Methods of Aircraft Charge Control During Flight

by

Benjamin C. Martell

Submitted to the Department of Aeronautics and Astronautics
in partial fulfillment of the requirements for the degree of

Masters of Science in Aeronautics and Astronautics

at the

MASSACHUSETTS INSTITUTE OF TECHNOLOGY

June 2021

Author .....
Department of Aeronautics and Astronautics
May 18, 2021

Certified by .....
Carmen Guerra-Garcia
Assistant Professor, Aeronautics and Astronautics
Thesis Supervisor

Accepted by .....
Zoltan Spakovszky
Professor, Aeronautics and Astronautics
Chair, Graduate Program Committee

Methods of Aircraft Charge Control During Flight

by

Benjamin C. Martell

Submitted to the Department of Aeronautics and Astronautics
on May 18, 2021, in partial fulfillment of the
requirements for the degree of
Masters of Science in Aeronautics and Astronautics

Abstract

The accumulation of aircraft electrical charge can impact lightning initiation, cause radio interference, or make it difficult for research aircraft to make accurate measurements of atmospheric electric fields. Two experimental campaigns are described in this thesis that relate to the control of net electrical charge on aircraft, and the associated physical phenomena. First, a successful flight demonstration of actively controlled charging in fair weather conditions is described. A corona discharge wire is used for remote charging of a 1.9 m wingspan plane to both positive and negative polarities. By applying a voltage between -13 and +13 kV to the wire, the plane charged to +23 and -30 kV, respectively. The system demonstrates comparable results to previous modeling and wind tunnel experiments, which showed an increase in plane potential and a decrease in corona current as wind speed increased. There are technological limitations to the charge control strategy, such as a saturation voltage due to spurious corona and the delicacy of the corona wire. The second experiment is the study of the behavior of streamer corona discharges in wind. A point-to-plane geometry is used to provide a baseline to compare to precipitation static (p-static) dischargers, which are in use on most airplanes today. We find that the discharge characteristics are strongly influenced by the wind: the frequency of pulsations and the average current increase with wind speed, but both become less consistent. In general, two types of streamer bursts emerged upon adding wind: first, the streamers tended to point with the wind especially at lower wind speeds and higher voltages; at higher wind speeds and lower voltages, the streamer bursts tend to point against the wind. To the authors knowledge, this phenomenon has not been experimentally observed before.

Thesis Supervisor: Carmen Guerra-Garcia
Title: Assistant Professor, Aeronautics and Astronautics

Acknowledgments

First and foremost, thank you to my advisor, Professor Carmen Guerra Garcia, for support in research and life. I am grateful for your encouragement, persistence, and positivity. Thank you to my girlfriend, Madeline Hoey, for putting up with me no matter what and for always making me smile, and for your inspirational drive to make the world a better place. Thank you to my mom, Lori Martell, for teaching me the meaning of commitment and empathy, and thank you to my dad, Robert Martell, for teaching me persistence and balance. Thank you to my entire family, especially Abby, Nan, and all my grandparents, for the endless and unconditional love and support.

This project could not have been completed without the help of Howard Samuels and the Burlington RC Flyers, who taught me to fly and enabled the success of the flight demonstration, Todd Billings and Dave Robertson who offer some of the most valuable and practical engineering guidance in the department, and my lab-mates Colin Pavan, Yiyun Zhang, and Lee Strobel, who have provided research guidance countless times. Further, thank you to our collaborators on this project, Pol Fontanes and Joan Montanya from the Technological University of Catalonia, who helped build the first iteration of the plane and telemetry system.

I am grateful for all the opportunities that I've had during my 2 years at MIT, and all of the people that are not mentioned here that helped make it great. The Big Idea Challenge team deserves a special shout-out for inspiring me to pursue space research in the future.

This work was funded by The Boeing Company through the Strategic Universities for Boeing Research and Technology Program. The international collaboration was supported by the MIT-Spain La Caixa Foundation Seed Fund (MISTI Global Seed Funds grant program).

Contents

List of Figures

List of Tables

Chapter 1

Introduction

1.1 Overview of Aircraft Charging

This thesis investigates technologies and physical phenomena related to the accumulation of electrical charge on airborne vehicles. Since airborne vehicles have no electrical ground reference, they present the unique electrical scenario of an isolated conductor, and so can easily maintain a net potential (voltage) relative to their surroundings. This net charge can affect the likelihood of lightning initiation, and can cause electrical discharges from the plane to the air surrounding it. Aircraft charging can occur naturally, but can also be controlled artificially if desired. In this thesis, charging refers to a change in net electrical charge on the aircraft, which can indicate an increase in positive or negative charge.

1.1.1 Naturally Induced Charging

Aircraft and other airborne vehicles naturally acquire electrical charge during flight, due mainly to frictional charging by precipitation particles such as ice, rain, snow, and dust. This triboelectric charging of the vehicle is typically (but not always) negative and is known as precipitation static or p-static [5]. Other sources of aircraft charging include corona discharge, charged particles in the engine exhaust, and contact electrification with the runway during takeoff [63].

Especially in thunderstorm environments, where there are strong electric fields and an abundance of water and ice particles, these natural charging mechanisms can lead to net charging levels of the order of 0.1-1 mC, which correspond to electric potentials of 0.1-1 MV relative to the surroundings when considering an aircraft self-capacitance of 1000 pF, such as the single-seat single-engine Schweizer powered sailplane used in the SPTVAR project [35, 31, 53].

1.1.2 Implications of Aircraft Charge and Strategies for Charge Control

The implications of aircraft charge control on radio interference and atmospheric electricity studies.

In the 1930-1940s, with the emergence of "all weather" aircraft, precipitation static became an active area of research as commercial airlines and government agencies recognized the hazards associated with the electrification of aircraft like its impact on radio communications [57, 65, 34]. When charge builds up on aircraft to the levels indicated in 1.1.1, it can cause corona discharge at the sharp points, corners, or edges of the airframe, such as the radio antennas and other extremities of the plane. Corona discharge on the radio antennas can cause electromagnetic interference noise, hampering communication with ground control or other aircraft. Early studies of this problem included flight campaigns with manned aircraft to elucidate the causes of precipitation static and quantify the influence of aircraft electrification on the severity of radio interference. Aircraft instrumentation included electric field meters, for measuring intensity and direction of electric fields, radio-noise meters, to measure the interference on antennas associated to precipitation static, air-conductivity meters, and current meters using induction probes and electrodes [65].

The most important technological outcome from these studies were passive dischargers, which are referred to as precipitation static (P-static) dischargers, or wicks, and are in use on most airplanes today. The primary purpose of p-static wicks is to dissipate the charge buildup using corona discharge at locations away from antennas

to minimize electromagnetic radio interference [5]. P-static wicks are passive elements of charge control which are activated whenever the aircraft acquires charge beyond some threshold which corresponds with electric field enhancements at the wick above its corona discharge inception.

Static dischargers today are typically of one of two varieties: a tip discharger, which is a variation of the static wicks patented by Dayton Granger in the 1940-60s [10] and includes several sharp wire tips in a rod bundle and a resistance gradient that leads the current towards the tip of the rod; and a parallel discharger, which includes a similar rod, but the tip consists only of two oppositely facing sharp points. Nowadays, the dischargers can include proprietary substrates and resistance coatings to maximize their ability to emit current at a low voltage threshold while reducing the level of radio frequency (RF) noise. They are typically located protruding off of the aft side of the wings and tail and there are requirements for the location and quantity depending on the regulatory agency, for example [3] and 14 CFR 25.899(a)(3). Testing of these dischargers usually consists of placing the wick 15 cm from a ground plate, and measuring the current and noise reduction, and is described in detail in United States General Specification MIL-DTL-9129E [4]. To the authors knowledge there have been no studies that investigate the effect of wind on the above metrics or the type of discharge, as this thesis begins to do.

The flight campaigns reported in Ref. [57, 65] using a B-17 research airplane also developed a controlled artificial charging system to simulate autogeneous charging of an airplane in any weather, motivated by a desire to simplify research in this field and avoid long and time-consuming flights to find appropriate weather conditions. This artificial charger was developed by the Naval Research Laboratory and was based on charge induction of water jets by an applied electric field prior to the separation of the jets into droplets. The water droplets would then carry away charge, as convected by the wind, and the aircraft would charge to the opposite polarity. In this case, the experiments focused on charging the aircraft to negative values and the water was charged positive. The charging system, consisting of about 200 jets, required an inducing potential of 10 kV and delivered a current of about 250 μA consuming about

75 gallons of water per hour [65]. These settings allowed to charge the B-17 aircraft to 500 kV, corresponding to a total net charge of 0.4 mC (when considering the 780 pF self-capacitance of the vehicle). These charging levels are comparable to those expected naturally and therefore the system was able to maintain the airplane potential near zero while flying in autogeneous charging conditions but was not considered a practical solution because of the considerable bulk and weight.

In the 1970-1980s, instrumented aircraft started to be used for atmospheric electricity studies. In particular, the New Mexico Institute of Mining and Technology in collaboration with the Office of Naval Research instrumented a modified Schweizer 845 single-seat aircraft, the Special Purpose Test Vehicle for Atmospheric Research or SPTVAR, to perform atmospheric electrical and cloud physics measurements in developing thunderclouds [31]. The aircraft was fitted with five electric field mills and was used to gather data from thunderclouds in the vicinity of the Langmuir Laboratory, Magdalena Mountains, NM, for science studies, as well as at the Kennedy Space Center, FL, for practical studies in connection to lightning risks to launch vehicles. It was soon realized that measurements of the atmospheric electric fields from onboard an aircraft are not straight forward as the aircraft becomes polarized, and there are important contributions to the measurement from the vehicle's net charge as well as charge plumes emitted by the aircraft, which need to be isolated from the external field contribution. To compensate for the aircraft's net charge, the SPTVAR tested an artificial charging system, in this case using a technique based on corona discharge first coined by Vonnegut [64, 63]. The artificial charger consisted of a brush-electrode connected to the high voltage terminal of a positive high voltage power supply whose low voltage terminal was connected to the structure of the aircraft. At high enough voltage bias, the brush-electrode would emit corona discharge and positive ions would be convected away by the wind, charging the aircraft to negative values. The brush-electrode was located at the aft end of the fuselage to favor ion evacuation. The applied voltage level was 5 kV, the ion currents were 5-10 μA and 20-40 μC of negative net charge was artificially acquired by the aircraft.

Artificial net charge control has also been considered as a means of controlling or

eliminating the tendency of a hovering helicopter to acquire net electric charge that can be hazardous to the ground personnel contacting the aircraft [43]. Studies in the 1990s revealed that an important source of helicopter charging was currents in the hot electrically-conductive exhaust gases induced by the local atmospheric electric fields. To compensate for this effect, Ref. [43] explored a charge control system that, rather than relying on artificial emission of charge as in [57, 65, 31], employed electrostatic shields around the engine exhaust and application of internal electric fields to modify the path of these exhaust currents. The system measured currents of about 12 μA and was able to achieve compensation of about 40 kV. For a heavy-lift helicopter like the ones contemplated in these studies the electrical capacitance would be of the order of 500 pF, resulting in stored energies around 400 mJ. For reference, discharges above 250 mJ can result in severe shock to humans, above 1 J, in possible unconsciousness and above 10 J in possible cardiac arrest [13].

From these studies it can be appreciated that charge control has been safely demonstrated for a variety of airborne vehicles including manned aircraft and helicopters, and using a variety of methods, ranging from emission of ions or charged drops to control of the ionized engine exhaust. However, most of these studies focused on charging to one polarity alone, and they provided a proof of concept without exploration of dependencies or limitations, in many cases exclusively reporting on/off operation in a particular configuration. In this thesis, we demonstrate electrical charging and discharging during flight of a small unmanned aircraft under fair weather conditions, using ion emission from a corona wire. The study considers charging to both negative and positive polarities, by employing high voltage positive and negative power supplies respectively, and addresses the influence of the amplitude of the applied high voltage as well as the wind speed.

The implications of artificial charge control on aircraft-triggered lightning

While the accumulation of charge can cause aircraft radio interference or others described above, it can also have an effect on the initiation of lightning. Lightning occurs naturally following a typical sequence of events: a cumulonimbus cloud forms with

temperatures of -15 to -25 °C near the top; natural convection causes an up-welling of super-cooled cloud droplets and very small ice crystals, which collide with falling graupel (soft hail); the collisions can cause the ice crystals to become positively charged and the graupel negatively charged; this polarizes the clouds to become negatively charged at the bottom and positively charged at the top; the polarization creates strong electric fields that can cause lightning if they surpass the electric breakdown of air [6, 2]. Lightning occurs most often from cloud-to-cloud (intra-cloud lightning) but can also travel down to the positively charged Earth. A lightning strike begins as a partial discharge such as a corona, and slowly develops into a leader. When two leaders of opposite polarity connect, a violent surge of current is passed through the plasma channel, which emits an intense light and sound.

In the 1940s, after the catastrophic crash of a Pennsylvania-Central Airlines DC-3A aircraft, formal studies investigating the effects of lightning on aircraft and its mitigation began [50]. Since then, there has been a lot of research into the mechanism of lightning attachment to airplanes, as well as the development of several technologies to mitigate the likelihood and damage of an attachment.

90% of aircraft lightning strikes are initiated by the aircraft itself, through a process known as aircraft-triggered lightning [35, 44, 37]. In this process, the discharge begins when a fully conductive aircraft flies into a region of high electric field or encounters a rapid change in the ambient field, such as a nearby intra-cloud strike [54]. The ambient electric field polarizes the airplane, amplifying the field at its extremities and initiating a bidirectional leader [42, 33]. Since positive leaders have a lower threshold field for initiation, they are typically initiated first. Once the positive leader has biased the airplane potential to sufficient negative levels, the negative leader forms on the opposite end of the aircraft, a few milliseconds later.

Mitigation strategies include reducing direct effects and damage to the attachment point of the aircraft. Such strategies are ensuring a fully conductive path for the high current to travel through by implementing an expanded metal foil, wire mesh, and diverter strips on the radome, and ensuring continuity of metal fasteners that are used on composite structures like the fuel tanks. Indirect effects such as electromagnetic

interference (EMI) are also mitigated using wire bundle shielding, and grounding straps [58].

Although these mitigation and protection strategies have reduced the likelihood of airplane failure (the last major accident caused by lightning was the Pan Am Flight 214 in 1963), a commercial aircraft is still struck by lightning once or twice every year on average [21], which can necessitate costly delays and repairs. In 1998, the National Oceanic and Atmospheric Administration estimated that lightning is responsible for around $ 2 billion annually in commercial airline operating costs and passenger delays. The present day costs are likely much higher if accounting from repair costs and inflation.

It has been recently proposed that active charge control of aircraft could reduce the probability of aircraft-triggered lightning by locally modifying the electrostatics of the vehicle [41, 26]. Based on this phenomenological description of lightning initiation from aircraft, Ref. [41, 26] proposed that flying uncharged was not optimal in terms of lightning risk reduction, and that aircraft-triggered lightning could be made less frequent by flying at an optimal net charge level that makes the inception of the positive and the negative leaders equally unlikely. In the majority of scenarios, this situation corresponds to some amount of negative charge. The theoretical study in [26] estimated that this optimum charge would be on the order of 0.1-1 mC, negative, for a Falcon-sized aircraft (22.5 m wingspan), and that the net charge scales quadratic with size (or linearly for the electric potential). For an aircraft with a 1-2 m wingspan, like the ones used in this thesis, the optimum net charge would be around 10 μC corresponding to an electric potential around 100 kV with respect to the environment.

Experimental validation of this hypothesis was provided in Ref. [48] through long arc leader attachment tests on a model aircraft and exploration of the effect of vehicle net charge on the inception of the positive leader. The experiment was conducted in the Labelec Lightning Laboratory [1] using a model aircraft with a 1 m wingspan and variable net charge between 0-1.6 μC negative (or electric potential 0-40 kV negative with respect to the environment). In this range, which was still far from the theoretical optimum at 7 μC negative (-170 kV), the ambient breakdown field could

increase by as much as 30%, demonstrating the effectiveness of the approach.

In this thesis, we explore a corona discharge-based active charge control system that is able to electrically charge an aircraft during flight to comparable potentials to those studied in the Lightning Laboratory.

1.2 The Other Corona: Corona and Other Partial Discharges in Air

Partial discharges such as corona discharge (unrelated to the COVID-19 coronavirus) result from a high electric field gradient and subsequent breakdown of a dielectric material, but not such a high field that the breakdown fully bridges the electrodes, which would cause a full discharge such as lightning or arcing. These discharges, which usually emit light in the visual and UV spectrum, can have many forms depending on the geometry, waveform, and polarity of the high voltage electrodes. These types of discharges occur naturally and are often studied as a pre-curser to lightning initiation [38], or as gigantic jet discharges in the atmosphere [61]. In high voltage engineering applications, such as power transmission, ignition, and radio transmitters, these discharges are often unwanted and unintended, and have been mitigated since the 1929 publication of Peek's book titled Dielectric Phenomena for High Voltage Engineering [49]. This work was followed by many, including those of Raether [52], Loeb, and Meek [40], who began to observe and characterize streamer corona discharges for the first time (streamers are investigated in detail in Chapter 3 of this thesis). These works and others provided the basis for how these phenomena are studied and many of the theories hold true to this day. New technologies began to emerge in the subsequent years that use corona discharge for their advantage. Electrostatic precipitators [19], ozone production [12], water treatment [55], and combustion [56] are just a few of the technologies that use partial discharges in air. Controlled partial discharges in air can be very cost effective because of their low energy and non-thermal properties. The following sections will describe the mechanisms and regimes of direct current

(DC) partial discharges in air. Despite a DC power source, some of the discharges studied here are pulsatory in nature.

1.2.1 Positive DC Point Corona Discharge

In this thesis we are primarily interested in investigating Positive DC Corona discharges. The positive distinction must be made because there are elementary differences between positive and negative corona. The differences are due primarily to direction that the electrons move relative to the propagation direction of the ionization front. Electrons are able to accelerate to high velocities much faster than ions due to the disparity in masses. These fast-moving electrons collide with neutral atoms or molecules with such energy that they ionize it. For example, the impact ionization of an oxygen molecule is described as:

$$e^- + O_2 \longrightarrow 2\,e^- + O_2^+$$

The electron will either recombine, giving off energy in the form of UV or visible light, or the two electrons are once again accelerated until they each collide with another molecule, again ionizing and releasing 2 more electrons. This growth process is called an electron avalanche and it occurs in opposite directions depending on the polarity. For example, when the high voltage electrode is positive, the electrons are attracted towards it [9, 11]. The subtle difference in electron direction creates much different behavior even at the macro scale.

The general theory described above is well known, however, work is still ongoing to fully understand and quantify the behavior in different scenarios. Broadly, there are two types of corona, streamers and glow, however each category has its own subcategories. The following describes the 4 main discharge regimes, in order of increasing point-to-plane electrode voltage, as reported by Trinh [59, 14]:

The first discharge to appear is the burst corona, which is a thin, luminous layer around the anode surface. It results from the ionization activity spreading around due to small positive space charge regions that suppress the discharge in that region.

As the voltage is increased, onset streamers emerge, which propagate with the electric field lines towards the opposite electrode, forming forming a filimentary, branching

streamer “tree.” The propagation occurs as an electron avalanche towards the anode and creates a region of positive space charge, which then acts as a new "anode" and creates a secondary electron avalanche. The streamer propagation is driven by the self-induced electric field generated by the positive layer of charge at the streamer head. The streamer continues propagating outwards until a residual positive charge is generated as a result of cumulative avalanches and electron consumption by the anode. This space charge covers most of the anode surface, and reaches a concentration such that the local electric field gradient declines to below the critical value for ionization. This temporarily suppresses the streamer discharge, while the space charge fades under the applied field, until the conditions required for a new streamer are once again met. This time scale is governed by the ion drift velocity, which is characterized by the following equation:

$$v = \mu E, \tag{1.1}$$

where μ is the ion mobility and E is the electric field. This process continues repeatedly, and depending on the operating conditions in atmospheric pressure air, can repeat consistently at a frequency of $\sim 10^3$ Hz, with individual streamer bursts propagation occurring in 10s to 100s of nanoseconds [8].

Positive glow corona has long been observed as an apparent continuous glow since the first observation by Michael Faraday in 1838 [20], however work by others more recently [18, 45, 59] has characterized it as a fast ($\sim 10^5$ Hz) pulsating discharge. The glow region appears as a thin luminous layer and corresponds with the high space charge appearing as a result of the slow moving ions. The pulsation is likely due to the space charge moving around the anode surface, and the DC component results from the space charge being removed rapidly enough to promote surface ionization activity, but the field is not high enough to allow streamer propagation.

Finally, the breakdown streamer emerges if the applied voltage is further increased, which eventually leads to a breakdown of the gap. This discharge is similar to onset streamers, but with a higher current, and occurs when a region of intense ionization

and positive space charge near the anode is cleared away from the anode due to the applied electric field.

It is rare to observe all of these types of discharges for a given geometry, for example for a high diameter (of the electrode) to gap distance (to the ground plate) ratio, typically only one regime, glow discharge, is observed before full breakdown. In other cases with a very low diameter to gap ratio, only onset streamers are observed. This high variability in discharge has yet to be fully understood, and is being actively studied by researchers who seek to understand what causes certain regimes and what causes their transitions [66, 38, 39].

To conclude this brief introduction, we now review prior work on the effect of wind on streamer corona discharge. Previous studies have experimentally shown that corona current increases linearly with wind speed, for applications such as thunderstorms and lightning mitigation for wind turbines [7, 15, 36, 51]. Most of these studies, however, concentrate on the glow regime. Until recently, no studies had quantified the impact of wind on streamer discharge regimes in a point-to-plane geometry. Vogel and Holboll made such measurements, and observed an increase in frequency and current with wind, and showed long exposure UV images of the streamer corona bending with the direction of the wind. These results were later confirmed by a 3-dimensional model by Niknezhad et al [46], but they mostly reported trends and did not adequately quantify the streamer frequency or current change with wind, and the images were taken at long time scales where it is difficult to discern the branching behavior [62]. As explained in Ref. [46], the reason the streamer bends with the direction of the wind is that the plasma channel that is left over from a previous streamer will succumb to the airflow, but some electrons will still be attracted towards the anode. The subsequent streamer will have a curved shape with the wind and then up to the ground plate. This regime is confirmed in Chapter 3 of this thesis, and a novel regime is also discovered, where the streamer propagates against the direction of the wind. We begin to characterize the emergence of these regimes for positive DC corona discharge in a point-to-plane geometry with tip diameter of 0.174 mm and gap distance of 25mm. We investigate the effect of applied voltage and wind speed on regime tran-

sitions and temporal characteristics such as the frequency of pulsation, the electrical current, and the shape of the streamer bursts. Our hypothesis is that the presence of wind will increase the frequency and electrical current of these pulsations due to the enhanced transport of ions (which is governed by the electric drift described in Equation 1.1.) The work provides a baseline for future studies that may vary this geometry configuration, and test other relevant engineering systems such as a p-static discharger, or a wind turbine blade.

1.3 This Work

1.3.1 Motivation

Broadly, this thesis is motivated by urge to explore that which is unknown. It is the courage of people who try something new, push the boundaries of the ordinary, and *share* their work, that has improved our society in so many ways. My goal in this thesis and in my life is to drive forward the sustainable human exploration of the universe.

More specifically, this work is motivated by exploring electrostatic problems on airplanes, especially those related to aircraft charge control such as lightning mitigation and radio interference, but a system of charge control can also benefit research aircraft performing electrical measurements in the atmosphere and address safety concerns in helicopters and other rotorcraft. In the first chapter, this work makes a step towards the maturation of the lightning mitigation technology into a scaled system, bringing it from a Technology Readiness Level (TRL) of 5 to 6, which is a subsystem prototype demonstration in a relevant environment [60]. While active charge control of aircraft has been shown before, this work expands on the quantification of relevant charging and discharging behaviors, the effect of wind, and explores the limitations of this type of system. The knowledge gained from this thesis will inform future work on lightning mitigation systems using active charge control and studies of the electrical properties of the atmosphere. In the second chapter, beyond direct applications to

the airplane industry, this research investigates the fundamental physics of streamer discharges in wind. Fundamental research such as this always presents an important step in advancing human knowledge and understanding the universe. Streamer discharges are a complex phenomena that is yet to be fully understood and utilized. The effect of wind on these discharges is especially opaque, with this thesis being one of the first to explore this in detail.

1.3.2 Outline

This work is divided into two sections, which constitute two experimental campaigns. The first section, Chapter 2, details the successful effort to demonstrate the ability to control the charge of an aircraft in flight using ion emission from a corona discharge. The charge levels achieved are comparable to those tested in the Lightning Laboratory and had a measurable impact on lightning initiation [25]. After detailing the flight and experimental platform and the campaign summary, the charging and discharging results are provided and commented on. The use of corona discharge in wind for controlled charging of an electrically isolated body has already been demonstrated in a wind tunnel setting [24], and the results from the flight campaigns in this thesis will be compared to those more fundamental studies.

The second section, detailed in Chapter 3, details the study of the discharge characteristics of streamers in wind. Although this study is an idealized point-to-plane geometry, it is used as a first and tractable step towards studying the behavior of p-static discharger behavior in wind. The results of the teting are reported and commented on. Finally, Chapter 4 offers a conclusion to the thesis and future work on these projects in both the short term and long term.

Chapter 2

Flight Demonstration of Controlled Artificial Aircraft Charging

This chapter includes a detailed summary of the work done developing an experimental flight platform to study remote aircraft charge control, the results of the campaign, and concludes with a thorough discussion of the results in the broader context, as well as suggestions for future work.

The purpose of this experimental flight campaign was to test the charge control concept and technology in true flight conditions. The artificial aircraft charging technology using a corona wire had previously been demonstrated in the MIT Wright Brothers Wind Tunnel, and had been shown to be able to reduce the risk of lightning initiation [24]. The next step towards making this technology viable for use on commercially built airplanes is to test a prototype in a real flight scenario, bringing the technology from TRL 5 to 6.

2.1 Experimental Requirements

The requirements are detailed in Table 2.1.

Table 2.1: Requirements

Req ID	Requirement	Explanation
2.1.1	The plane must be able to fly steady and level for at least 5 minutes of flight time.	Minimum amount of time for a useful amount of data.
2.1.2	The plane must be fully conductive throughout the body, with a resistance of less than 100 Ω between any two points.	This is essential to demonstrate charging of the aircraft and ensure that the electronics are surrounded by a Faraday cage.
2.1.3	The conductive skin must be connected to the ground of the power supply.	This will create a potential difference between the wire and the plane.
2.1.4	The plane must have a range of at least 0.5 km.	This will allow large circles to be flown in line-of-sight conditions.
2.1.5	The plane must be able to carry a high voltage power supply that can provide a 15 kV potential to the corona wire.	In order to get meaningful results that can be validated by the wind tunnel experiments.
2.1.6	The corona wire must create a uniform discharge, without inducing spurious corona from the wire ends.	Spurious corona can cause unsteady discharge which will be harder to validate with a model.
2.1.7	The plane must be able to take off and land from the ground.	To avoid risk of hand-launching, and for safety.
2.1.8	Data must be transmitted directly to a ground station, with back-up on-board memory.	Science data is critical.
2.1.9	The platform should make measurements of the airspeed, wire voltage, plane voltage, supplied power.	Necessary diagnostics to adequately test charging system.

2.2 Flight Platform

2.2.1 Airframe

The first decision that was made in this technology demonstration was the vehicle itself. The plane will drive many of the sub-level requirements, such as mass, propulsion, controls, and surface treatment. Prior to the work performed in this thesis, a demonstration was attempted, but failed due to issues with the flight mechanics of the plane. To reduce the likelihood of future flight problems, a relatively simple glider airplane with a 1.9 m wingspan was chosen for this study, with a single "pusher" propeller and a conventional fuselage-mounted tail unit. This plane is designed to hold up to ∼4 kg all up weight (AUW). The vehicle ultimately chosen was the Finwing Sabre, which has a similar shape to modern commercial airplanes. This plane was chosen because it met all of the relevant requirements (2.1.1, 2.1.5, 2.1.7).

2.2.2 Undercarriage

The undercarriage proved to be one of the most challenging mechanical components of the plane, due the extreme stresses and vibrations that the plane undergoes during take-off and landing. During testing, the plane regularly took the full runway (∼100 m in length, mowed grass) to take off, but it was the landings which were more difficult and often resulted in damage to the undercarriage. The undercarriage thus underwent a series of updates, which are still on-going.

The undercarriage has two main parts. The nose gear, which is in the front and has its direction controlled by a servo, helps steer the plane during taxi and take-off. The first nose gear was supplied by the manufacturer of the plane and was made of thin aluminum that plastically deformed after a few taxi tests. After further research it seemed that others operators of this configuration had this problem as well. The nose-gear was then upgraded to a stiffer steel spring shown in Figure 2-1. This nose-gear has since been bent slightly backwards due to bumps in the grass field, but it still works well. The other main part of the undercarriage is the landing gear, which

Figure 2-1: Final nose gear configuration.

consists of two 8.9 cm diameter wheels supported on each side of the plane. This part was also upgraded from the original, using a stiffer plastic instead of thin aluminum. Unfortunately this was often ripped from its glued position on the underside of the plane. All the force from the landing impact goes into the 45 cm^2 glue joint, and each impact weakens it or begins to break the surrounding foam. Several methods were used to remedy this, including using an additional plate, with Nylon bolts that should break before the epoxy. This still ended with the undercarriage breaking off during landing. Despite the challenges, this system did satisfy Requirement 2.1.7. A new connection system that uses a support structure embedded in the foam of the fuselage may help to distribute the load, and is currently being investigated.

2.2.3 Motor/Control Surfaces

As a general rule of thumb for remote control airplanes, the motor should produce 100 Watts for every 0.5 kg that the plane weighs. Since the plane was expected to be $\sim$4 kg, the motor must produce 800 Watts. Using a Watt-meter that was placed in series with the flight battery, this was tested in the lab, with the plane secured to the ground. It was found that the original motor was producing only 350 W, which was determined to be insufficient, and so the motor was upgraded to the BadAss 3515-940Kv Motor (728 Watts for 11x5.5 prop). The manufacturer (Innov8tive Designs) of these motors tests them with all combinations of propellers, and have provided all of the data on their website. When testing this motor, we achieved a power output of 728 W, which was deemed sufficient, as the final mass was 3.576 kg, and the expected flight maneuvers are very gentle.

The control surfaces are actuated using servos. Each servo takes a 5 V supply and uses PWM (Pulse-Width-Modulation) to determine the angle of rotation. Each one is trimmed so that the middle of the actuation corresponds with the middle of the control range.

2.2.4 Radio Transmitter and Receiver

The transmitter used is a Spektrum DX6e six channel transmitter, which is paired to a Spektrum AR620 receiver. These control each of the 5 servos (the flaps are not used) and the throttle. These systems are designed for $>$1 km of flight range, satisfying Requirement 2.1.4. Flight training was provided by Howard Samuels at Burlington's RC Flyers Club, using a Spektrum buddy box system.

2.3 Charging elements

2.3.1 Conductive Skin

Requirement 2.1.2 states that the plane must be conductive throughout. For the purposes of charging, only two parts of the plane must be conductive: the wing,

so that the ions being emitted will be attracted back to the plane; and the surface surrounding the electric field mill, so that it has a consistent reference. For safety purposes, however, it is important for the entire plane to be conductive to act as a Faraday cage for the electronics, which will be electrically grounded to the surface of the plane. If the electronics were not grounded in such a way, they would have a potential difference relative to the plane, inducing an electric field which could cause corona discharge to form on the circuit boards leading to an electronic short and causing permanent damage.

The conductive skin was the most challenging part of the experimental platform. Prior to the start of this thesis, preliminary tests in August 2019, which used conductive spray paint, showed issues with inconsistent paint thickness and wearing over time. For these reasons, it was originally decided to use Aluminized Mylar as the conductive skin for this plane, with copper tape connecting the various surfaces and acting as the Faraday cage for the electronics, as shown in Figure 2-2. This was used for several months but its reliability decreased over time and it may have contributed to a crash landing on October 15, 2020. The main difficulty with the Aluminized Mylar is that it does not form well to curved 3-dimensional shapes, like the fuselage or wings of the plane. Its rigidity helps it stay an even thickness throughout the surface, however it prevents it from forming around curved surfaces. Another challenge with this material is connecting to it electrically. Several connection methods were tested including clips, aluminum tape, and spot welding, and it was determined that copper tape offered the best electrical connection. Despite this, over time the connection between the copper tape and Mylar loosened, and needed to be re-applied before each flight. After the crash on October 15 2020, the entire flight system was re-examined, including the Mylar, to figure out why this happened. The electrical connection had loosened during flight, causing an electrical polarization of the different parts of the plane. This led to interference through the ground line of the electronics, and caused the servos controlling the plane to jitter and rendered the plane uncontrollable. This loosening may have been a result of the high currents melting the thin layer of aluminum as it transferred from the copper tape. An image of the suspected melted

Figure 2-2: Plane with aluminized Mylar and copper tape configuration.

aluminized Mylar is shown in Figure 2-3.

After discovering this, it was decided to go back to using conductive spray paint, which ultimately was much more consistent at keeping the various parts of the plane connected than the Mylar. No connection point issues were ever found using this solution. Figure 2-4 shows the plane coated in conductive paint. The paint used is MG Chemicals 843AR and fulfills Requirement 2.1.2.

2.3.2 Electric Field Mill

An electric field mill (EFM 113B) was used to infer the relative potential of the plane to the surrounding air. The electric field mill was placed on the nose of the aircraft, flush with and grounded to the conductive surface of the plane.

The electric field mill is calibrated by applying a known voltage (up to 40 kV) to the electrically isolated plane in flight conditions the laboratory. The plane is mounted

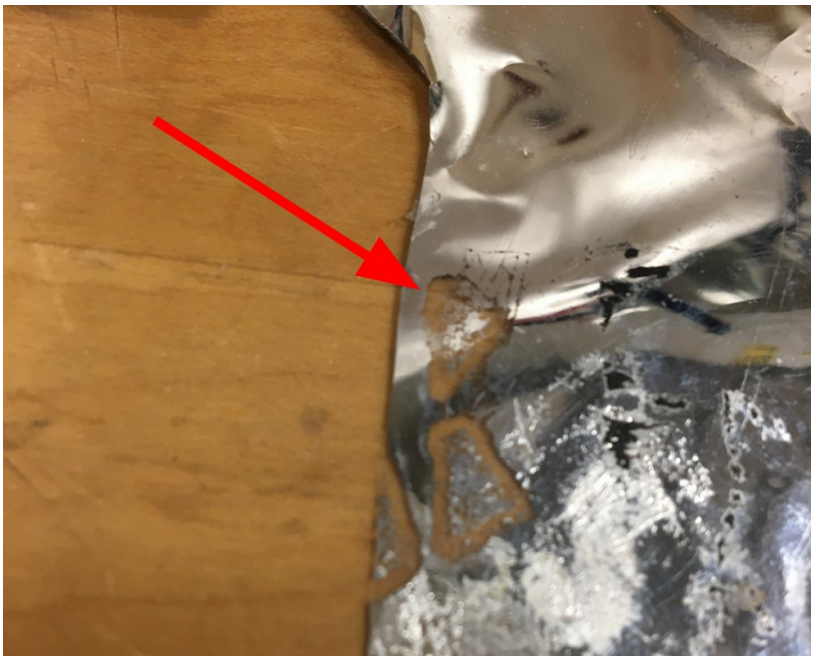

Figure 2-3: Aluminized Mylar melted at the connection to the copper tape.

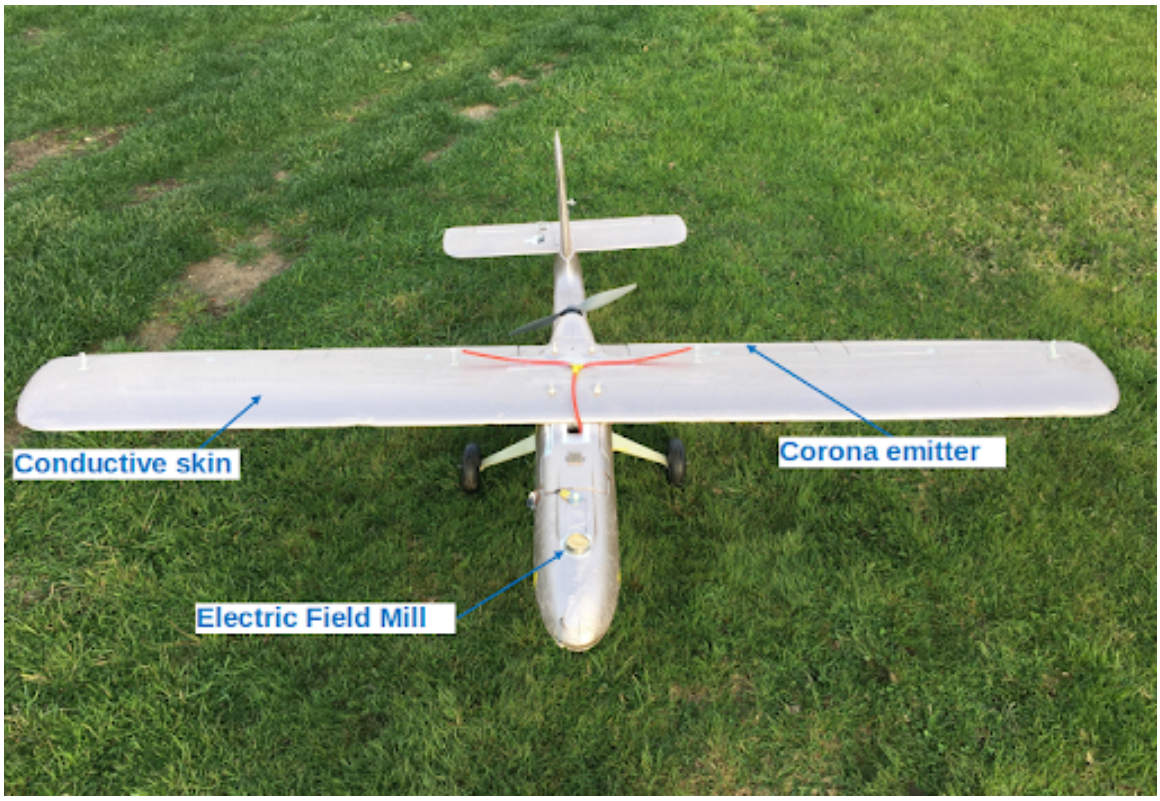

Figure 2-4: The final configuration of the plane, with conductive paint coating the outer surface, an electric field mill to infer the plane potential, and a corona wire to charge the plane.

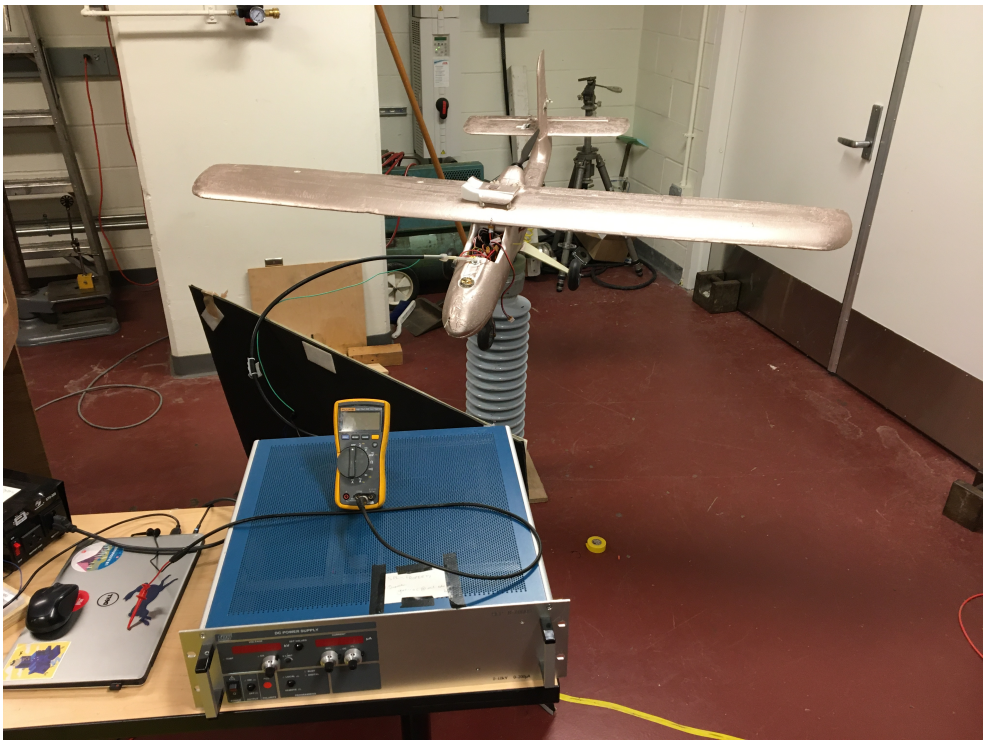

Figure 2-5: Photo of the calibration setup in the laboratory. The plane is mounted on an insulating cylinder, and brought to a known voltage (EFM calibration) or the corona wire is turned on and the voltage and current are monitored (power supply calibration).

on a corrugated insulator and connected to a high voltage DC power supply, as shown in Figure 2-5. The plane potential presents a linear relationship with the local electric field measured by the electric field mill, which is located close to the nose of the plane and flush with the surface. Each range (5, 20, 50, and 200 kV/m) of the electric field mill is calibrated separately.

Both positive and negative polarities were calibrated, as shown in Figures 2-6 and 2-7. As will be seen later in the thesis, the calibration is very sensitive to the position of the electric field mill, and vibrations during take-off and landing may induce slight variations in the location of the field mill (along its axis). An additional calibration was performed after a particularly bumpy takeoff that resulted in the EFM falling down about 2 cm into the plane. This configuration was recreated and the calibration is shown in Figure 2-8.

Note that the results are presented in terms of electrostatic potential with respect

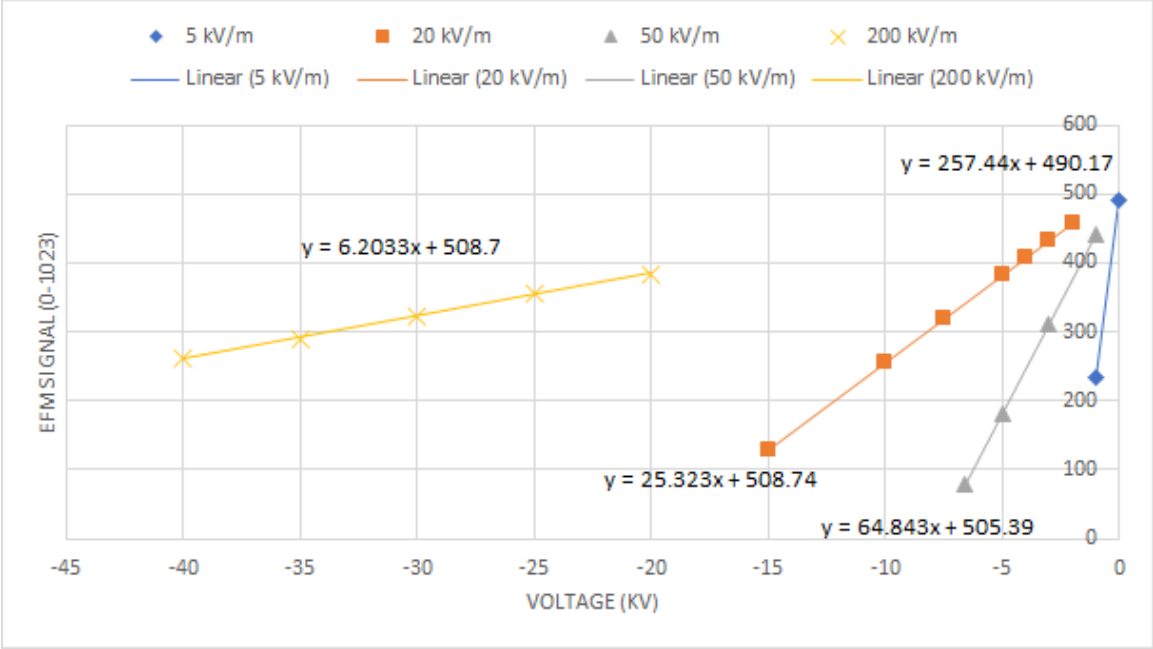

Figure 2-6: Electric field mill calibration for negative charging.

to the environment rather than charge acquired by the plane since this is a more direct measurement. The electric potential can be related to the net charge through the self-capacitance of the vehicle which in this case is of the order of 75 pF, e.g. a potential of 30 kV corresponds to approximately 2 μC.

2.3.3 Airspeed Sensor

The airspeed is detected using an MPXV7002DP differential pressure sensor (-2:2 kPa) attached to a pitot tube and is mounted protruding 4 cm from the nose of the airplane.

The airspeed sensor, mounted on the vehicle, is calibrated in a 46x46 cm^2 wind tunnel with known air speeds up to 15 m/s, demonstrating a linear relationship between measurement and wind speed, shown in Figure 2-9. Speeds below 5 m/s can not be measured by this sensor.

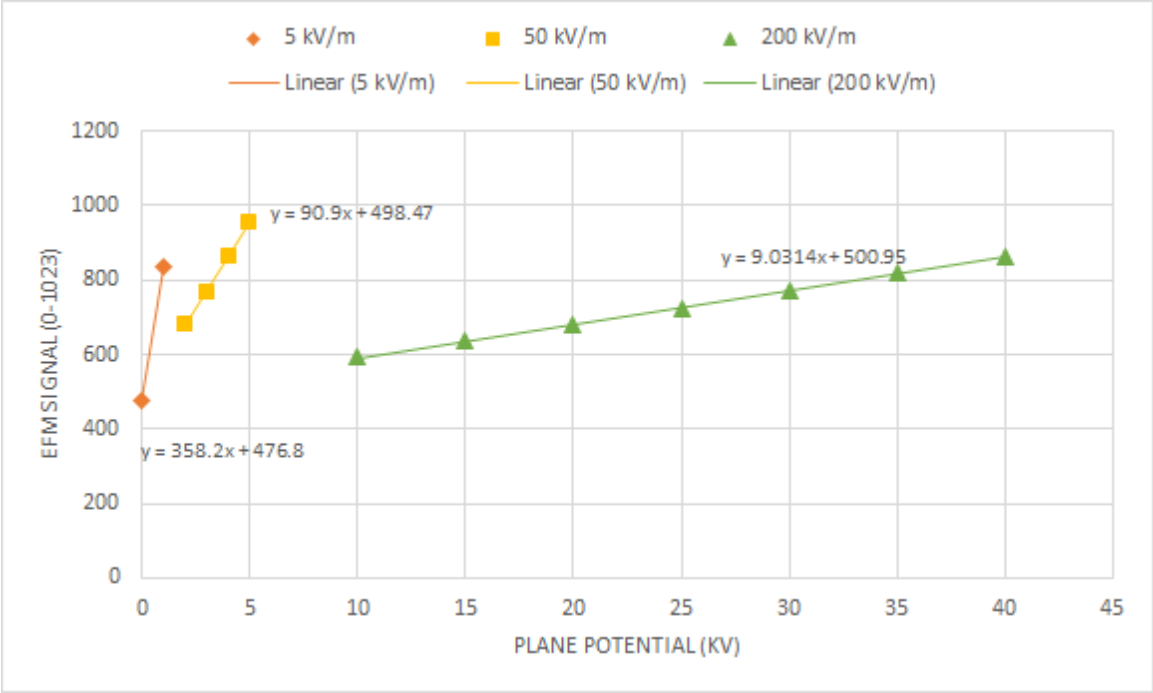

Figure 2-7: Electric field mill calibration for positive charging.

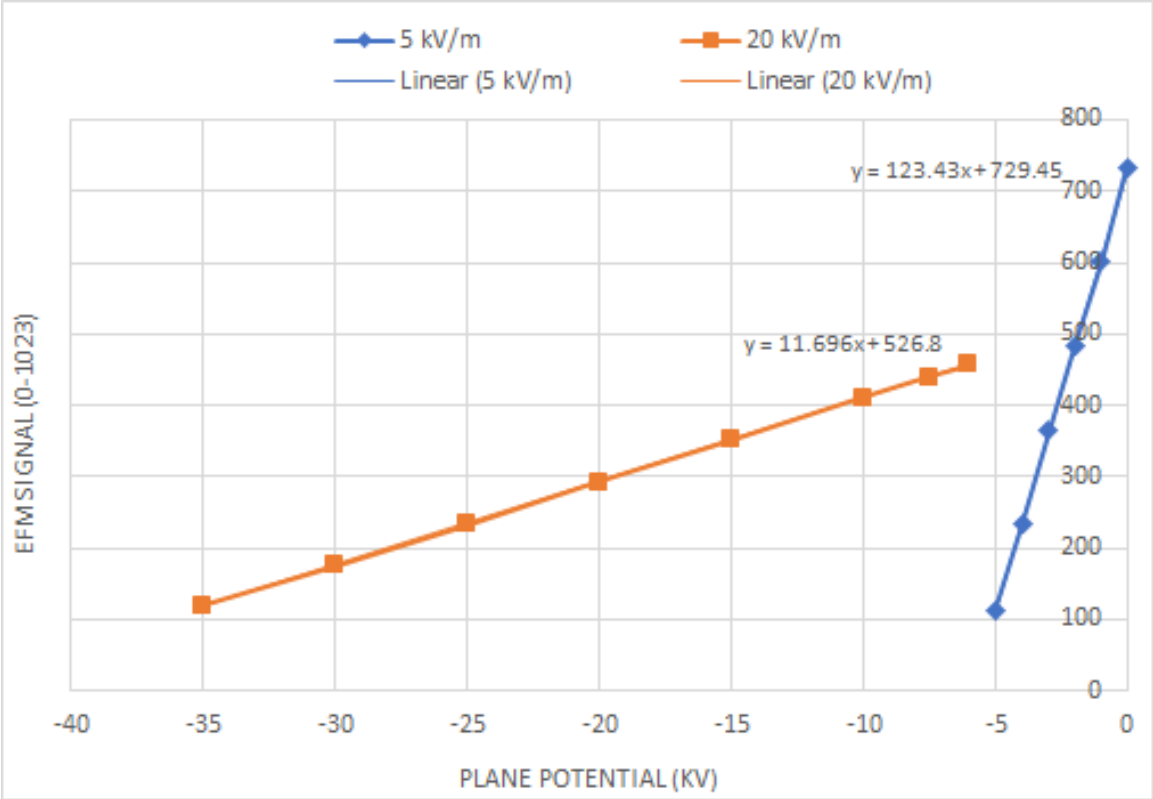

Figure 2-8: Electric field mill calibration for positive charging, positioned seated lower in the body of the airplane, to replicate conditions from Nov 25 flight 1, where the field mill was shifted during takeoff.

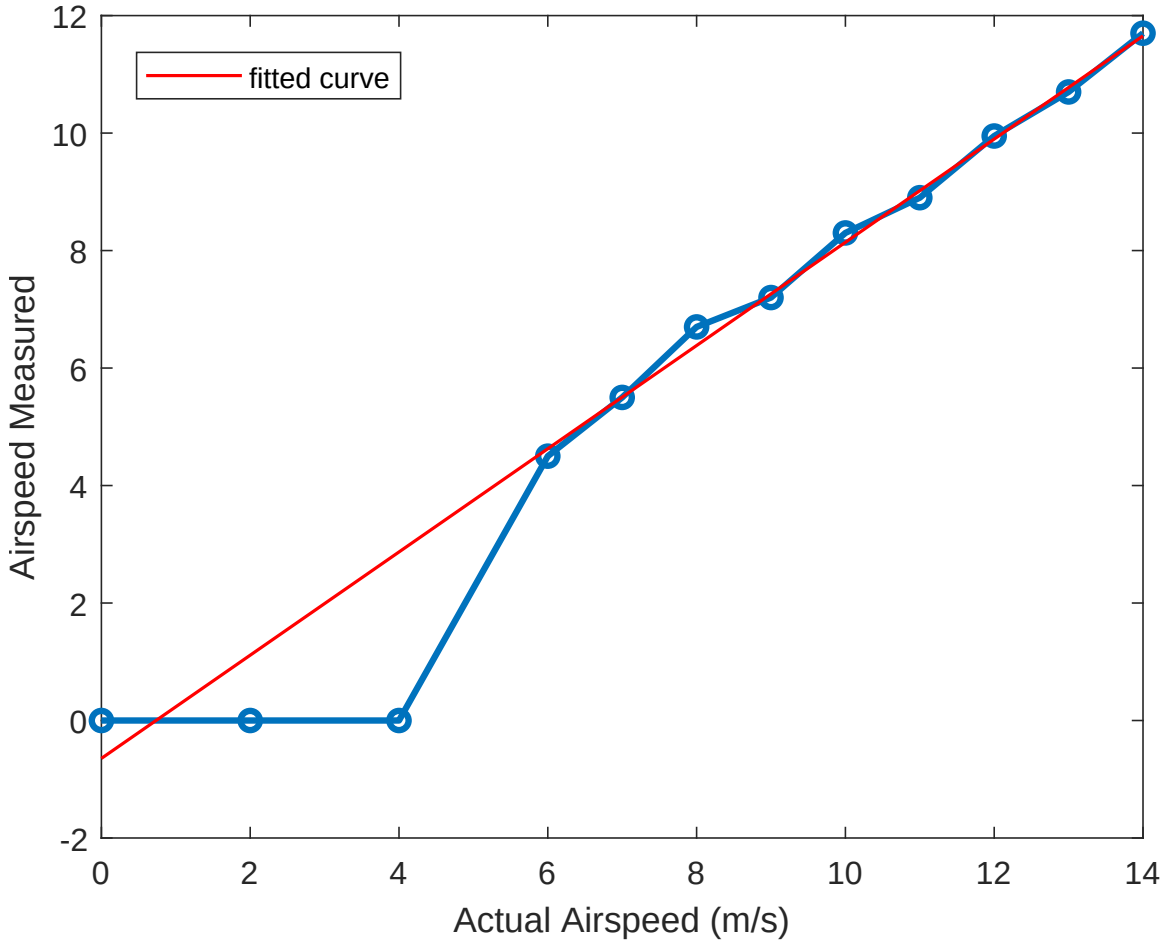

Figure 2-9: Airspeed calibration. Airspeed measured through the pitot tube sensor versus actual airspeed from the calibrated wind tunnel.

2.3.4 Telemetry

The telemetry system, which was developed by the collaborators on this project, Pol Fontanes and Joan Montanya, at the University Polytechnic of Catalonia, uses an XBee radio and an Arduino Nano to collect the sensor data and control the high voltage power supply. Using the analog input channels, the data from the electric field mill, airspeed sensor, and the power supply are collected and transmitted continuously (at a rate of approximately 3 Hz) to the ground station, while simultaneously writing the data to an on-board SD card for redundancy. The control board also receives commands from the ground station, and converts the commands into a 0-5V DC signal that controls the high voltage power supply, and the safety relays in between. The positive and negative power supplies require different operating code, so the Arduino program must be uploaded before switching. The board also features a power converter and regulator, that ensures that the power supply receives a constant 12V signal instead of the variable voltage from the LiPo battery, and so that the Arduino is powered by a consistent 5V.

2.3.5 Charging System

In this study, two 620 mm long, 0.25mm diameter tungsten corona wires are electrically isolated 2 cm above the aft surface of each wing, as shown in Figure 2-10. The location of the wire was similar to the optimal location found in [24]. Special care was taken to mitigate spurious corona by adding 6.35 mm diameter aluminum spheres to the ends of the wires.

The corona wires are connected to the high voltage terminal of the positive high voltage power supply, which is capable of delivering up to +15 kV and 0.26 mA (Ultravolt 15A 12-P4) for the negative charging experiments; and a negative high voltage power supply capable of delivering up to -15 kV and 0.26 mA (Ultravolt 15A 12-N4), for the positive charging experiments. This power supply provides real time data on the current being applied to the wire. The ground of the power supply is connected to the conductive surface of the plane. This ground is also connected to

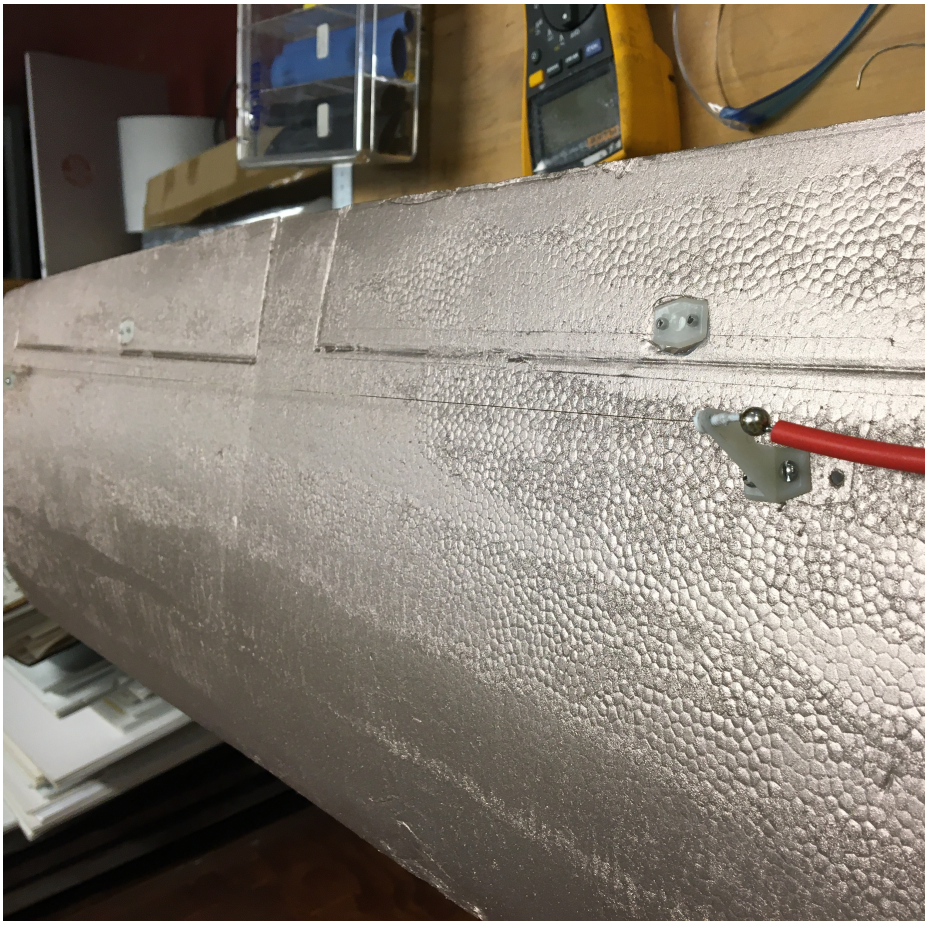

Figure 2-10: Corona wire mounted above the trailing edge of each wing.

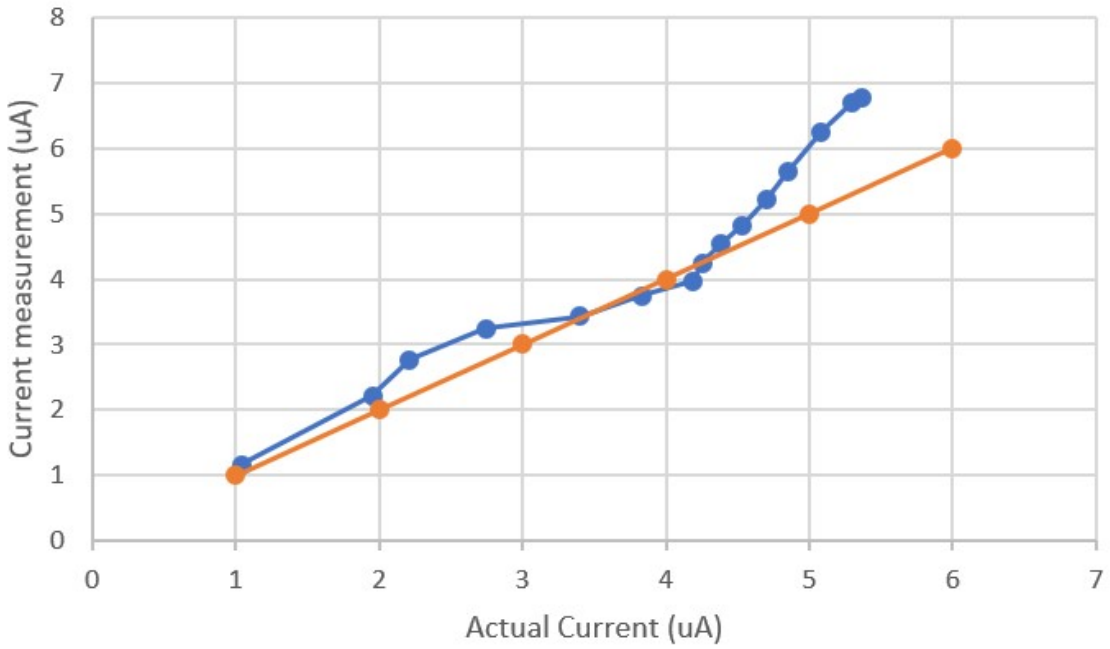

Figure 2-11: Calibration of the power supply current sensor (blue), compared to a 1:1 line (red).

the ground of the flight electronics, to avoid damage caused by a high electric field inside the plane.

The power supply current is calibrated using a high voltage 1 GΩ resistor in series with a 470 Ω resistor, and a Fluke 115 multimeter, and the applied voltage command is calibrated using a 1000:1 high voltage probe. The current calibration is shown in Figure 2-11. The current appears to deviate from the 1:1 behavior at the higher currents, but it is suspected that this is due to spurious corona in the connector used, which is rated to voltages up to 13 kV (this test went up to 15 kV).

The charge control system and sensors are powered by an on-board 3S 1300 mAh 45C LiPo Battery.

2.3.6 Flight System

The final flight configuration components are detailed in Table 2.2, and more details about some of them are described earlier in this chapter. A diagram of the full system is shown in Figure 2-12.

Table 2.2: Details of the equipment used for this study. The mass was measured or estimated based on the total flight mass of 3.576 kg.

Category	**Sub-Category**	**Item**	**Specs/Part**	**Mass (kg)**
Flight	Plane	Fuselage, Wings	Finwing Sabre, EPO foam, 1900 mm wingspan	1.52
Flight	Plane	Undercarriage	.35-.61 Dubro fiberglass reinforced landing gear, dual strut steel spring nose gear	
Flight	Propulsion	Propellor	12x8 APC pusher propellor	0.048
Flight	Propulsion	Motor	BadAss 3515-940Kv	0.185
Flight	Control	Flaps Servos (2)	Hitec HS-85BB High Torque Micro Servo	0.038
Flight	Control	Aileron servos (2)	Hitec HS-85MG Premium Metal Gear Micro Servo	0.042
Flight	Control	Ruder servo	Hitec HS-85MG Premium Metal Gear Micro Servo	0.021
Flight	Control	Elevator servo	Hitec HS-85MG Premium Metal Gear Micro Servo	0.021
Flight	Comm.	Transmitter	Spektrum DX6e 6 channel transmitter	0
Flight	Comm.	Receiver	Spektrum AR620 6 channel receiver	0.008
Flight	Power	Flight Battery	Admiral Pro 4S 5000 mAh 60C LiPo	0.494
Flight	Power, Control	ESC/BEC	80 Amp	0.095
Experiment	Telemetry	Control board	Xbee Radio, Arduino Nano	0.2
Experiment	Power, Sensor	High Voltage Supply	Ultravolt 15A 12-P4; Ultravolt 15A 12-N4	0.198
Experiment	Power	Experiment battery	Tattu 3S 1300 mAh 45C LiPo	0.119
Experiment	Sensor	Airspeed sensor	MPXV7002DP Differential Pressure pitot tube	0.016
Experiment	Sensor	Electric Field Mill	EFM 113B	0.164
Experiment	Experiment	Corona Wire	Tungsten 0.25 mm diameter	0.001
Experiment	Safety	Timer	12 V timer relay	0.024
Experiment	Ground	Conductive skin	MG Chemicals 843AR	0.1
General	Misc		Wiring, connectors, nuts, bolts, linkages, mechanical parts	0.282

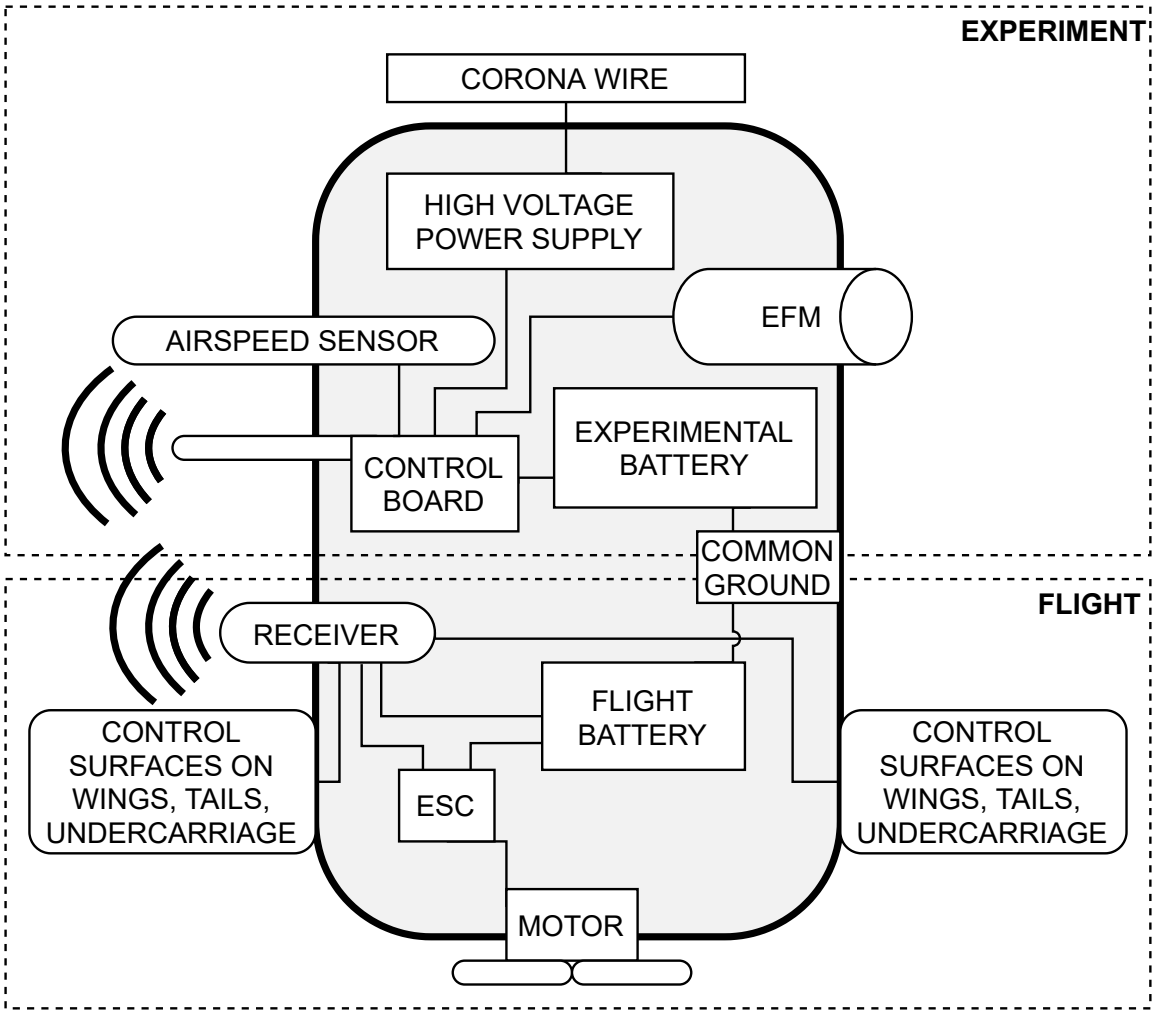

Figure 2-12: Diagram of the test vehicle outfitted with components to meet the requirements. The two main subsystems are the flight system, which drives the plane and ensures it is in the air safely, and the experiment system, which is being used to quantify the charging behaviors. Both systems full functionality are critical to the success of the mission.

2.4 Flights

2.4.1 Pre-Flight Checklist

The following checklist is used to ensure that the system is operating nominally, and is ready for a flight experiment.

- Ensure flight, experimental, and transmitter batteries are fully charged.
- Clean corona wire with Acetone.
- Clear SD Card.
- Ensure all control surfaces are trimmed to center.
- Verify all linkage stoppers are tight.
- Verify undercarriage is well secured.
- Ensure all surfaces of the plane are electrically conductive using ohmmeter, including extremities.
- Ensure the EFM ground, radio ground, telemetry ground are all connected to the conductive skin.
- Ensure the propeller is secured tightly to the motor.
- Ensure flight and experimental batteries are fully charged
- Ensure all components in the plane are well secured with velcro.
- Verify the center of mass on the plane is adequate.
- Verify no rain is expected and wind speeds are below 5 m/s.

2.4.2 Flight Testing Procedure

The testing procedure is outlined below. 2 people are necessary for each flight test: a pilot (P), who will operate the plane; and ground control (GC), who will operate the telemetry ground station. In case of emergency or uncertainty, the default procedure will be to first attempt to land the plane as soon as safely possible. Once the plane is landed, use caution in approaching the plane, and if uncertain about the charge on the surface,touch the plane with a ground stake inserted in the ground to ensure the plane is fully discharged before handling it. In all the tests conducted this was never necessary, because the plane fully discharges as soon as it makes contact with the runway.

1. P & GC: Double check that pre-flight checklist is complete.
2. P: Connect flight battery to ESC. This will power ON all servos, the flight radio, and the motor.
3. P: Connect experimental battery to timer. Once it is, the telemetry control board will stay ON for 30 minutes.
4. GC: Verify good signal from telemetry.
5. P: Place the plane on the downwind side of the runway, pointing up wind.
6. GC: Turn the high voltage ON, verify nominal operation, and then turn the high voltage OFF.
7. P: Notify other pilots and pedestrians by yelling "TAKING OFF!"
8. P: Check runway is clear, and take off when ready. The 10 minute flight time begins.
9. P: Once in the air, assume a steady level flight path, and notify GC when ready to begin high voltage experiment.
    - Flight paths were typically 30s long steady loops around the flight field.

10. GC: Send commands to the plane to test charging or discharging.
    - Charging and discharging times were typically between 1 and 4 minutes at each charging level, depending on the test.
11. P: When nearing the 9th minute of flight, notify GC to turn HV OFF if not already. Prepare to land.
12. P: At or near the 10 minute mark, land the plane.
13. GC: Save the data.
14. Flight complete!

2.4.3 Summary of Flight Campaigns

All the results in this thesis are from flights performed at Mary Cummings Park in Burlington, MA, and the flight details are shown in Table 2.3. Previous flight tests were performed in September and October of 2020, to practice flying the aircraft, and perfect the data collection system. The data collected in these flights are not reported on here because significant changes to the conductive skin were made (see Section 2.3.1) to the plane in the intermediate time, which can affect the self capacitance of the plane and the electric field mill calibration.

Flights usually lasted 10 minutes, and consisted of charging the plane to up to three different voltage levels. Flights launched and landed on a grass runway of about 100m in length.

2.5 Charging Strategy

The charging strategy is modeled after the previous work of Refs. [41] and [24] and relies on ion emission from a corona discharge emitter in the presence of wind. For these experiments, the ion emitter is a long thin wire because of its reliability and uniformity of the discharge in the positive polarity, and to facilitate comparison to 2D numerical models and wind tunnel experiments in Ref. [24]. The wire is connected to

Table 2.3: Details of the flight tests performed for this study. Approximate atmospheric conditions are obtained from the closest weather station, [22].

Date	#	Test	RH [%]	T [$^{\circ}C$]	wind [m/s]	P [kPa]
Nov. 21 2020	1	negative charging	63	9	1	102
Nov. 21 2020	2	negative charging	54	13	4	102
Nov. 25 2020	1	negative charging	67	4	1	103
Nov. 25 2020	2	negative discharging	67	5	1	103
Jan. 26 2021	1	positive charging	56	-2	4	102
Jan. 26 2021	2	positive discharging	57	1	4	102

the high voltage terminal of a high voltage power supply and the low voltage terminal is connected to the conductive airframe. Both positive and negative power supplies have been tested to generate positive and negative corona discharges respectively. The polarity of the high voltage power supply sets the polarity of the charging strategy.

To charge the plane negatively, the wire is set to a high positive voltage with respect to the plane. When the wire is applied a voltage above its corona inception voltage of approximately 7kV, the air surrounding the wire is ionized and a positive glow corona discharge is triggered. When wind is present, some of the ions are convected away, leaving behind negative charge of equal magnitude. This transient charging phase gradually lowers the plane potential, and correspondingly a larger fraction of the positive ions are attracted back by the competing effects of wind convection and electrostatic attraction. Eventually, a quasi-steady state is reached that corresponds to all the positive ions generated by the glow corona being attracted back to the negatively charged plane. In the absence of other charging or discharging mechanisms, the plane has settled into a steady state phase of charging for a given corona wire high voltage bias and wind speed. The time scale of this process is in hundreds of nanoseconds (given the self-capacitance of the plane tested $\sim$75 pF, and currents of tens of μA and charging voltages of the order of 30 kV measured). These fast transients could not be resolved in this study and the focus is on the steady state charging level reached at different applied voltages and wind speeds, as in [24].

Increasing the voltage applied to the wire increases the amount of charge needed on the plane to attract all the positive ions back to it, and thus increases the level of charging. Increasing the wind speed will also increase the required charge accumulated on the plane, within a certain range before saturation is reached [24]. Charging the plane positively relies on the same principles, and requires a negative high voltage power supply to generate a negative corona, but there are some differences in the discharge behavior of positive and negative corona wires.

The discharge characteristics of positive and negative corona wires are similar to the differences between positive and negative point corona discharges, as described in Section 1.2.1. The discharge behavior seen in this work matches that of previous work studying discharge in high voltage power transmission lines, and has been well studied back to Peek's 1929 book [49]. Figure 2-13 shows the characteristic appearance of the corona discharges used in this study, in the absence of wind, and as imaged with an ultra-violet (UV) sensitive camera and an exposure time of about 30 ms. In the positive case, a uniform DC glow is observed that is stable and steady in time. The negative corona has a non-uniform intensity along the length of the wire and its appearance fluctuates in time. It can also be appreciated that, while at comparable voltages (13 and -13 kV), the luminosity is much brighter in the negative case, which is accompanied by a higher current. This is also shown later in this thesis to occur during flight tests: the negative charging necessitates a much higher current to keep the plane at the same potential, as compared to positive charging.

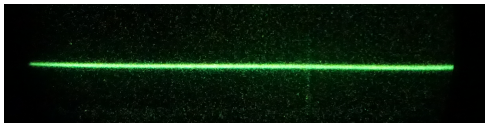

(a) Positive wire.

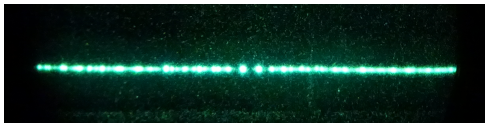

(b) Negative wire.

Figure 2-13: Characteristic appearance of the corona wire emission using a UV-sensitive camera, no wind. (a) Positive corona at 13 kV applied voltage with respect to the wing, and (b) negative corona emission at -13kV.

2.6 Charging and Discharging Results

2.6.1 Flight Data

Figures 2-14, 2-15, and 2-16 show the data collected from the flights listed in Table 2.3. In each flight, four parameters are studied: the commanded voltage, the airspeed, the plane potential, and the corona current. The airspeed was not collected for the Jan 26 flights due to a sensor failure.

2.6.2 Aircraft Charging

The plane potential as a response of commanded voltage is plotted in Figure 2-17, where each flight is broken up into the periods of time when high voltage is ON. In all cases the plane potential increases with the commanded voltage, up to a certain saturation voltage. The saturation is likely a result of spurious corona on the extremities of the plane, such as the wing tips. The plane was brought to 40 kV in the lab to test this hypothesis, and spurious corona were occasionally found. In general, the plane potential reaches a lower magnitude when charging positive (red) than when charging negative (blue), for the same commanded voltage magnitude. In addition, the saturation voltage is approximately 20 kV for positive charging, and 30 kV for negative charging. This difference is likely due to a lower efficiency observed with negative corona wire discharges, as described earlier in Section 2.5. This can also be seen in the much higher current observed when charging positive versus negative, as shown in Figure 2-18. This also demonstrates the lack of dependency of the charging level on the current emitted once the plane reaches saturation. At this point the current only affects the charging rate, not the ultimate magnitude.

2.6.3 Effect of Wind

The dependency of the charging level and emitted current with wind speed is shown in Figure 2-20 for the flights on November 25. The trends observed are consistent with those reported in the wind tunnel experiments of Ref. [24] for the corona wire

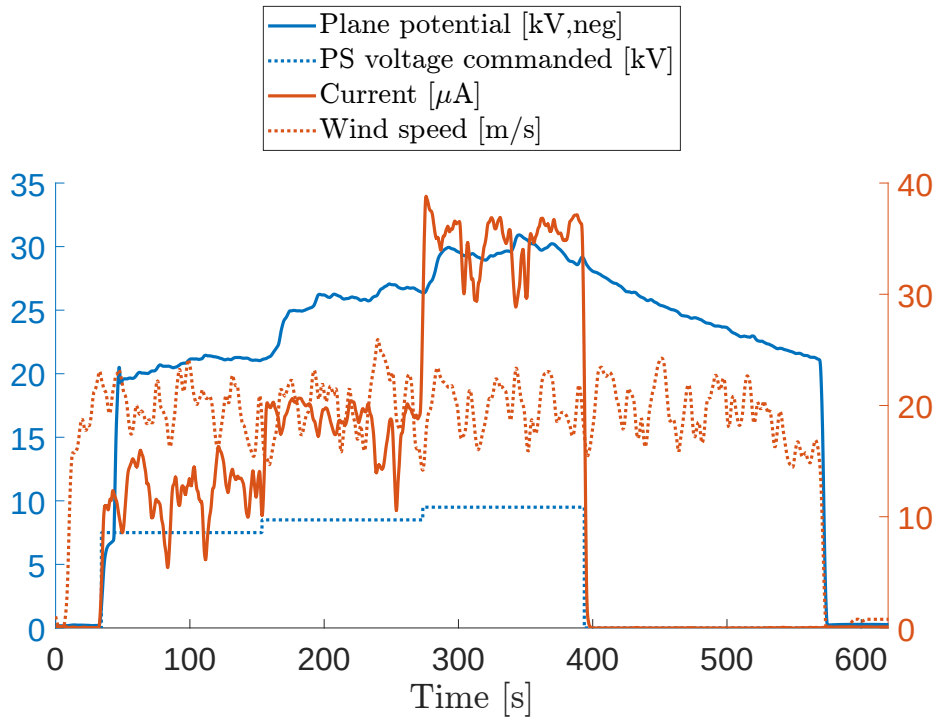

(a) Nov 21 flight 1 (f1)

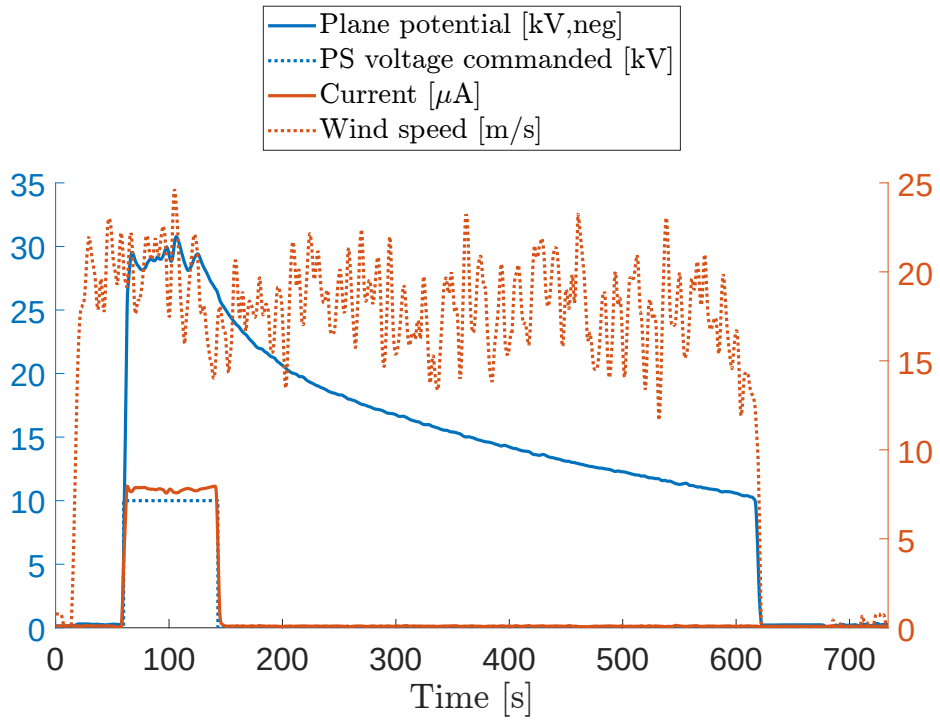

(b) Nov 21 flight 2 (f2)

Figure 2-14: Timeline data from November 21, 2020 flights testing negative charging and discharging.

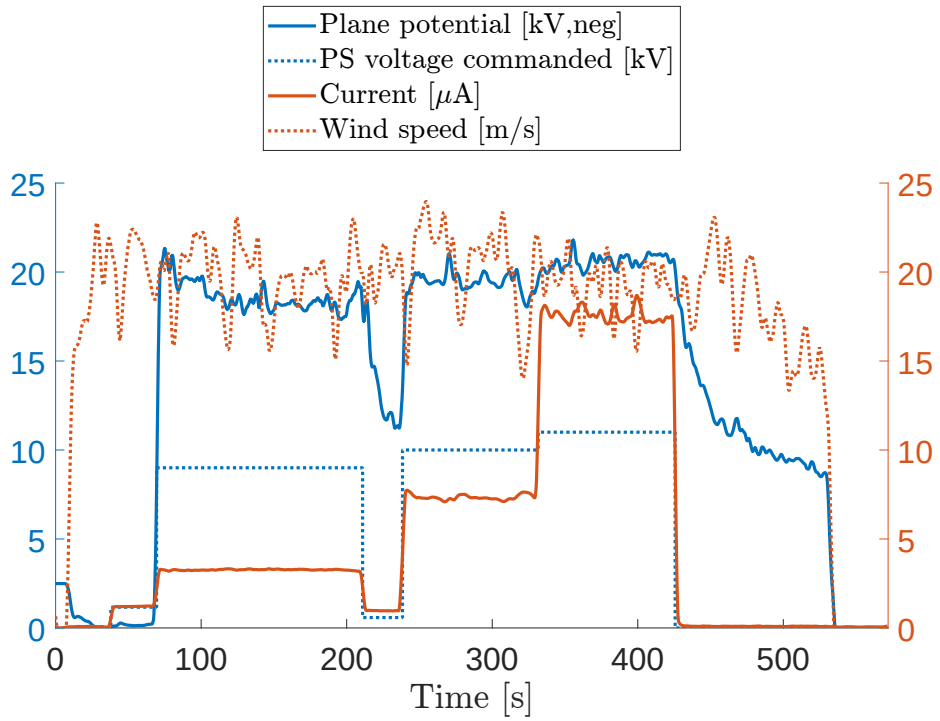

(a) Nov 25 flight 1 (f1)

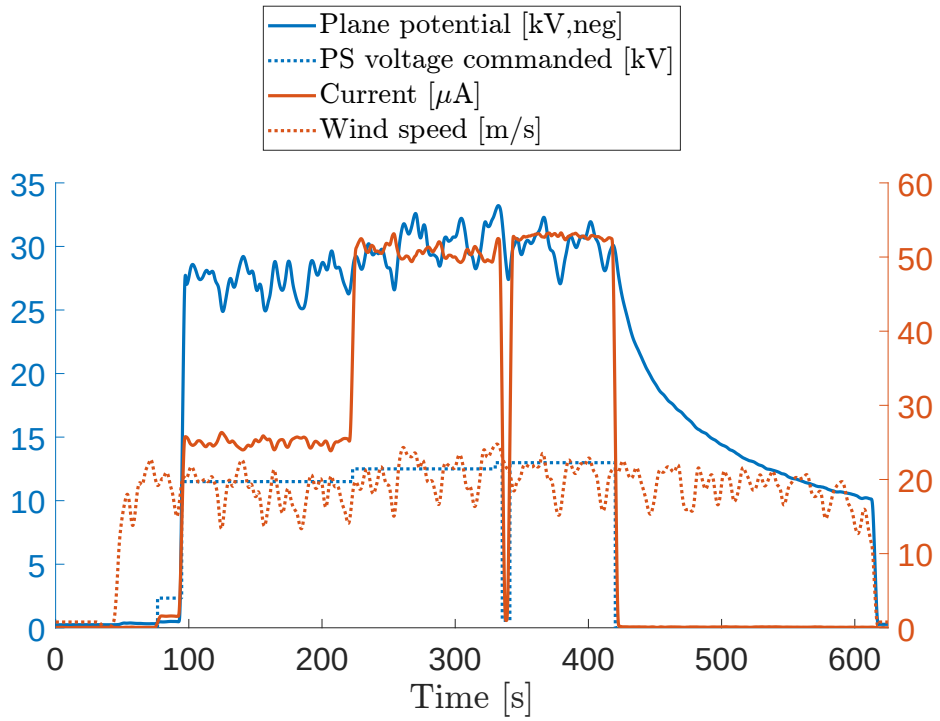

(b) Nov 25 flight 2 (f2)

Figure 2-15: Timeline data from November 25, 2020 flights testing negative charging and discharging.

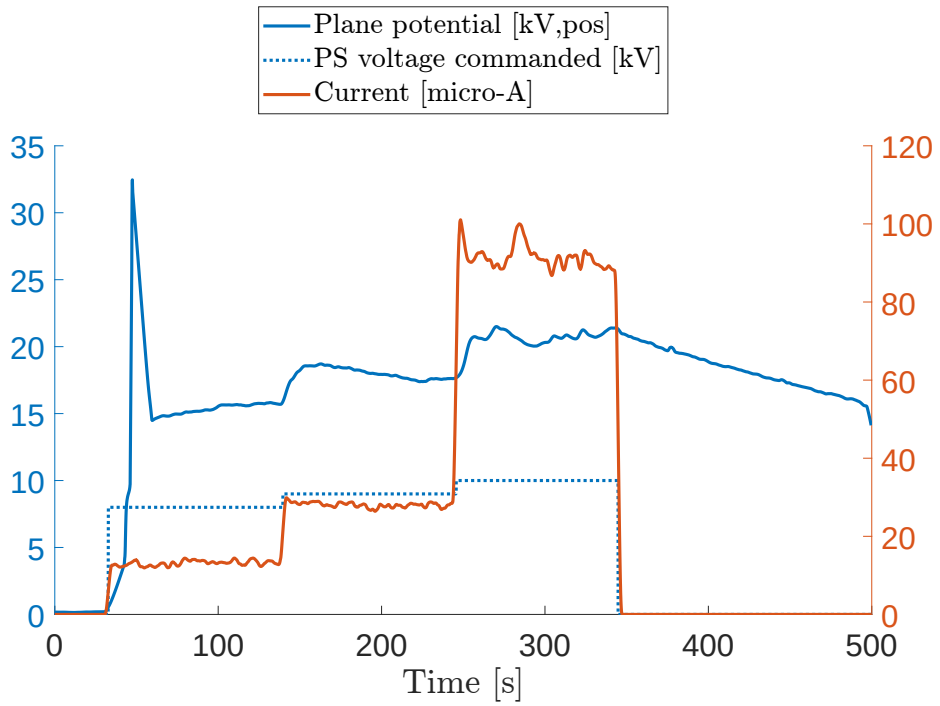

(a) Jan 26 flight 1 (f1)

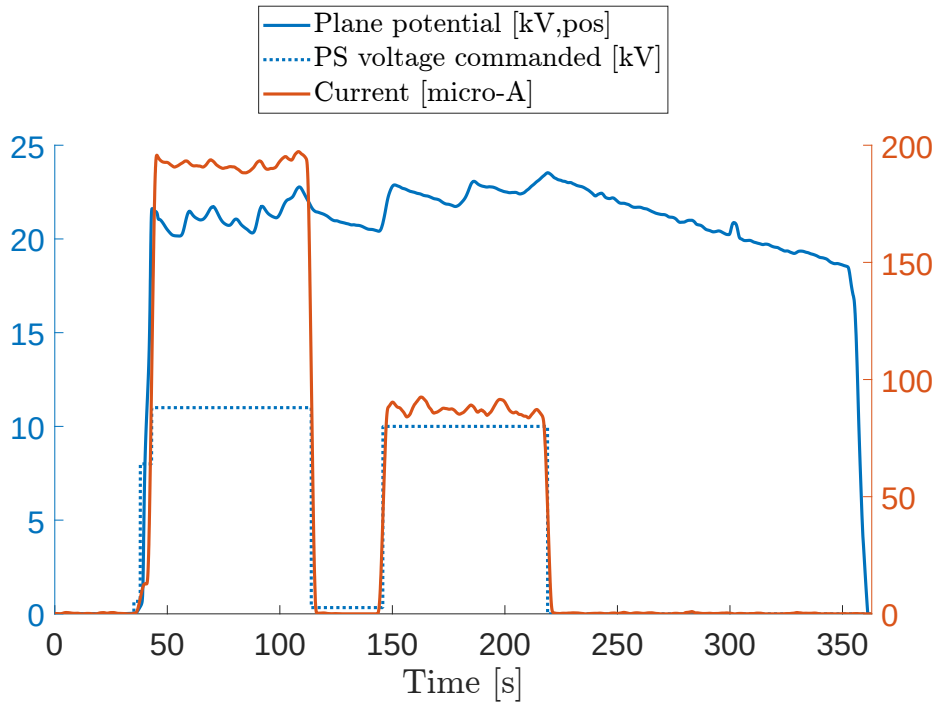

(b) Jan 26 flight 2 (f2)

Figure 2-16: Timeline data from January 26, 2021 flights testing positive charging and discharging.

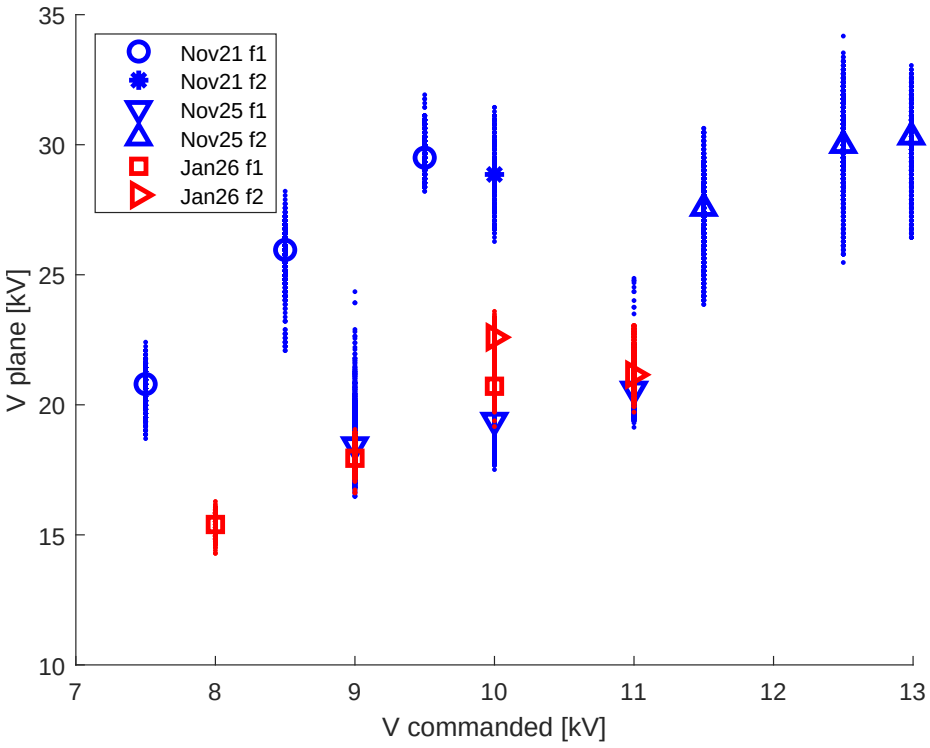

Figure 2-17: Plane potential as a function of the commanded corona wire voltage. The red points represent positive charging, while the blue represent negative charging. The different markers correspond to different flights.

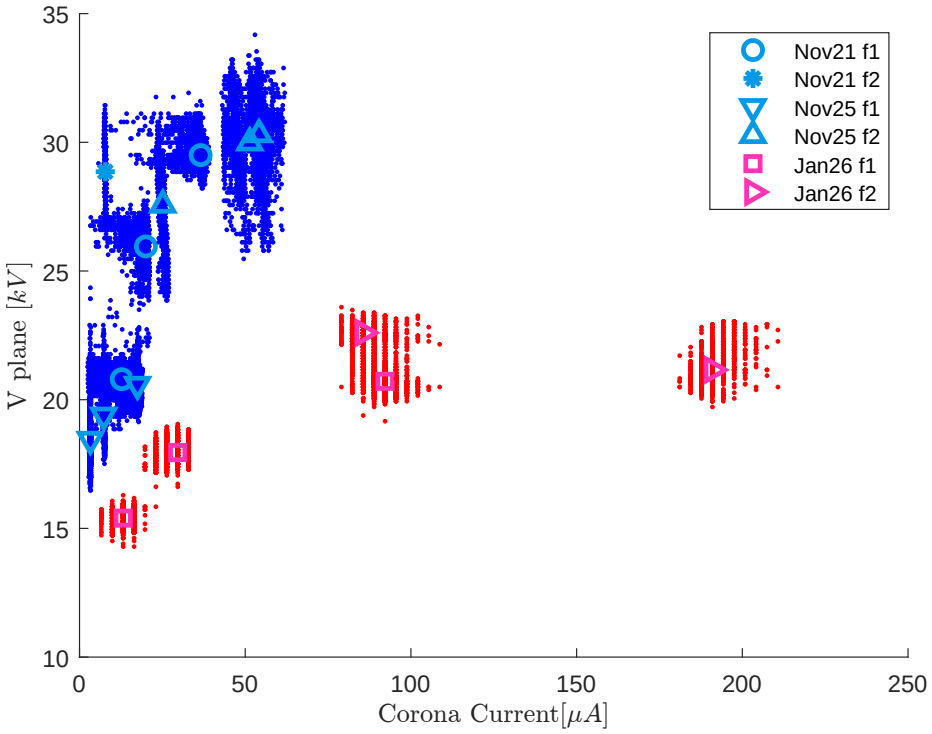

Figure 2-18: Plane potential as a function of corona current. The red points represent positive charging, while the blue represent negative charging. The different markers correspond to different flights.

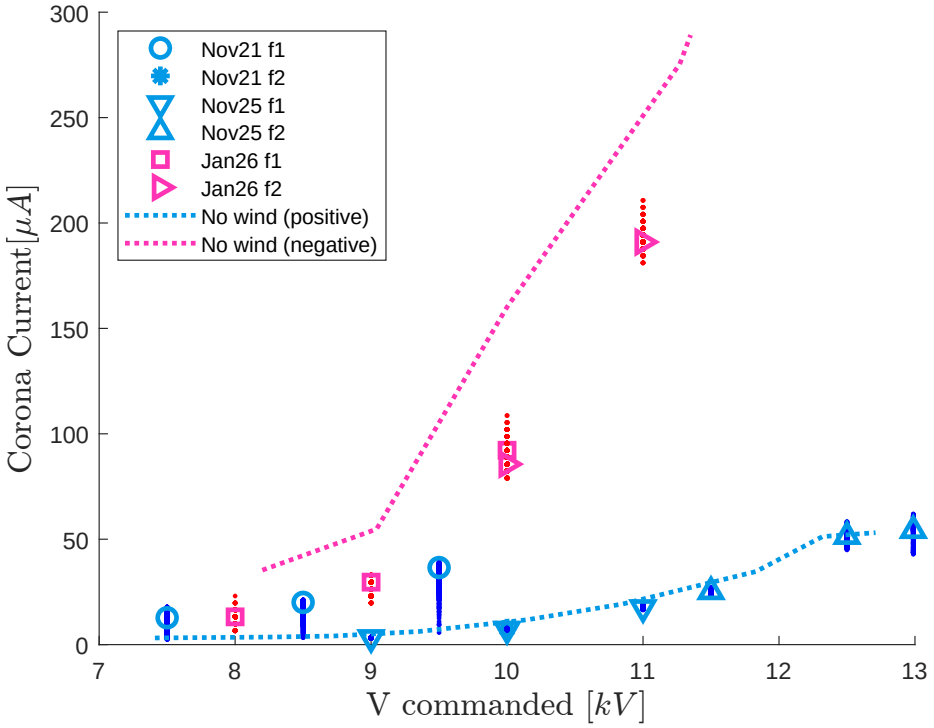

Figure 2-19: Current response to applied voltage to the corona wire, during flight. The blue symbols represent negative charging (positive corona); the red symbols represent positive charging (negative corona). The different markers correspond to different flights. The dashed lines are the reference current-voltage characteristics, as measured in the laboratory in the absence of wind.

operating in the so-called charging-dominated regime. In particular, at the higher applied voltages tested (11-13 kV), the plane potential increases in magnitude as the wind speed increases, and this can be explained by the competing effects of ion convection by the wind and electrostatic ion attraction by the aircraft. The current decreases with the wind speed, since as the aircraft-wire system becomes more negative with respect to the environment, so the positive corona discharge is weakened. Higher positive applied voltages lead to more negative charging levels. At some point, the corona discharge becomes so weak that it is close to extinction so that no further charging can be achieved. This saturation regime is what is observed at the lower applied voltages tested (9-10 kV): the current measured is low, below 10μA, and the plane potential shows no clear dependency with wind speed. The wind tunnel tests in Ref. [24] also showed that the saturation can be overcome by increasing the power supply bias, as observed in the flight campaigns, Figure 2-20.

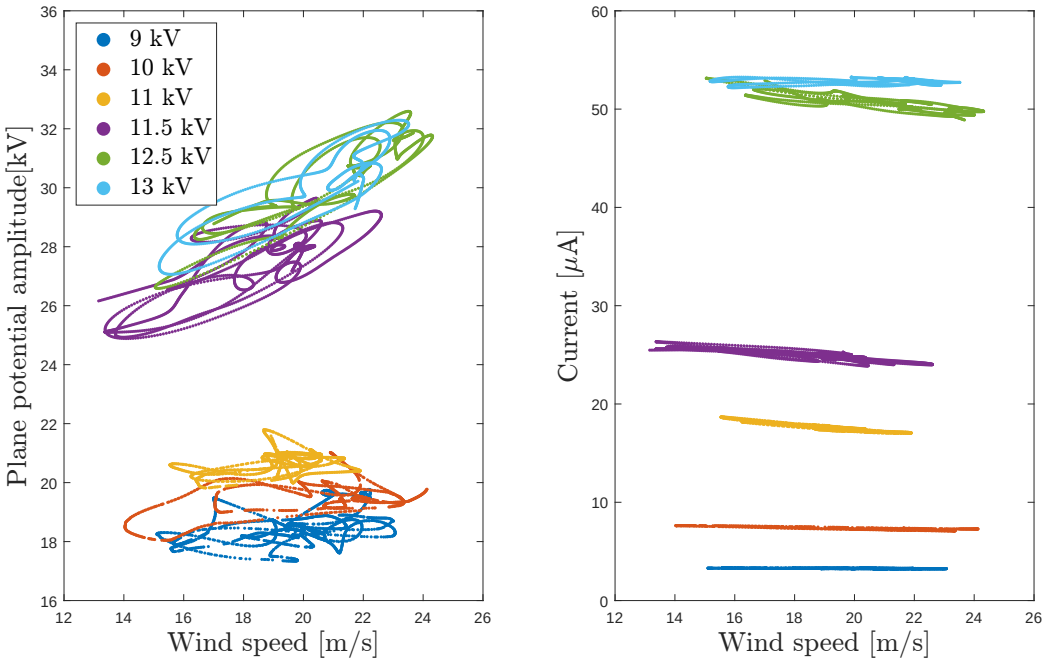

Figure 2-20: Plane potential and corona current as a function of wind speed, for Nov 25 flights. The colors represent the commanded wire potential.

The dependency of wind speed is also shown from the November 21 flights in Figure 2-21, where all charging levels seem to correspond to the saturation limit, showing no dependency on the potential acquired or the current with wind speed.

This earlier saturation with wind speed, combined with the higher plane potentials observed, Figure 2-17, could be explained by a lower ion mobility; which depends on the presence of aerosols, humidity levels and other factors that can not be controlled [32, 29, 28, 17]. Interestingly, the 10 kV applied potential had a lower current than all of the voltages tested in the first flight. We think that this could be due to experimental flight battery losing voltage over the course of the day, resulting in a lower current on flight 2 for the same applied potential. This hypothesis can also be seen by looking at Figure 2-18; both the plane potential and the current of the Nov21 f2 flight are lower than the highest of Nov21 f1.

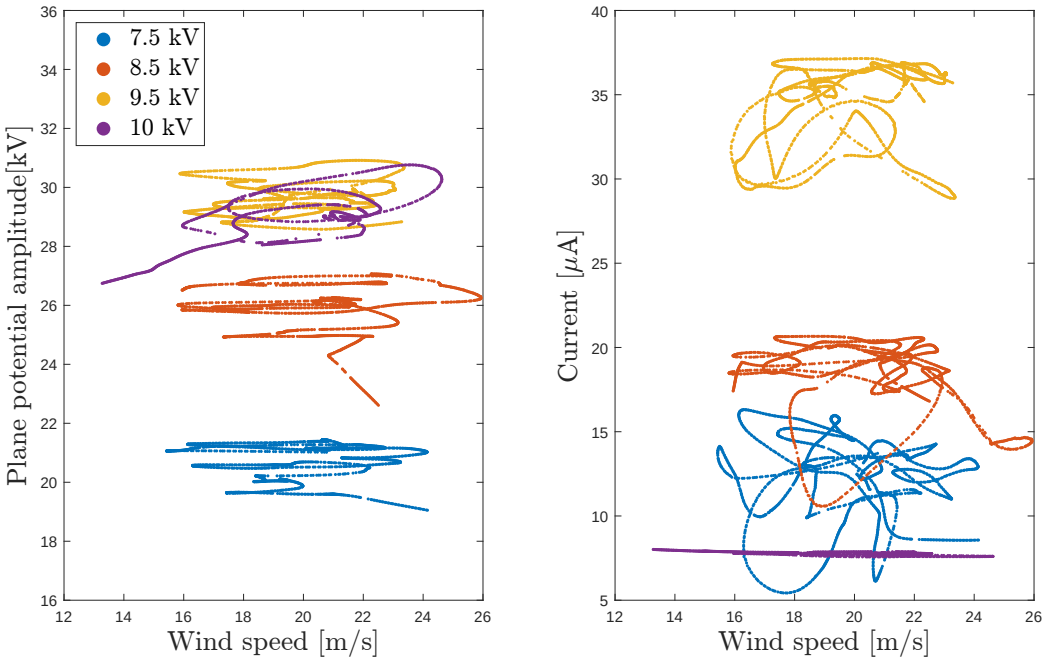

Figure 2-21: Plane potential and corona current as a function of wind speed, for Nov 21 flights. The colors represent the commanded wire potential.

The airspeed sensor was malfunctioning during the January 26 flights that was later determined to be an electrical connection failure, but similar trends are still observed for these flights as shown in Figure 2-22. Despite airspeed magnitudes being uncharacteristically low (due to the malfunction), the expected trends can still be seen: a rise in plane potential and a fall in current with wind speed.

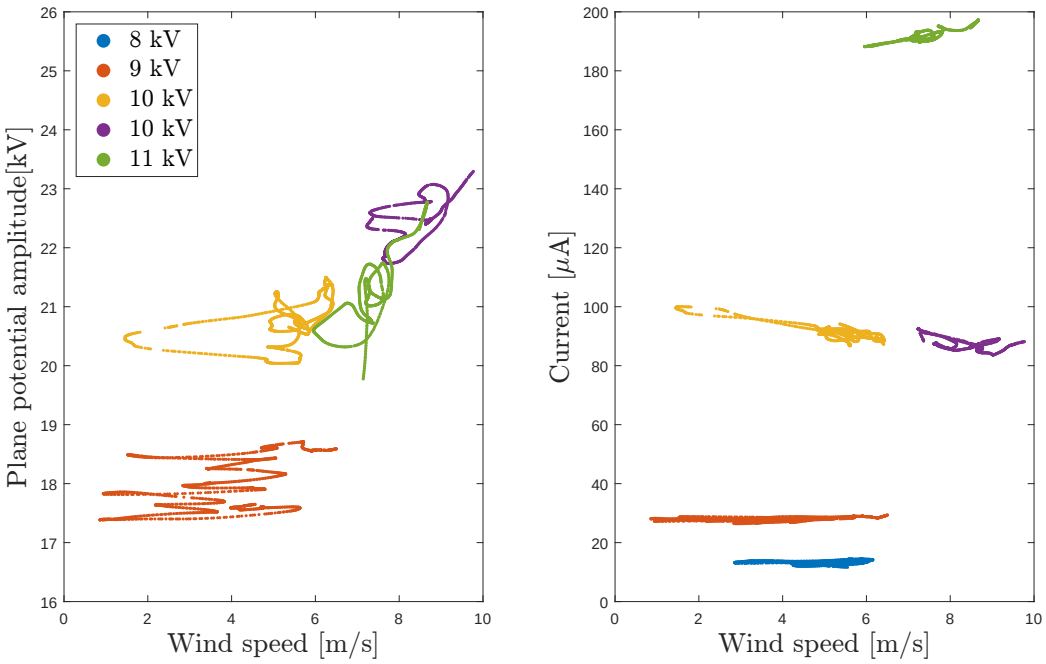

Figure 2-22: Plane potential and corona current as a function of wind speed, for Jan 26 flights. The colors represent the commanded wire potential.

2.6.4 Aircraft Discharging

As the high voltage is turned OFF, the plane's charge decays exponentially as shown from t=400 to t=570 in Fig. 2-14 (a). This decay can be explained as the discharging rate of a capacitor (the plane) to a resistor (the atmosphere). Assuming an RC circuit where the resistance R is given by the atmospheric properties and the capacitance C is the self-capacitance of the plane, the change in potential over time is given by:

$$V_p = V_s \cdot e^{-t/\tau} + D \tag{2.1}$$

where $\tau = RC$ is the time constant or characteristic discharging time, V_p is the plane potential, V_s is the initial plane potential, and D is a constant to account for possible deviations from the calibration conditions. As an order of magnitude, the capacitance C can be estimated using the model from Ref [26] and scaled by the 1.9 m wingspan of the plane, to give $\sim 75pF$. The resistance is $R = \frac{L}{A\sigma}$, where $L \sim 0.1m$, is taken as a characteristic length for potential decay given the geometry of the aircraft, $A \sim 2.6m^2$ is the estimated surface area of the plane again derived from the model in

Ref. [26], and σ is the electrical conductivity of air at sea level, which is $\sim 10^{-14} Sm^{-1}$ [53]. A characteristic time constant is expected to be $\tau \sim 290s$.

Figure 2-23 shows the discharge over time curves from each flight and Table 2.4 shows the discharge time constants of those flights, based on exponential fits to equation 2.1.

A factor of 4-10 difference is observed in the time constants for flights of different days. This may be result of the inverse relationship between the time constant τ and the conductivity of air. The conductivity of air, $\sigma \approx q\mu_q n_q$, is proportional to the number density of ions (n_q) and their mean mobility (μ_q), with q being the electronic charge. The lower discharge rates measured on November 25, compared to November 21, indicate a higher electrical conductivity of air which can be explained by higher charge concentrations or higher mobility of the charge carriers. Higher concentrations of ions in the atmosphere can be a result of lower aerosol, smoke nuclei or particulate concentrations (which in turn result in lower ion attachment rates to aerosol particles) [17]. Higher mobility of ions can be expected, for example, for lower humidity levels, with a clear trend in the case of positive ions and a less clear one for negative ions [32, 29, 28].

Table 2.4: Discharge time constants.

Date	Flight #	τ [s]
Nov. 21 2020	1	230
Nov. 21 2020	2	234
Nov. 25 2020	1	24
Nov. 25 2020	2	54
Jan. 26 2020	1	518
Jan. 26 2020	2	294

2.7 Discussion

The flight experiments reported in this thesis have tested the charge control strategy on a small aircraft, flying at low altitude and low speed. Under these conditions, net

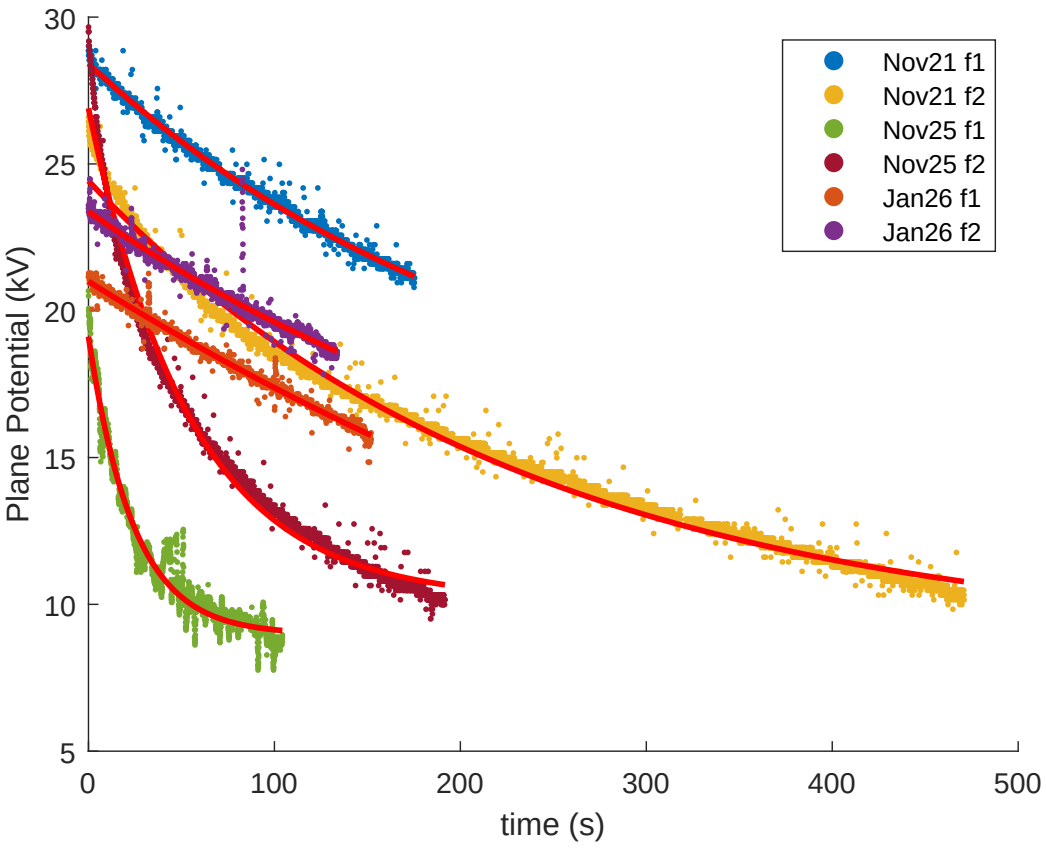

Figure 2-23: Discharge curves for each flight, each one fitted to equation 2.1.

charging of the vehicle to levels that would have a measurable reduction on the risk of lightning [48] were achieved, while posing no alteration to flight operations or other electronics on board. The following section discusses expected scaling with vehicle size and altitude, as well as high wind speed effects.

The effect of altitude (or air density) on the net charge level acquired through ion-emission by corona discharge in wind was discussed in Ref. [24] and is driven by differences in net ionization rates of air (and corona inception thresholds) as well as differences in ion mobility. Roughly, the corona breakdown field scales proportional to the air density and the ion mobility inversely to the air density. Below saturation (see Figure 2-20), flying at altitude decreases the efficiency of ion convection by the wind since a higher ion mobility necessitates lower aircraft charging to balance the wind drag. Note that when flying at 10 km altitude, the ion mobility will be about three times higher than at sea level. However, when saturation is reached because the corona is significantly weakened, this effect disappears, and relative air density changes should not modify the acquired aircraft potential [24]. Therefore, when flying at higher altitudes, the maximum net charge (or saturation level) will be comparable but will be reached while flying faster (since a driving parameter is the relative value of wind speed to electric drift speed) and will require a lower applied voltage of the power supply.

As discussed in section 2.5, the electrostatic potential acquired by the aircraft relative to its environment, or likewise the net charge, is set by the competing effects of ion convection by the wind and electrostatic attraction. Given similar local electrostatic conditions, the electrostatic potential will remain unchanged. E.g. if the aircraft had a wing that was 50% longer but otherwise the location of the wires was kept unchanged, the same plane potential will be achieved. However, the net charge (proportional to the capacitance and therefore a characteristic length scale) would increase accordingly; and the current emitted will also be proportional to the length of wire used. When considering a geometrically similar but larger aircraft the location of the wire needs to be selected considering the following trade-off: if the wire is very near the airframe surface, ions are easily captured and the aircraft charge

level will be limited; if it is very far, the corona weakens too much. In addition, locations further back toward the trailing edge lead to more charging, since ion escape is facilitated. Therefore, the wire would be placed at a comparable distance from the wing surface for both planes (not scaled with size) and the electrostatic potentials developed are expected to be similar. The net charge would however scale with size: e.g. an aircraft 10 times larger would acquire the same potential but 10 times the charge. This scaling is consistent when comparing the estimated charge acquired by the 2 m wingspan vehicle of this thesis, of ~ 2 μC, to that acquired by the 10 times larger SPTVAR vehicle when using controlled corona emission, of ~ 20 μC [31].

Note that this scaling with size presents a limitation when considering the charge control system for lightning strike risk reduction. In this case, the optimum aircraft electrostatic potential in terms of lightning risk reduction scales linearly with size (and the net charge scales quadratic with size). While the net charge control strategy based on corona discharge explored in this thesis is expected to have a measurable influence on the triggering of lightning for a small vehicle, alternative charge emitting devices should be explored for larger aircraft. This magnitude of charge compensation is already adequate to protect personnel against electrostatic discharge, even for large vehicles, as the stored energy is proportional to size so at the same acquired potential the stored energy, and hence the risk, is higher.

The discharging rates to the atmosphere, while considering no external sources from non-electric propulsion systems or spurious corona discharges, scale as $\tau^{-1} = (RC)^{-1} \sim \epsilon_0^{-1}\sigma$. This scaling shows that the dependency with vehicle size cancels out and only the atmospheric conductivity plays a role. Note that ϵ_0 is the permittivity of free space. Two geometrically similar aircraft would therefore have similar discharging rates to the atmosphere, but an aircraft flying at high altitude would discharge more rapidly than an aircraft flying at low altitude since the conductivity increases with altitude [27]. E.g. when going from 0 km to above 10 km of altitude, the conductivity increases from $\sim 10^{-14} Sm^{-1}$ to $\sim 10^{-12} Sm^{-1}$ [27] so the discharging rates would increase by a factor of 100. This independence with size is confirmed by the similar order of magnitude reported by measurements on ground of the discharging time

constant of the SPTVAR aircraft with the engine off being $\sim$ 300 s (comparable to the ones reported in this thesis) despite the much larger wingspan of 18 m [31].

2.8 Conclusions

The experiments reported in this thesis have demonstrated key milestones for the use of bipolar ion emission from the aircraft surface to control the net charge of the vehicle. These milestones include remote operation and control of the net charge during flight; safe operation of a highly charged aircraft during fair weather; and exploration of parameter dependencies by comparison to preceding wind tunnel studies. Both charging to negative levels and positive levels were demonstrated, by using positive and negative corona discharges respectively. The differences between polarities were revealed including higher consumed currents and lower acquired voltages for the positive charging strategy as a result of the lower efficiency of the negative discharge and the higher mobility of the negative ions. The dependencies with applied voltage bias and wind speed were consistent with observations in the wind tunnel: charging increases with applied voltage bias; and both a regime with increasing charging in wind speed and a saturation regime were observed [24]. Once the charging system was turned off the aircraft discharged to the atmosphere following an RC law, with the time constant being comparable for the positive and negative polarity.

The results also indicate some of the technological limitations of the system. First, for both the positive and negative charging schemes, the aircraft seems to reach a saturation voltage close to + 23 kV (positive charging) and -30 kV (negative charging), even if the commanded voltage was increased. This saturation may be due to spurious corona forming at the sharp points of the plane such as the nose, tail, and wing tips, although this hypothesis could not be confirmed. Such a threshold would indicate that the ion emitter current can not compensate the leakage current from these sources. In addition, the use of corona wires for ion emission was selected here for a comparison to the numerical model and wind tunnel experiments in Ref. [24], however a production system will require a robust ion emitter less prone to damage and increased drag.

The applicability of a charge control system for aircraft lightning risk reduction or precipitation static mitigation has yet to be fully explored. In particular, a flight platform that can fly in a more representative environment, including flying at high altitude or within relevant thunderstorm environments would be desired. Future work should make use of a research aircraft to demonstrate lightning risk reduction by using multiple electric field mills to detect the environmental electrical conditions in thunder clouds and the net charge of the vehicle, and provide a closed-loop control of the net charge based on an estimated requirement. As mentioned in the introduction, net charge control could also be of use to compensate for natural charging in certain airborne vehicles, such as rotorcraft, to ensure safety of boarding passengers. In addition, net charge control can be of value to research aircraft measuring atmospheric electric fields.

Novel aircraft systems offer another opportunity for this technology, but also pose a challenge. Blended wing airplanes, Vertical Take-off and Landing (VTOL) and multi-rotor aircraft, and advanced materials like carbon fiber reinforced plastic (CFRP) are just beginning to be implemented and taken advantage of in the aerospace industry. For the purposes of this work, many assumptions were made, like a fully conductive, standard geometry airframe, but in reality these assumptions may not hold up to complex new aircraft systems and airframe materials. In addition, this system must be proven in the dynamic nature of the atmosphere: the electric field, temperature, pressure, humidity, and aerosol levels are constantly changing as an aircraft travels quickly through it. These parameters will affect the charging and discharging, and the lightning mitigation as discussed above, and future work should focus on which of these parameters will need to be sensed and in what resolution (spatially and temporally) to provide a closed system.

Chapter 3

Wind Tunnel Experiments of Streamer Corona

This chapter includes a detailed summary of the research investigation of the discharge behavior of a point-to-plane corona discharge in the presence of wind.

The motivation behind this wind tunnel testing is to provide a first step towards studying the discharge of p-static wicks, which are used to discharge an airplane of its net electrical charge, which accumulates naturally and can cause radio interference. The current standard testing procedure for these dischargers does not account for the discharge changing due to wind [4]. A standard commercial p-static discharger is shown in Figure 3-1, which was manufactured by Dayton-Grainger. In this work a simplified discharger geometry is studied up to wind speeds of 30 m/s (67 mph). A sharp needle of .174 mm tip diameter is applied a voltage ranging from 6-18 kV and is separated 25 mm from a ground plate. The tests described in this thesis have shown that wind significantly alters the discharge characteristics, such as the electrical current, the frequency of pulsations, and the shape of the streamer corona. While the behavior of glow corona in wind has been addressed in numerous works [15, 16], studies of streamer corona in wind are mostly absent from the literature. The remainder of this chapter will describe the experimental setup and discuss the results of this study, and will conclude with recommendations for future work.

Figure 3-1: Standard p-static discharger wick used on commercial aircraft, manufactured by Dayton-Grainger.

3.1 Experimental Setup

The experimental setup is shown in Figures 3-2 and 3-3. A 46x46 cm open-return wind tunnel with air-speeds up to 30 m/s is used. An airspeed sensor was used to verify that the wind tunnel produces an even distribution throughout the test area. The needle is supported on an insulating stand 25 mm from an aluminum ground plate of 203 mm diameter and 6.35 mm thickness. The tip, power supply, electrical measurements, data acquisition system, and imaging system are all described in the following sections.

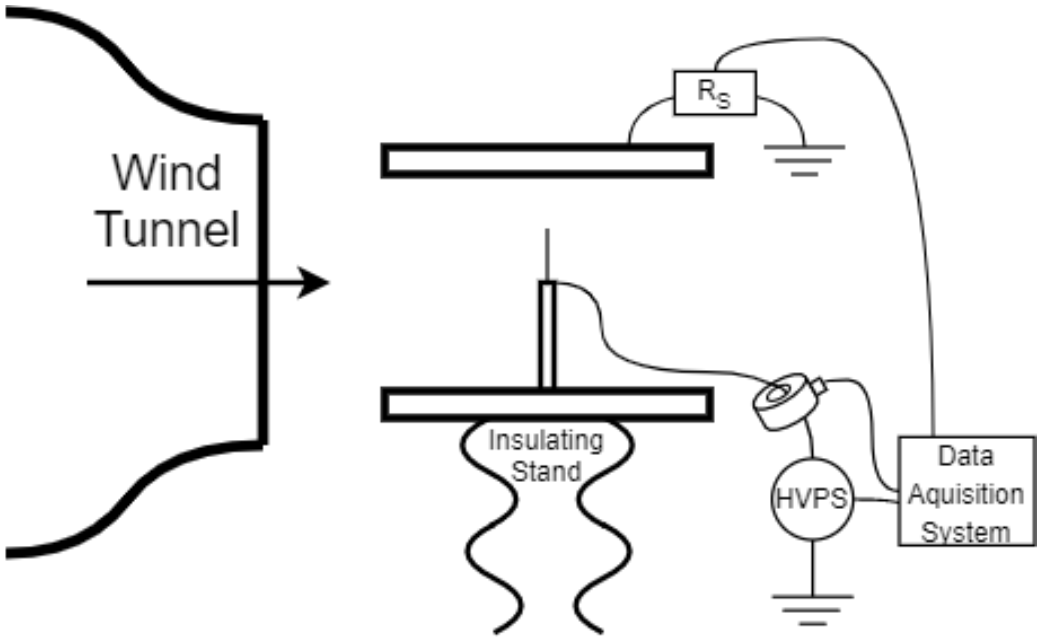

Figure 3-2: Experimental apparatus for the wind tunnel experiments. The PMT and the ICCD Camera are not shown for clarity.

3.1.1 Tips

Before settling on a tip geometry (diameter and gap distance), several were tested, with the goal of making repeatable and interesting observations. Over the course of the preliminary testing, several trends were observed that are not reported here quantitatively. First, a larger diameter tip ($\gtrsim$ 2mm) and tips that are closer to the ground plate ($\lesssim$ 10mm gap) typically emit burst or onset streamers at a narrow

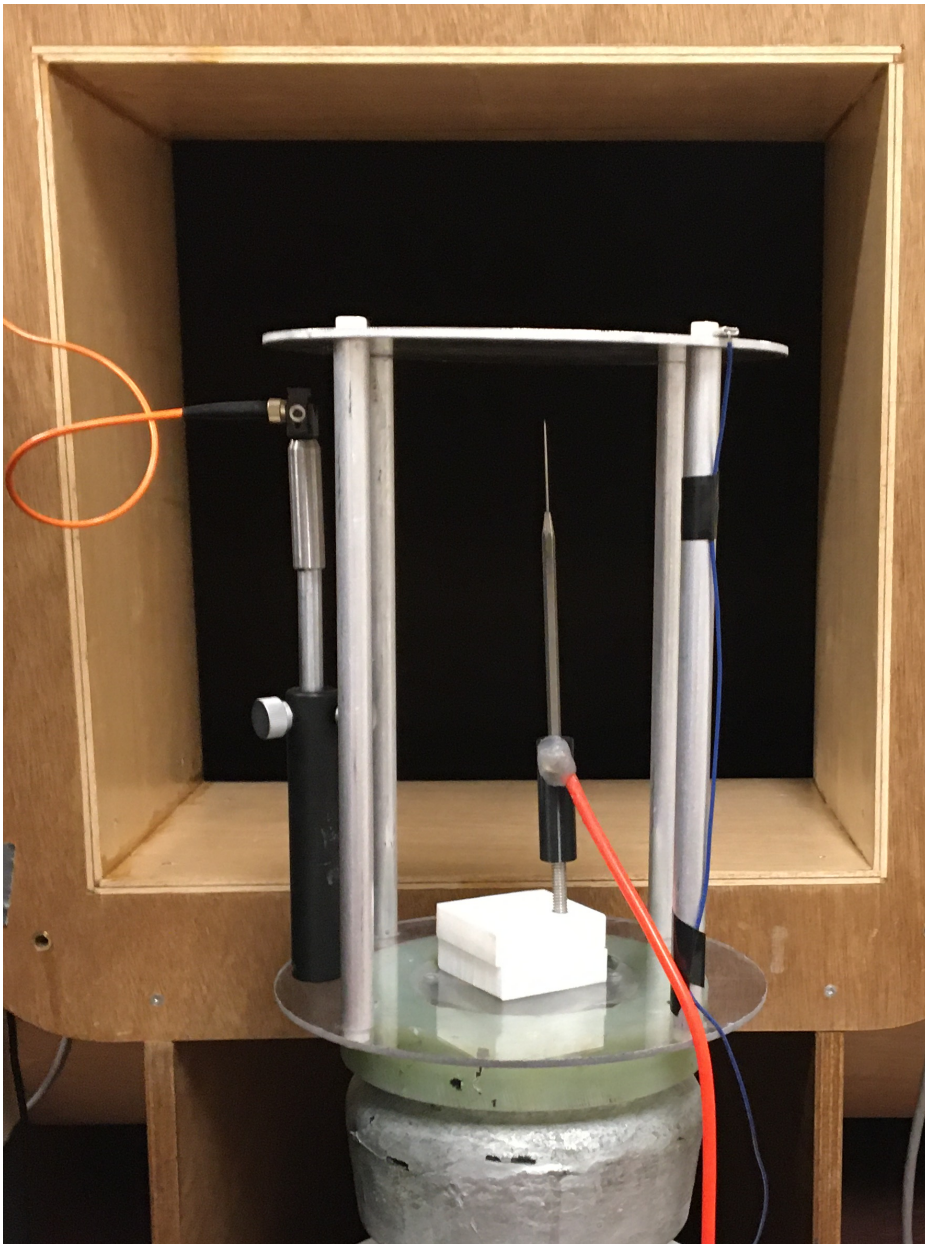

Figure 3-3: Photograph of the experimental set-up for the wind tunnel experiments. The orange cable is a fiber optic cable for the PMT measurements, the red cable is the high voltage wire, and the blue cable is the ground wire.

range ($\lesssim$ 1 kV) of voltages. Any higher voltages will induce a glow corona, until a sufficiently high voltage is placed to create an arc across the gap. Smaller diameter tips ($\lesssim$ 2mm) and tips that are further from the ground plate ($\gtrsim$ 10mm) tend to have a larger range of voltages at which the streamer regime is seen, and fewer glow-only corona regimes. All the tip materials tested, including aluminum, 1018 steel, and stainless steel, corroded after several tests, as shown in Figure 3-4. Tip corrosion is a common phenomenon that can occur in as little as several hours of corona discharge for many types of materials, including stainless steel. This is an ongoing research area and challenge for technologies that utilize corona discharge in air [30, 47]. The corrosion is likely a result of NO_x generation in the discharge, and $-NO_3$ ions that form near the emitter surface can cause pitting corrosion on the electrode surface [23].

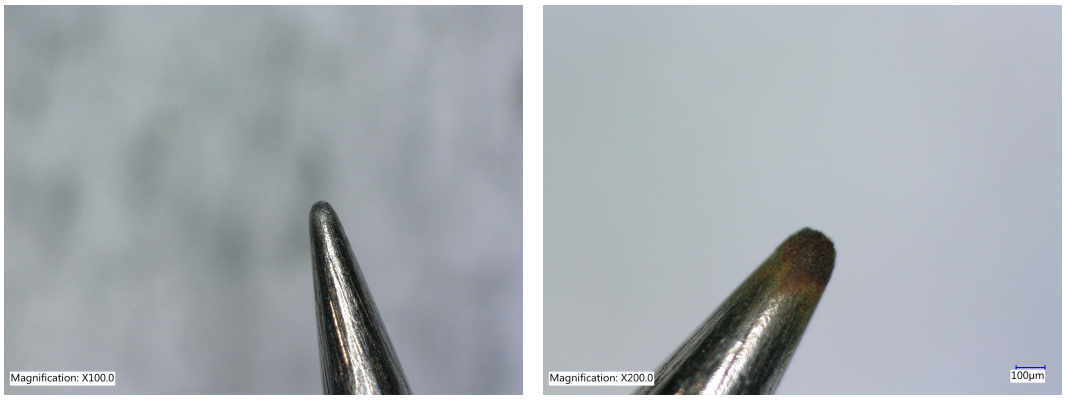

(a) Cleaned tip (b) Tip after several days of testing

Figure 3-4: Magnified photos of the 0.174 mm diameter tip used for the experiments. (a) shows the tip at 100x magnification after recently being cleaned with baking soda. (b) shows the tip at 200x magnification after several days of testing with an orange layer of corrosion. The corrosion does not seem to impact the shape or behavior of the discharge. The corrosion may be due to excessive build up of heat on the stainless steel.

Ultimately, the tip reported on in this thesis is a 0.174 mm diameter stainless steel needle, as shown in Figure 3-4. Corrosion did build over time, but did not appear to greatly alter the surface geometry or the observed discharge behavior. It is expected that in the future a regular cleaning procedure must be established so that the corrosion does not build enough to increase the diameter significantly.

The needle tip can also be negatively impacted by dust/particle accumulation.

Before each test a strict cleaning procedure using a fresh micro-fiber clean-room cloth and acetone is observed to reduce the likelihood of particulate on the tip. This cleaning procedure was tested by checking for dust particles using a 200X microscope.

The needle is suspended on a ceramic insulating stand and is supported by a 3D-printed PLA plastic clamp, with height adjustability. The gap distance is adjustable but for these tests was set at 25 mm and is measured using calipers. The high voltage wire is connected using a set screw, which is coated in silicone putty to prevent spurious corona, shown in Figure 3-3.

3.1.2 Power Supply

A Matsusada RB60-30 DC high voltage power supply was used to vary the applied voltage to the tip from 0 to +30 kV. A small control box was built to operate it. The electrical current and voltage outputted by the power supply (not time-resolved) are measured using the data acquisition system.

3.1.3 Electrical Measurements

The time-resolved electrical current is measured both going to the needle using a Pearson 2877 Rogowski coil and the current coming from the ground plate by measuring the voltage across the shunt resistor of 180 Ω. An Oriel 7734X photo-multiplier tube (PMT) was used to measure the intensity of light over time, however damage to the sensor caused a decay time much longer than specified and is only used for comparative purposes to confirm the pulsation frequencies as measured by the current sensors.

Figure 3-5 (b) shows a sample of the diagnostics from one streamer discharge test, using 16 kV applied voltage and 0 m/s wind, including the supply current, ground current, and PMT signals over time. The peaks of the ground signal are shown with downward facing triangles. These were detected using MATLAB's peak-finding algorithm. Also shown in Figure 3-5 are a single streamer burst as measured by the electrical diagnostics (a), an ICCD image of a single streamer burst (c), and a

superposition of many ICCD images of single streamer bursts (d).

From these figures it is clear that the PMT decay time is much longer than was expected, likely due to previous damage to the sensor. Arcanjo et al. [8] shows that a streamer corona in a similar set-up should illuminate the PMT in similar time-scales (rise and fall time) to the electrical current waveform. The two current signals convey well the time-scales involved, and is consistent with previous work showing the rise time of 10s of ns and the decay time of 100s of ns [8].

A time-resolved high voltage probe (Lecroy PPE 20kV) was used verify that the voltage did not vary significantly during streamer corona. The results of this test are shown in Figure 3-6; the small oscillations of 10 V can be considered negligible compared to the total voltage of 16,000 V.

3.1.4 Data Acquisition

The electrical signals reported on are measured by a WaveRunner 9000 Teledyne oscilloscope (4 GHz bandwidth). The data acquisition rate is $50 * 10^6$ Hz for 200 ms, which corresponds to 20 ns period and a total of 10^6 samples for each test. At a pulsation frequency of 4 kHz, around 800 streamers are sampled. Note, a BNC P4017 oscilloscope (100 MHz) was used to collect the results displayed in Figure 3-6.

3.1.5 Imaging

Like the tip geometry, the imaging setup underwent several revisions to get to the final configuration used to capture the results obtained in this thesis.

A summary of the camera trials is provided in Table 3.1

Due to the fast and repetitive time scale of the streamers ($\sim$1-10 kHz), a high speed camera (Edgartronic SC2+) was used to capture individual streamer pulses, however with all lens configurations attempted, the visible light was too dim. A UV intensifier, the Syntronics Corona Finder, was used briefly however the P43 phosphor has a decay time of 1.5 ms, which is much longer than the expected period between streamers (10-100 μs), so multiple streamer bursts were seen in each image. Since

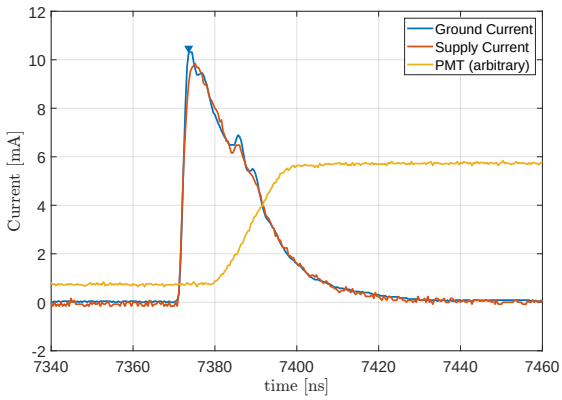

(a) Electrical measurements of a single streamer burst.

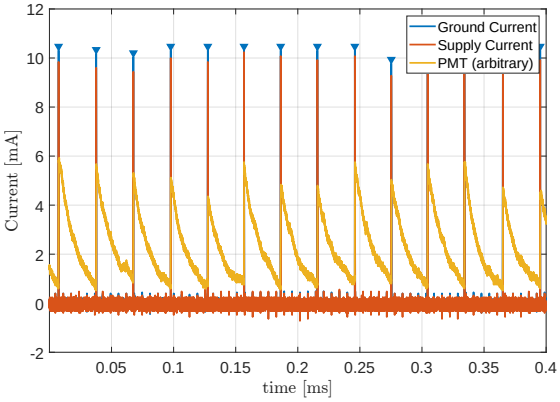

(b) Electrical measurements of 14 consecutive streamer bursts.

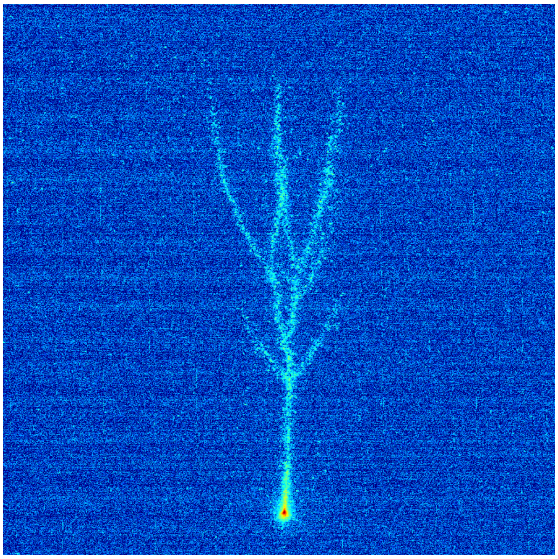

(c) ICCD image of a single streamer burst.

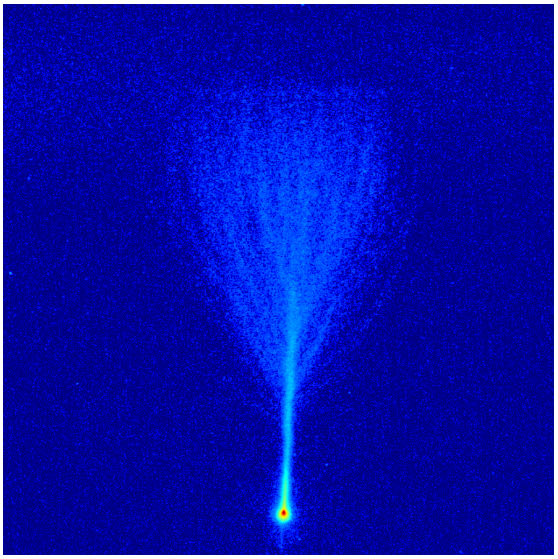

(d) 100 images superimposed

Figure 3-5: Sample of diagnostic capabilites, for an applied voltage of 16 kV, and 0 mps wind speed. (a) The supplied current, ground current, and PMT signals over time for a single streamer burst. (b) A 400 μs sample of a test, with 14 consecutive streamer bursts. The peaks of the ground signal are shown with downward facing triangles. (c) An image of a single streamer burst using the ICCD Camera. Exposure time 150 μs and Gain 24. (d) 100 ICCD images like (c), superimposed

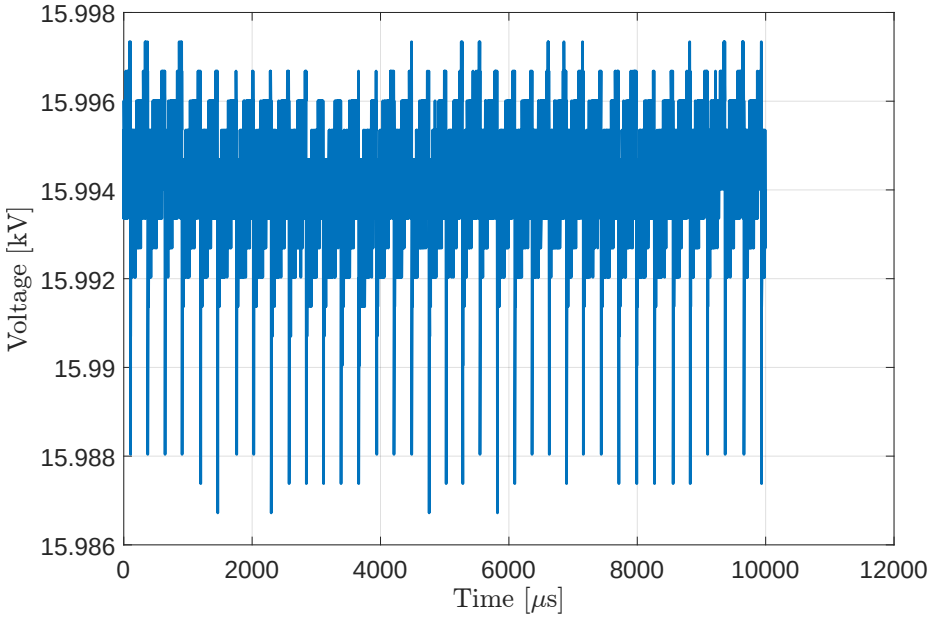

Figure 3-6: Signal from the time-resolved high voltage probe during a 16 kV, 0 m/s wind test. Small oscillations are observed of ∼10 V and can be considered negligible compared to the total voltage of 16,000 V.

Table 3.1: Summary of the camera lens trials for imaging streamers.

Optics	**HS Camera**	**ICCD**
UV lens	Not enough light	Very low resolution
UV lens + Intensifier	Can not Focus	
UV lens + Intensifier + 50mm lens	Good focus and light, intensifier decay time = 1 ms	
50 mm lens	Not enough light	Low resolution
Macro Zoom lens	Not enough light	Good resolution and light

a primary goal of this project is to quantify and observe the behavior of individual streamer bursts, this was not explored further. This could be used for future studies that look at the time-averaged behavior of streamer bursts.

Ultimately, a PI-MAX 4 Intensified Charged Coupled Device (ICCD) Camera was used for the imaging, with a Macro Zoom lens (Vivitar Series 1 28-90mm) and a 20 mm 3D-printed Macro extension to increase the field of view (FOV) further. The ICCD camera can take images with a gate-width (exposure time) down to nanoseconds, and has a P46 Phosphor intensifier (.2 μs decay time). For this study, the gate-width was varied from 25 to 450 μs, and the gain is varied from 14 to 48 to obtain the best possible contrast, while only imaging a single streamer burst. As will be seen later on, streamer bursts were not always captured one at a time, due to apparently random consecutive small streamer bursts.

3.2 Results

The results reported are from a series of tests on March 12 2021, where the applied voltage was varied from the streamer inception voltage, 6 kV, to close to arcing voltage, 18 kV, and the wind speed was varied from 0-30 m/s for each voltage tested.

Firstly, the images in Figure 3-8 show the 100 superimposed streamer images, from each data case. The gate-width was varied from 25 to 450 μs, and the gain is varied from 14 to 48 to obtain the best possible contrast, while only imaging a single streamer burst. As seen in Figure 3-10, at the higher wind speeds and voltages, there arises a regime where some streamer bursts are pulsating at a frequency much higher than originally expected, so the images taken in these cases may not only contain a single streamer burst. In the image batches, however, only a fraction of the images contained streamers, and those that did not contain a streamer corona did show evidence of a glow corona.

Figures 3-9, and 3-10 show the time-dependent waveform measured by the ground current for each test conducted, on the left side of the page. On the right side of the page, waveforms are plotted in the frequency domain, computed by using MATLAB's

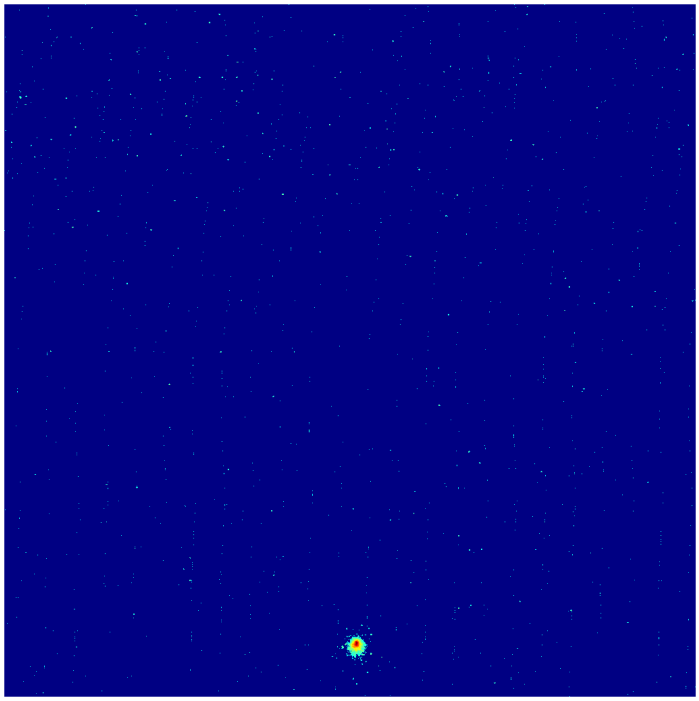

Figure 3-7: The persistent glow corona, observed in between streamer corona bursts. ICCD image of an applied voltage of 16 kV, and wind speed of 0 m/s.

fast Fourier transform (fft) tool, and filtering noise below 0.65 mA for voltages up to 16 kV, and 1 mA for the 18 kV test. The discrete Fourier Transform is a method to approximate the shape of a discrete signal using a combination of sinusoid waves. Each peak in the plot represents a certain frequency of sinusoid that was apparent in the signal. Often the plotted spectra show a decaying harmonic structure at the integer multiples of the pulse frequency, for example in the 12 kV, 0 m/s case of Figure 3-9 (h). This is expected when performing a Fourier analysis on a triangular pulse train, which is a combination of a perfect pulse train in a finite amount of time (which would result in harmonics at every integer multiple, equal in magnitude), and a triangular shape (which causes the decay).

From detecting the peaks of the ground current we can calculate the period of time in between each consecutive peak, and the corresponding frequency. For the 300-1000 streamer burst pulsations observed in each test, we can plot a distribution of the period of time in between them. This is shown on the left side of Figures 3-11 and 3-12, where the period is in log scale on the y-axis, and the horizontal width

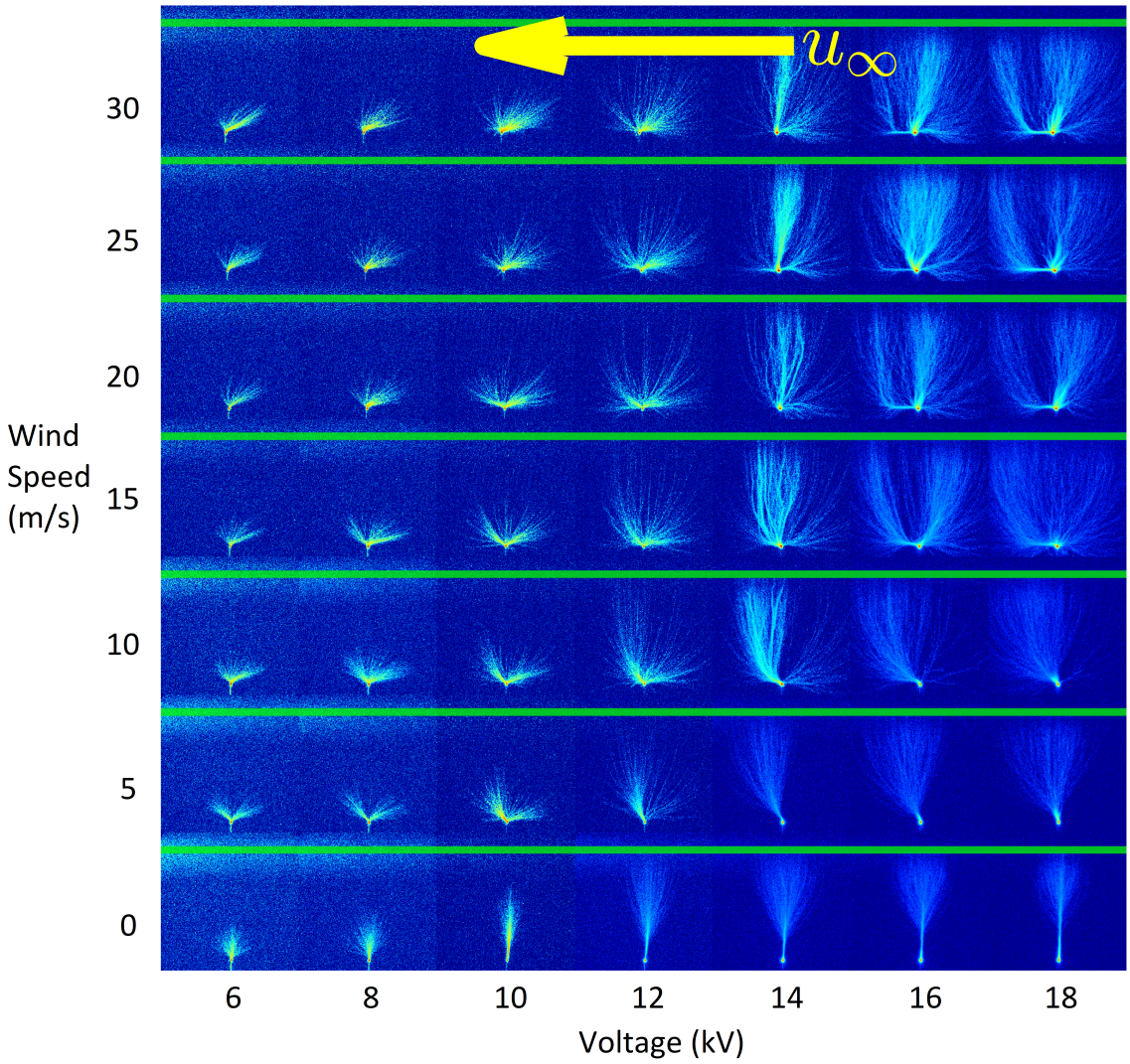

Figure 3-8: Superimposed images. Wind is going right to left. Green lines represent the ground plate.

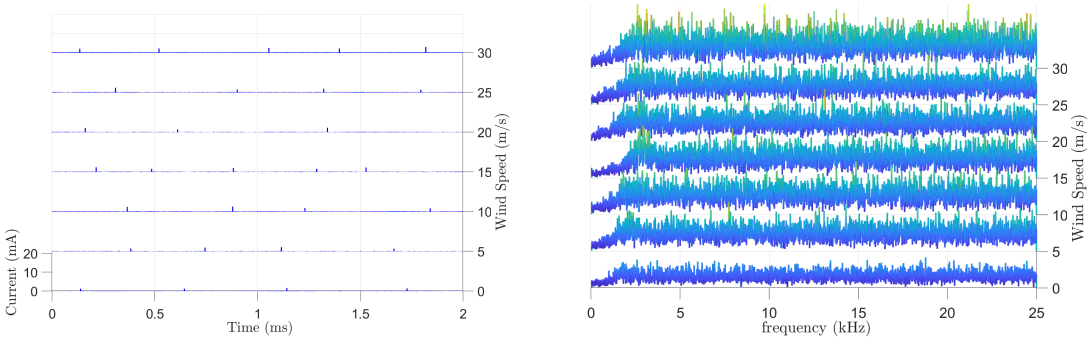

(a) 6 kV (time domain sample)

(b) 6 kV (frequency domain)

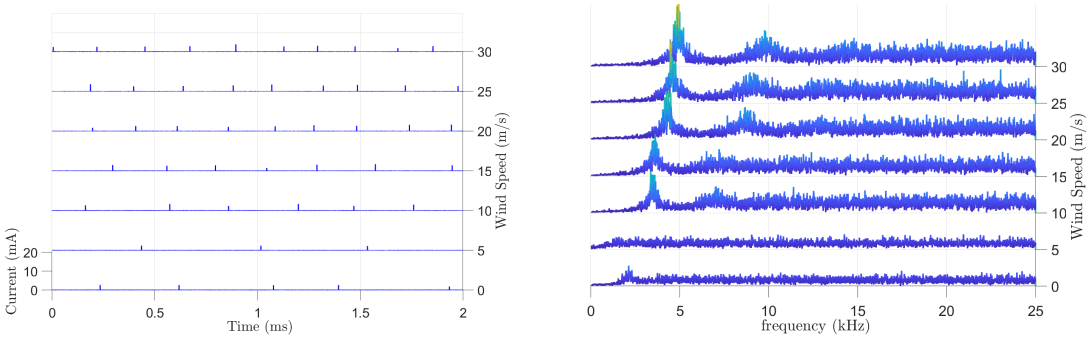

(c) 8 kV (time domain sample)

(d) 8 kV (frequency domain)

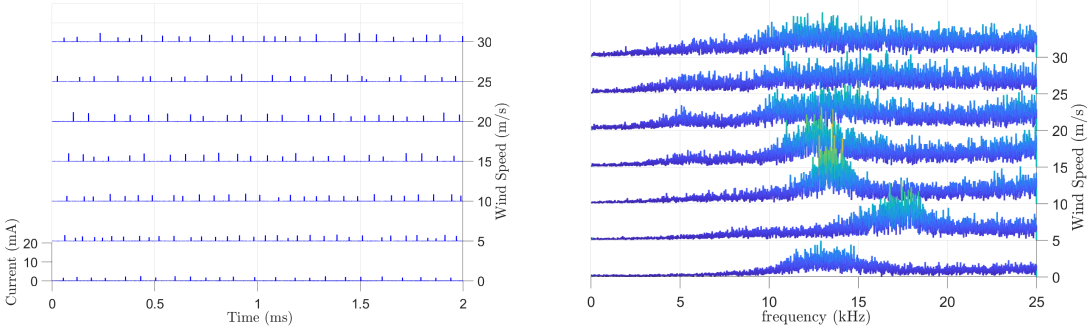

(e) 10 kV (time domain sample)

(f) 10 kV (frequency domain)

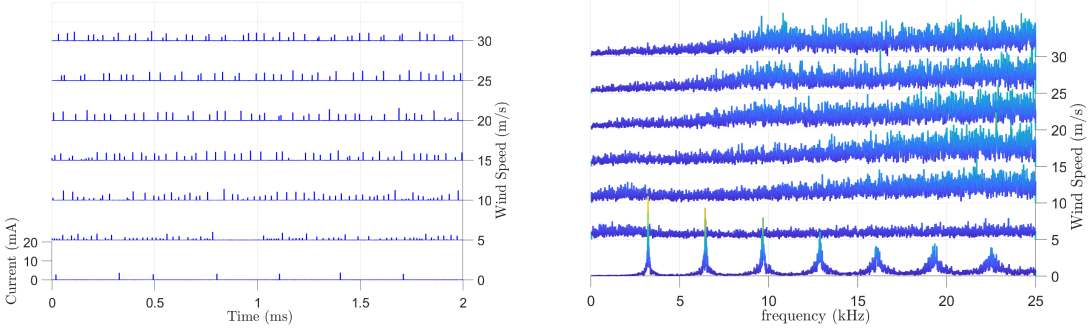

(g) 12 kV (time domain sample)

(h) 12 kV (frequency domain)

Figure 3-9: (left) A 2 ms time domain sample of the ground plate current at a range of voltages and wind speeds. (right) Current peaks plotted in the frequency spectrum at a range of voltages and wind speeds. This spectrum is based on 200 ms of data.

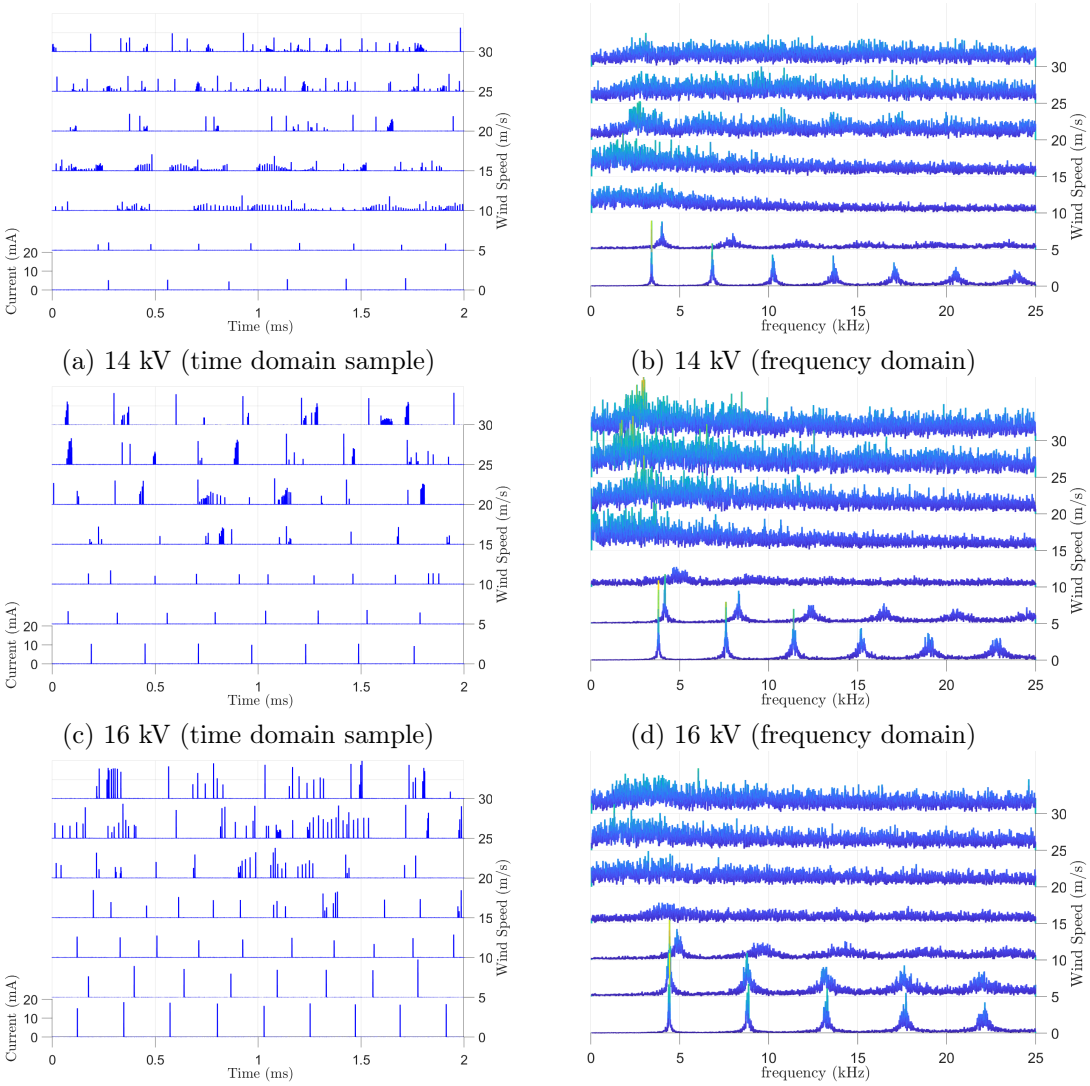

(a) 14 kV (time domain sample)

(b) 14 kV (frequency domain)

(c) 16 kV (time domain sample)

(d) 16 kV (frequency domain)

(e) 18 kV (time domain sample)

(f) 18 kV (frequency domain)

Figure 3-10: (left) A 2 ms time domain sample of the ground plate current at a range of voltages and wind speeds. (right) Current peaks plotted in the frequency spectrum at a range of voltages and wind speeds. This spectrum is based on 200 ms of data.

of each bar corresponds to the likelihood of two adjacent peaks to have that period. For reference the right-hand axis of these plots is converted to frequency. Several of these distributions are plotted next to each-other to demonstrate the change in shape at different wind speeds. The frequency corresponding to the inverse of the period is shown in the appendix Figure B-1, and can be useful to observe the trends in another way. These are shown for applied voltages of 6 kV up to 18 kV, identified by different colors, and in ascending order. The distributions in these plots are smoothed using a local, weighted linear least squares regression and a 2^{nd} degree polynomial model. This analysis well characterizes the distribution of adjacent streamer burst frequencies, but does not account for the relationships between frequency and current from non-adjacent streamers, which can be visually seen on the left side of Figures 3-9 and 3-10. An analysis that can better discriminate between different types of streamer bursts is actively being explored. A similar analysis but of the distribution of the currents measured at each peak is shown on the right side of Figures 3-11 and 3-12. These distributions are smoothed using MATLAB's kernel-smoothing density function, which is based on a normal kernel function that is estimated at 100 equally-spaced points. This can be used to show how the peak of individual current pulses changes with wind speed, as well as how it changes with voltage. It will be shown as well that, especially in the high voltage, high wind cases, there are two dominant streamer current magnitudes that are present.

3.3 Discussion

3.3.1 No Wind Case

From these plots several observations can be made. First, if only looking at the 0 m/s wind case (bottom row of each plot in Figures 3-9 and 3-10), the frequency of pulsations seems to increase as the applied voltage is increased from 6 to 10 kV. The superimposed ICCD imagery of the discharge, shown in Figure 3-8, indicates that the streamer corona discharge has not bridged the gap in these cases. At 12 kV a

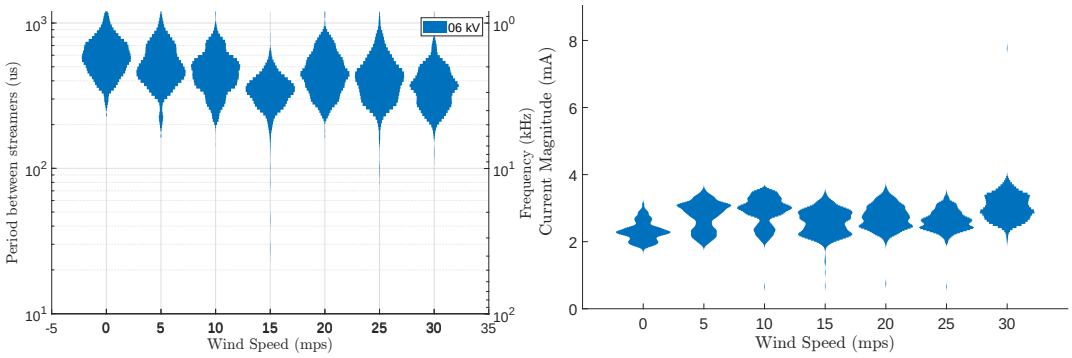

(a) 6 kV period distribution

(b) 6 kV electrical current distributions

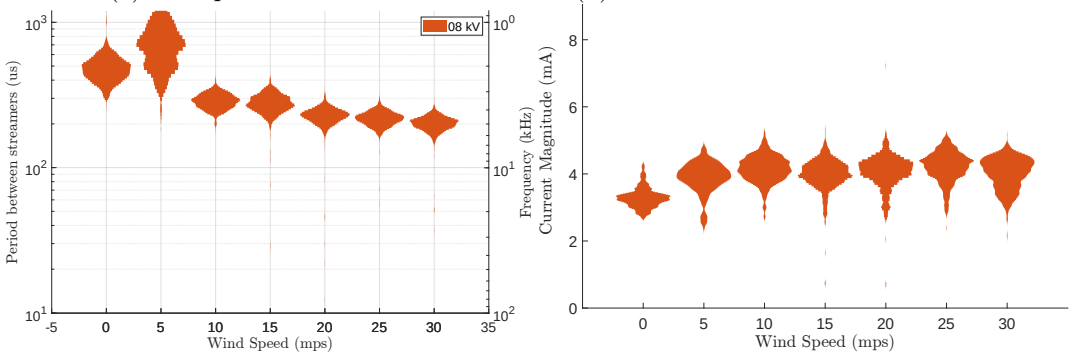

(c) 8 kV period distributions

(d) 8 kV electrical current distributions

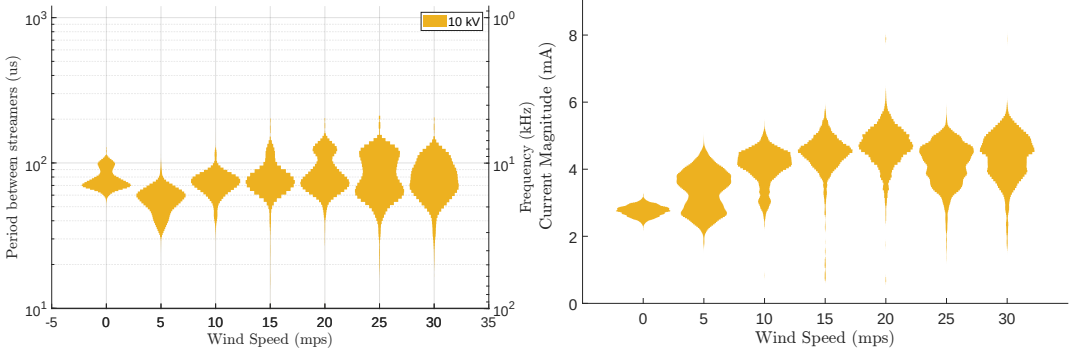

(e) 10 kV period distributions

(f) 10 kV electrical current distributions

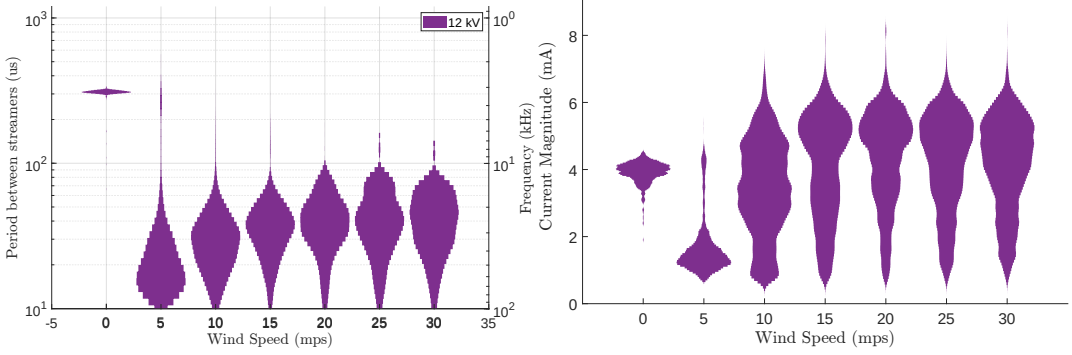

(g) 12 kV period distributions

(h) 12 kV electrical current distributions

Figure 3-11: (left) Distributions of the period of each sequential streamer burst (the inverse of the frequency) as they change with wind speed. Each distribution is normalized individually so that the maximum bin value fills the allotted horizontal space. (right) Distributions of individual pulses peak current, plotted at different wind speeds and voltages.

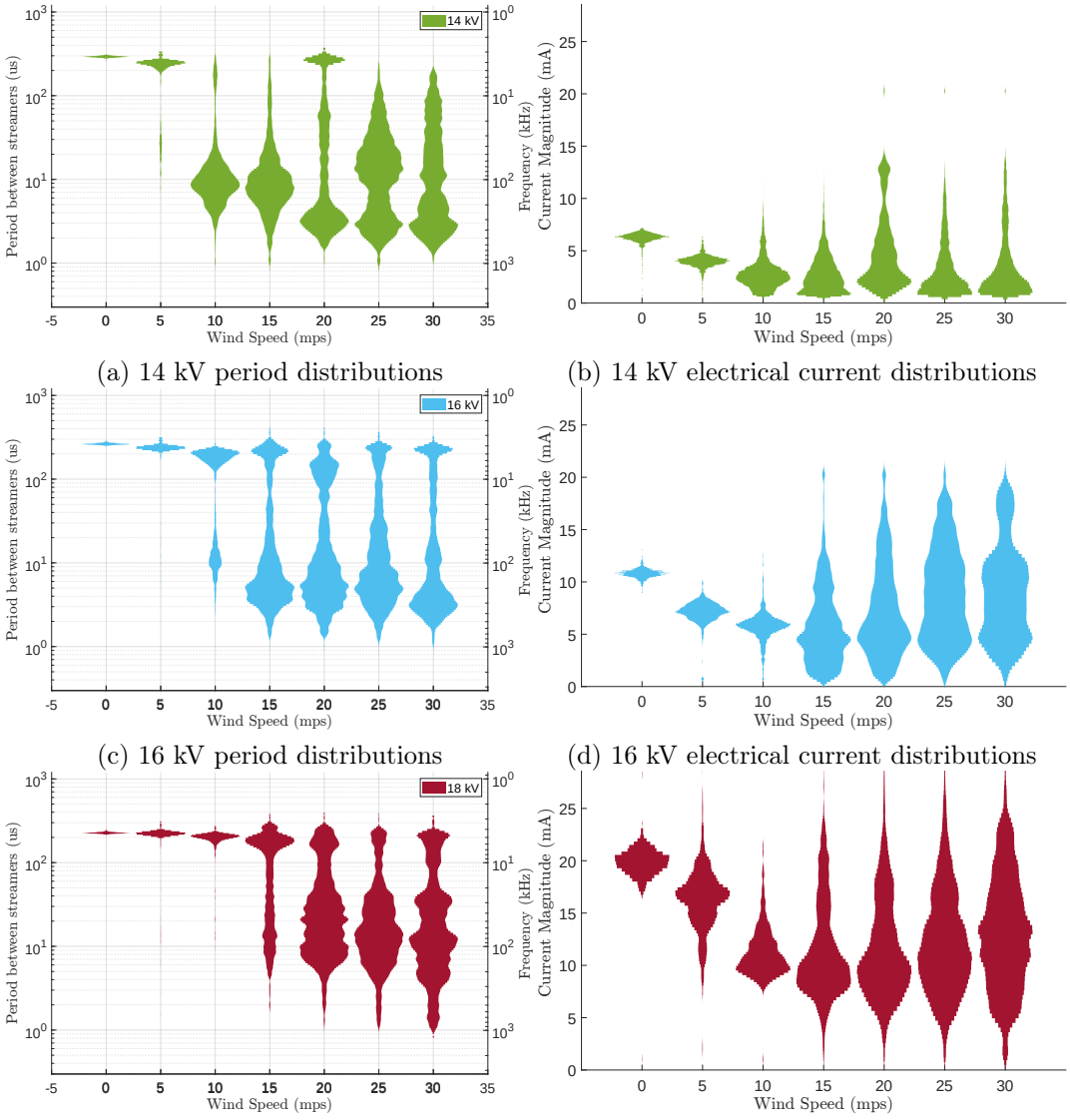

(a) 14 kV period distributions

(b) 14 kV electrical current distributions

(c) 16 kV period distributions

(d) 16 kV electrical current distributions

(e) 18 kV period distributions

(f) 18 kV electrical current distributions

Figure 3-12: (left) Distributions of the period of each sequential streamer burst (the inverse of the frequency) as they change with wind speed. Each distribution is normalized individually so that the maximum bin value fills the allotted horizontal space. (right) Distributions of individual pulses peak current, plotted at different wind speeds and voltages.

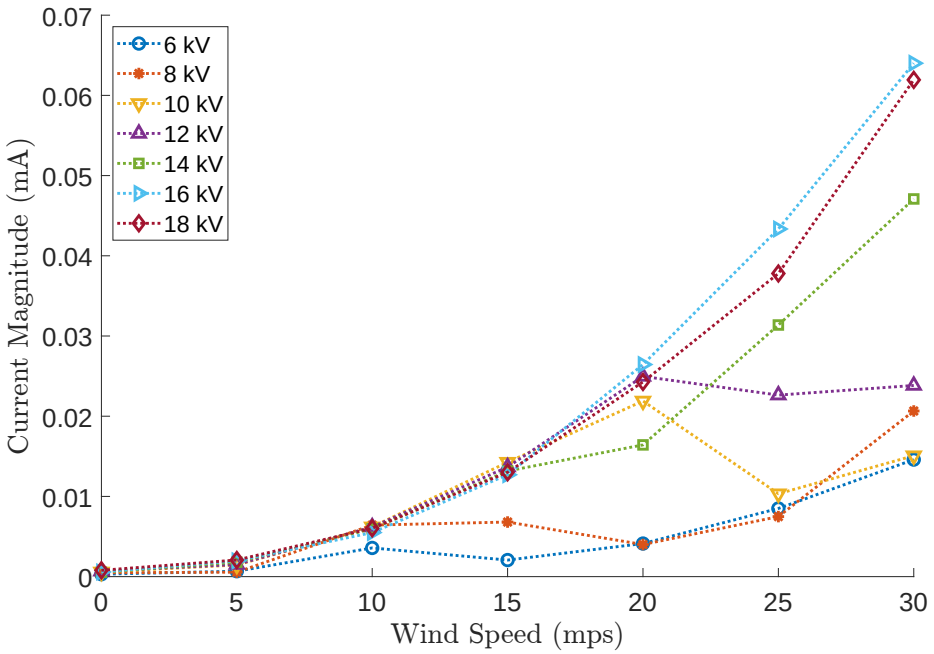

Figure 3-13: Averaged current as a function of wind speed.

new regime seems to have formed as the discharge bridges the gap and some streamer bursts make contact with the ground plate, with a lower frequency than 10 kV. This regime continues with increasing frequency as the applied voltage is increased to 18 kV. Another observation from this is that the low voltage (6-10 kV) has a broader frequency spectrum than the higher voltage (12-18 KV) regime.

From Section 1.2.1, we saw that onset streamers propagate approximately following the electric field lines until either the positive space charge overwhelms the anode, weakening its concentrated electric field, or the streamer reaches the cathode (in this case the ground plate), and the positive space charge extends the entire gap. The difference in these two scenarios is that when the streamer has not bridged the gap, there is still a portion of the gap that is under the influence of only the applied electric field, whereas when the positive space charge takes up the entire gap, the influence of the external electric field is minimal. From Figure 3-8, we can see that once the streamer has bridged the gap at voltages greater than 12 kV, as the voltage is increased further, the streamers seem to have less branching effects, due to the higher electric field. The higher electric field will also clear out the positive space charge faster, leading to a higher frequency discharge.

We can calculate a rough estimate of the expected frequency using Equation 1.1, based on the air ion drift. With applied voltages ranging from 6 to 18 kV with a gap of 25 mm, the electric field ranges from 240-720 kV/m. Assuming an ion mobility of 1.4 cm^2/Vs, the drift velocity would range from 3,360-10,080 cm/s. If we then assume that the ions must clear away the entire 25 mm for a new streamer to initiate, then we would expect a frequency ranging from 1.34-4.03 kHz. This is around the order of magnitude that we see in the results with 0 wind speed, where frequencies ranging from 1.5-15 kHz are seen.

3.3.2 Adding wind

When adding wind, the ion velocity, which drives the charge removal rate, is given by the superposition of drift and wind:

$$v_{ion} = \mu E + u_W. \tag{3.1}$$

Early work by Chapman [15] showed that for a corona discharge in wind the current is proportional to:

$$i \propto v_{ion}(V - V_c), \tag{3.2}$$

where V is the applied voltage and V_c is the corona inception threshold. Using this scaling, the dependency of current with wind speed would be expected to be at most linear for the DC glow corona. In this study of streamer corona, particularly for the higher voltages (see Figure 3-13), the dependency seems to follow more of a quadratic trend.

The distributions of the streamer burst peak current as a function of wind speed (right-hand side of Figures 3-11 and 3-12) do not show a linear or quadratic trend, however, because although the average current may be higher, the peak current may be lower with a higher frequency.

In all cases, the wind has the effect of spreading out the frequency spectrum, and making the discharges less repeatable and more erratic. This may be due to pressure

variations from turbulence caused by the tip, although this effect was found negligible in [46]. This effect also correlates with the structure of the streamer burst spreading out - instead of going straight towards the cathode, the streamers are more likely to branch out in either direction, as shown in the higher wind speeds of Figure 3-8. This spreading out will likely cause variations in the time needed for a new streamer to emerge - depending on where the space charge is after a streamer burst, the next streamer burst may have to wait different amounts of time for the space charge to clear out. The more erratic behavior can be explained by the more 'options' that the streamers have.

The next observation that can be made is that the wind tends to allow a higher frequency of streamers. Although not always obvious from the Fourier transform analysis, looking at the distribution plots in Figures 3-11 and 3-12 and as can be visually seen in the time domain plots on the left side of Figures 3-9 and 3-10, there tend to be shorter gaps in between successive streamers at higher wind speeds. In many cases, the wind reduces the amount of time for the positive space charge to clear away. This is most clearly seen at 8 kV, where the frequency band stays narrow and increases incrementally with wind speed.

The effect of wind on the streamer shape is very interesting and can be seen clearly in Figure 3-8. At 0 wind, all the streamer regimes are relatively symmetrical about the tip axis. As soon as even a small 5 m/s wind is added, the discharge changes. At the higher applied voltages, streamers operate in the regime observed by [46] and [62], where the streamer is tilting with the direction of the wind. This regime seems to be associated with a *decrease* in peak current with wind speeds, as shown on the right hand side of Figure 3-12. This may be a result of geometrical effects that cause a longer current pulse duration and lower peak current, but a higher overall amount of charge transfer. At the lower voltages, however, the streamer splits into two segments, one pointing with the wind, and one pointing against the wind. The 6 kV streamers seem to be split evenly between these two directions (see Figure A-1 in the appendix for a look at individual frames), and as the voltage is increased, the component directing with the wind becomes more prevalent. Of interesting note here

is that the 12 kV case, which seemed to be bridging the electrode gap at 0 m/s, is no longer bridging the gap after adding 5 m/s wind, and begins to show behavior more aligned with the lower voltages.

Moving up to 10 m/s, we can observe that the tendency for streamers to point against the wind becomes stronger: in all cases at least one streamer burst or branch like this is observed. Moving from 15 m/s up to 30 m/s this trend continues, until at 30 m/s almost all of the streamers bursts coming from the tip at voltages up to 14 kV, are pointing against the wind.

To summarize, the higher the voltage the more likely the streamer will be tilted with the wind, and the higher the wind speed the more likely the streamer will travel against the wind. The propagation of the streamers downwind is as observed in Ref. [46]: at the time scale of streamer propagation, wind has no effect, but at the longer timescales both ions and excited species are convected by the wind. The propagation of streamers upwind can be explained by charge accumulated in the downstream direction, so that the upwind direction effectively sees higher electric fields.

The trends seen in the structure of the discharge correlate with the distributions of the electrical current in the right side of Figures 3-11 and 3-12. In the higher voltages and lower wind speeds, as the discharge transitions from traveling with the direction of the wind to both with and against the wind, the current pulses spread out in magnitude, there are more streamer bursts of both high and low current. Notice how in the 18 kV case, when wind is applied, the streamer pulses lower in current magnitude (3-12), but increases in average current (3-13) and frequency (3-9). From these trends, it can be concluded that the streamer bursts moving with the wind tend to have a higher current (which lowers with wind speed) and lower frequency (which increases with wind speed), and the streamer bursts moving against the wind tend to have a lower current (which increases with wind speed) and a higher frequency (which also increases with wind speed).

3.4 Conclusions

The results here have successfully demonstrated a strong influence of wind on streamer corona. Wind can both direct the streamers with or against it, which depends on two competing effects related to the applied voltage on the tip. Wind tends to increase the average current, and reduces the period of time in between streamer pulses.

Future work may include widening the parameter space studied, including testing different gap distances, and different radius of curvature tips. In addition, the test setup can be modified to study p-static dischargers in wind in a similar way to the way the specification testing process.

Chapter 4

Conclusions

4.1 Summary of Conclusions

This work investigated methods of charge control for airplanes, and the related physical phenomena. As discussed in Chapter 1, aircraft charging can occur naturally by triboelectric effects, such as collisions with water molecules in the air. If unmitigated, the charge can build to levels that induce corona discharge from the radio antennas of the airplane, causing communication interference. These discharges are instead diverted to p-static dischargers, a passive form of charge control that are initiated when the airplane surpasses a voltage threshold with respect to its surrounding environment.

Recent work has demonstrated that the net charge of an airplane can have an affect on lightning initiation, and that the risk of lightning can be mitigated by controlling the charge to an optimal level that depends on the direction of the electric field. A charge control system that utilizes corona discharge to expel ions from the aircraft has been proposed and tested in the wind tunnel previously, and Chapter 2 of this thesis demonstrates this system in flight. A 1.9 m wingspan remote controlled airplane is charged to both positive and negative polarities. By applying a voltage between -13 and +13 kV to the wire, the plane is charged to +23 and -30 kV, respectively. The system demonstrates comparable results to previous modeling and wind tunnel experiments, which showed an increase in plane potential and a decrease in corona

current as wind speed increased. The technological limitations of this charge control strategy have been described, such as a saturation voltage due to spurious corona, and the delicacy of the corona wire.

The second experimental campaign in this thesis, described in Chapter 3 is focused on understanding the physical changes to positive streamer corona in response to airflow. This is motivated by the lack of wind tunnel testing of p-static dischargers that are used to passively discharge airplanes. This work has demonstrated that wind has a strong influence on the discharge characteristics: the frequency of pulsations and the average current increase with wind speed, but both become less consistent. In general, two types of streamers emerged upon adding wind: first, the streamers tended to point with the direction of the wind especially at lower wind speeds and higher voltages; at higher wind speeds and lower voltages, the streamers tend to point against the wind. To the authors knowledge, this phenomenon has not been experimentally observed before.

4.2 Recommendations for Future Work

For an active charge control system, the recommended next step is to implement the system onto a larger research aircraft that can be used to measure the electric field conditions inside thunder clouds. This will serve as both a valuable research study, but also a further validation of the results found in this work. This will also foster necessary robustness improvements that will eventually help to scale the technology up to being used on commercially manufactured airplanes.

For the study of p-static dischargers, the immediate next step will be to study the effects of wind on the commercially used dischargers, by substituting the needle. From the initial studies, not reported in this paper, the p-static dischargers tend to operate at a regime similar to a metal rod of similar radius.

Future studies of electrical discharges in wind could utilize a nanosecond pulsed power supply to investigate more forms of streamers. This could help to determine the relationship between consecutive streamers, and help modeling efforts that aim

to characterize streamers in wind.

Appendix A

Additional Single Burst Streamer Images

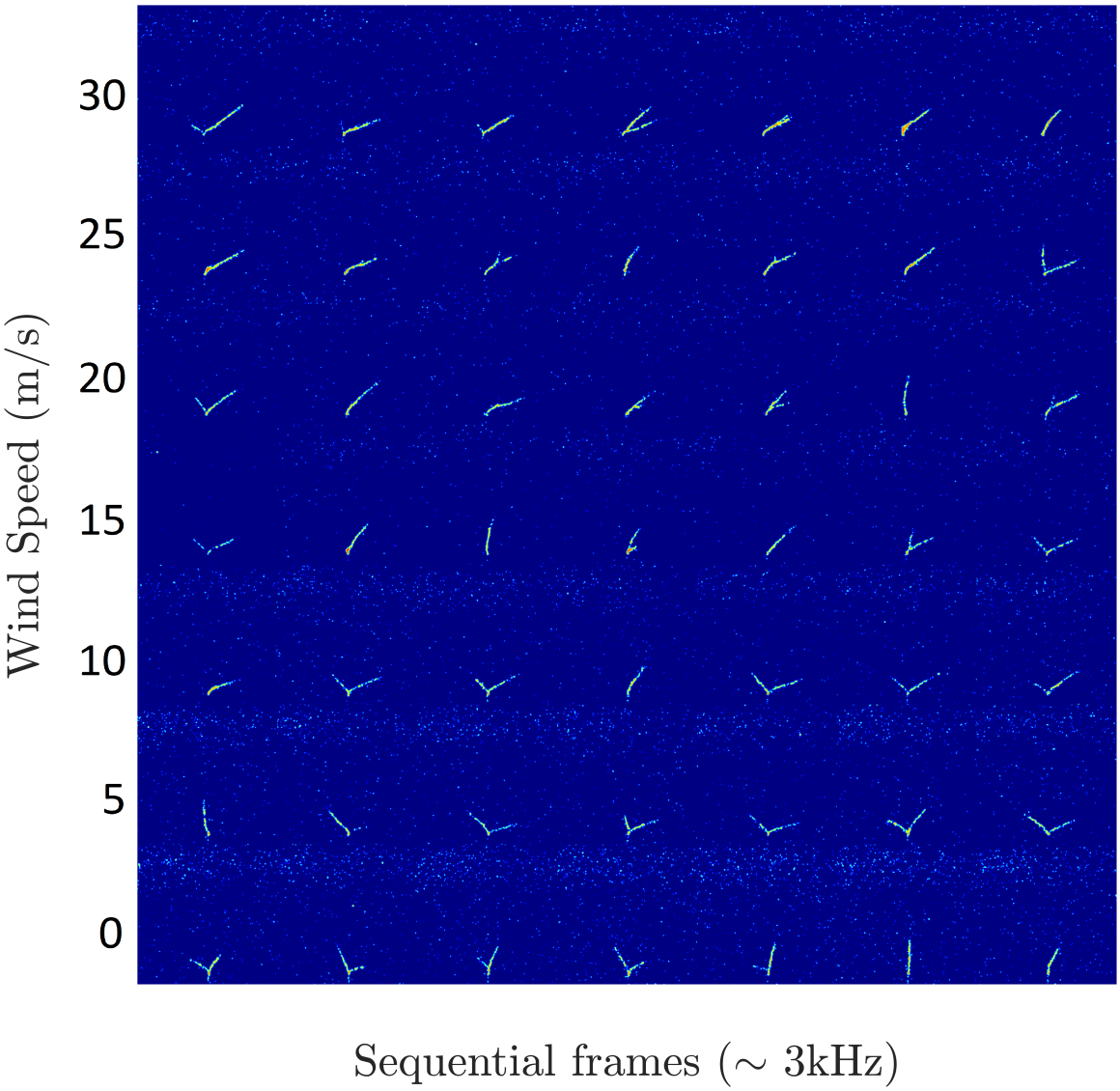

Figure A-1: 7 individual streamer bursts at 6 kV as they change with wind speed.

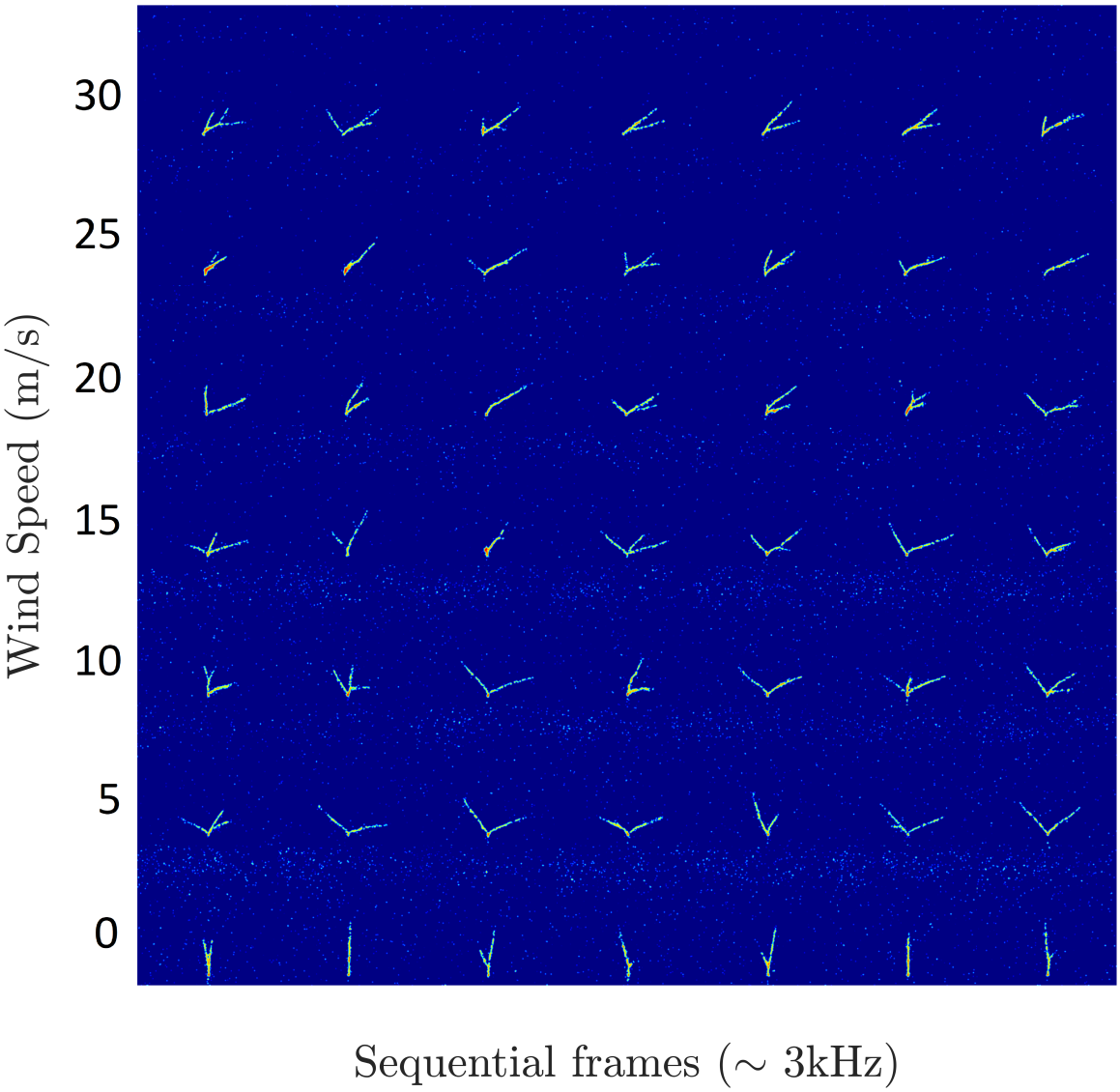

Figure A-2: 7 individual streamer bursts at 8 kV as they change with wind speed.

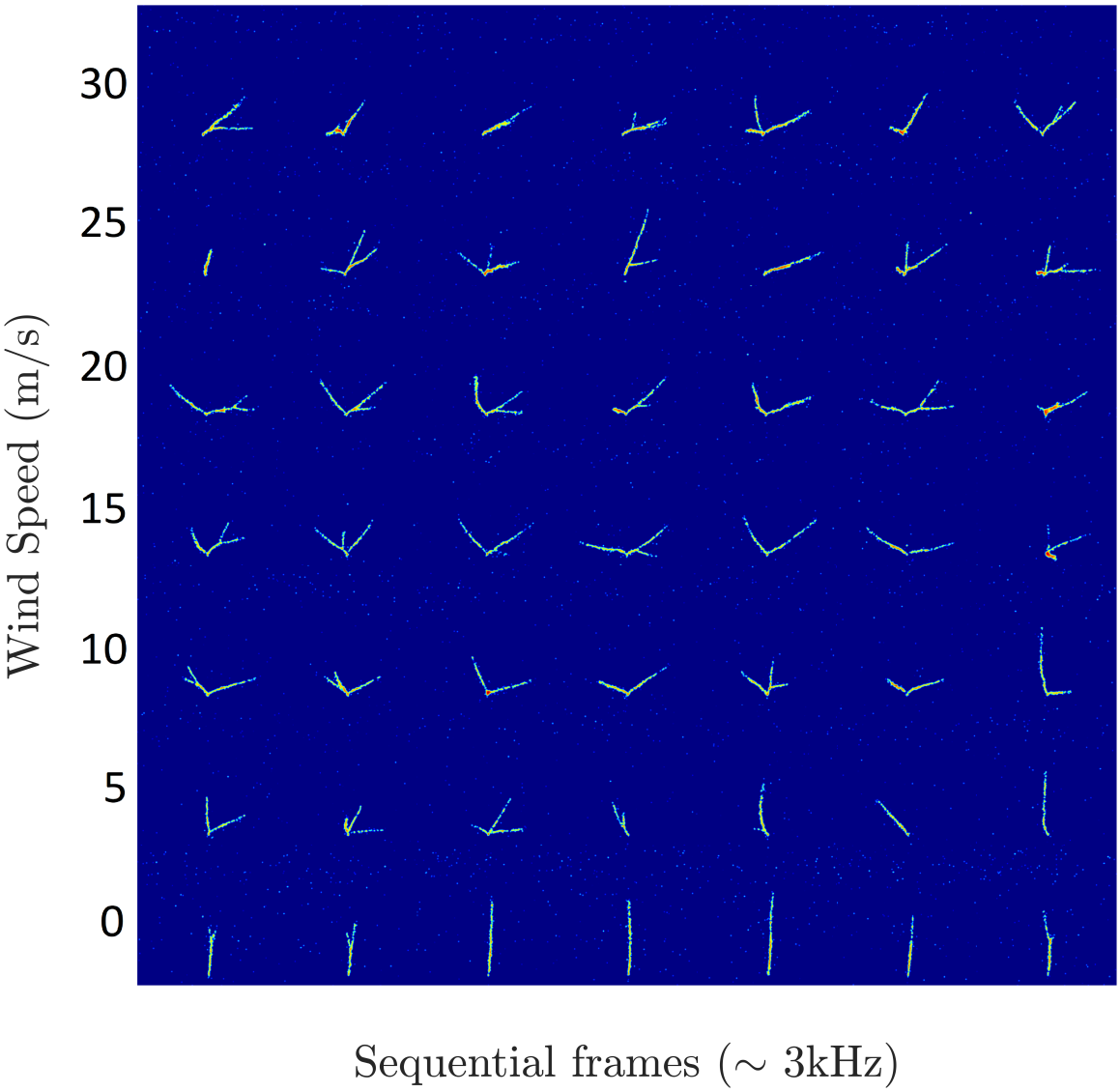

Figure A-3: 7 individual streamer bursts at 10 kV as they change with wind speed.

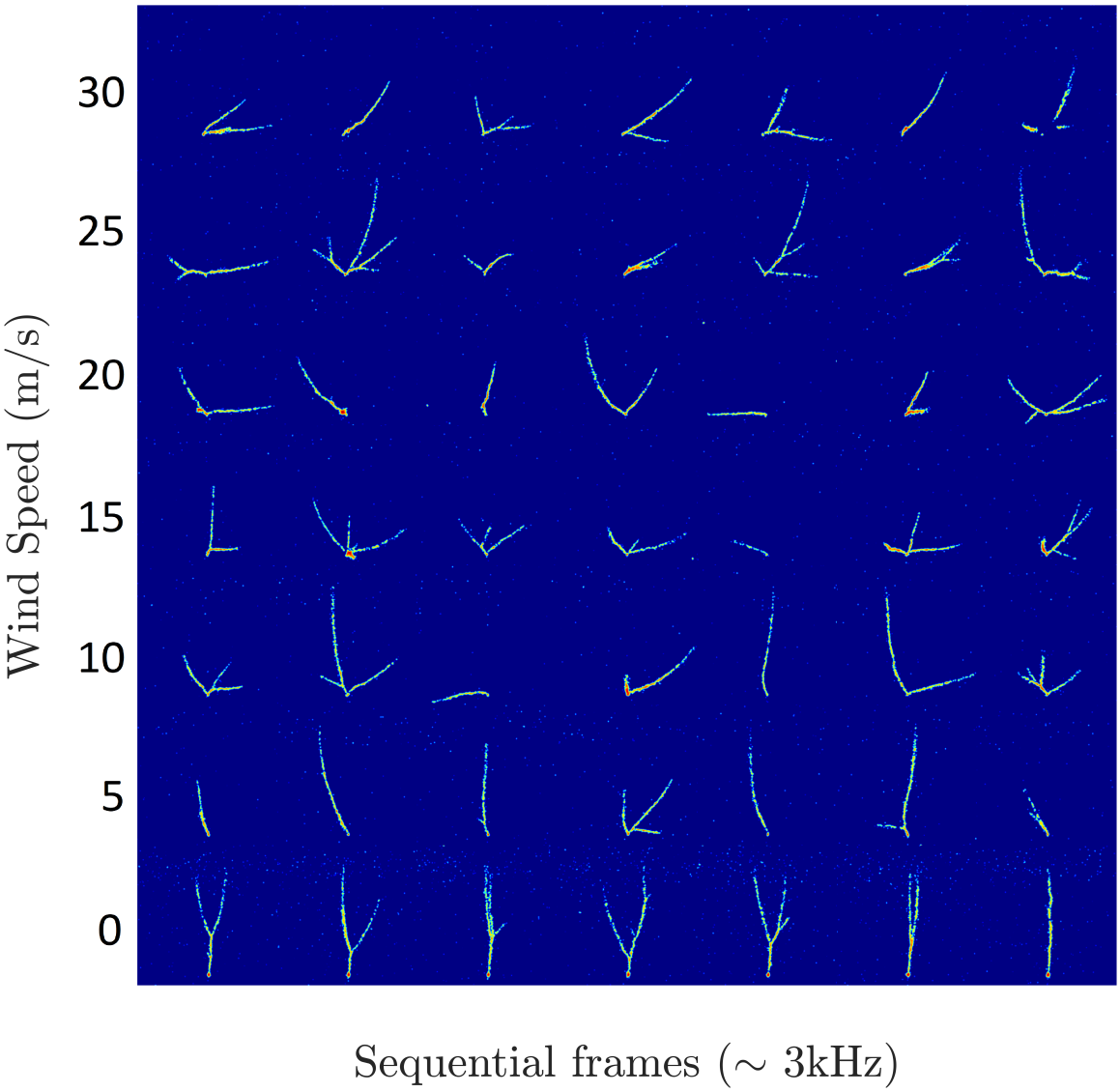

Figure A-4: 7 individual streamer bursts at 12 kV as they change with wind speed.

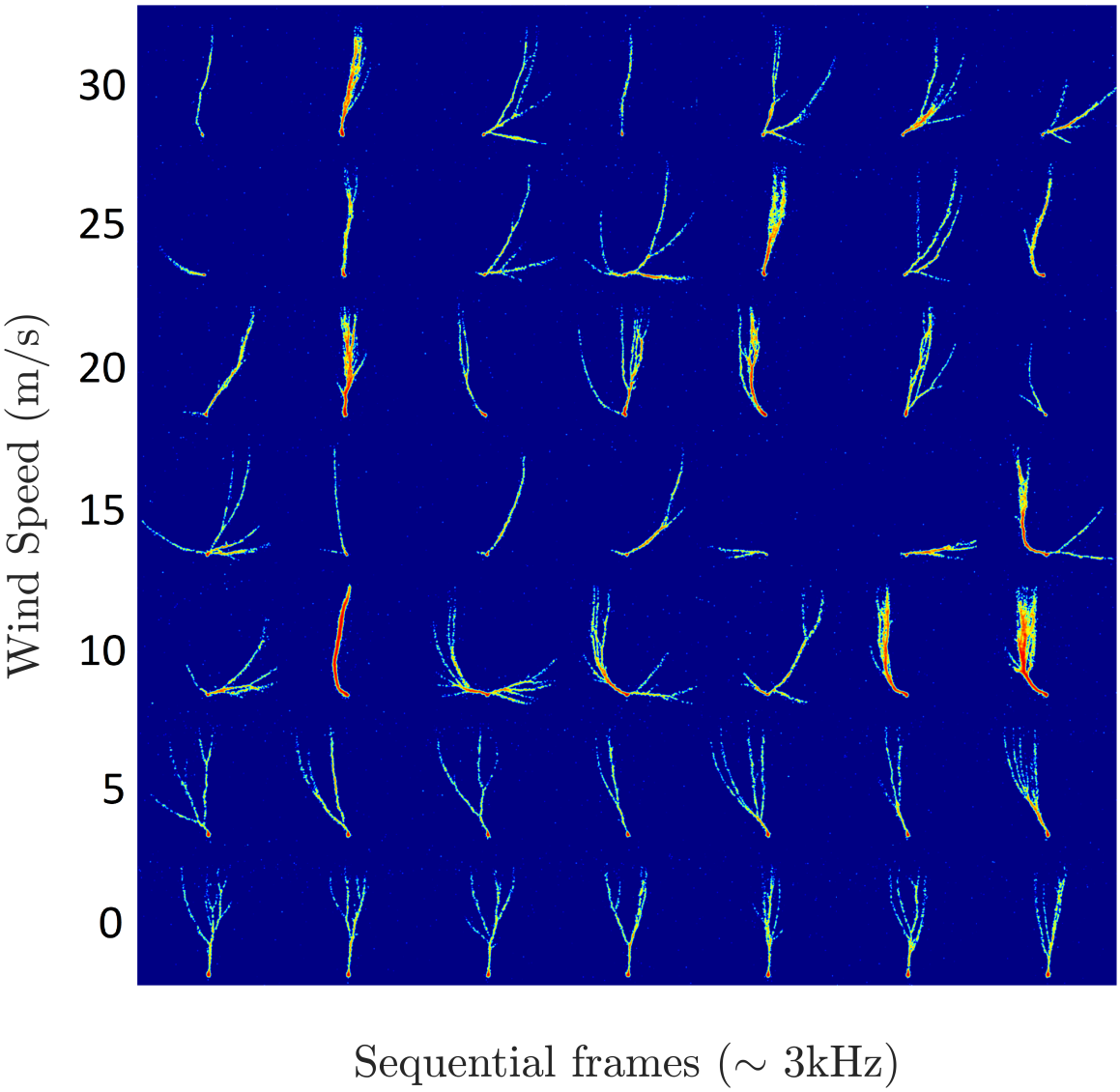

Figure A-5: 7 individual streamer bursts at 14 kV as they change with wind speed.

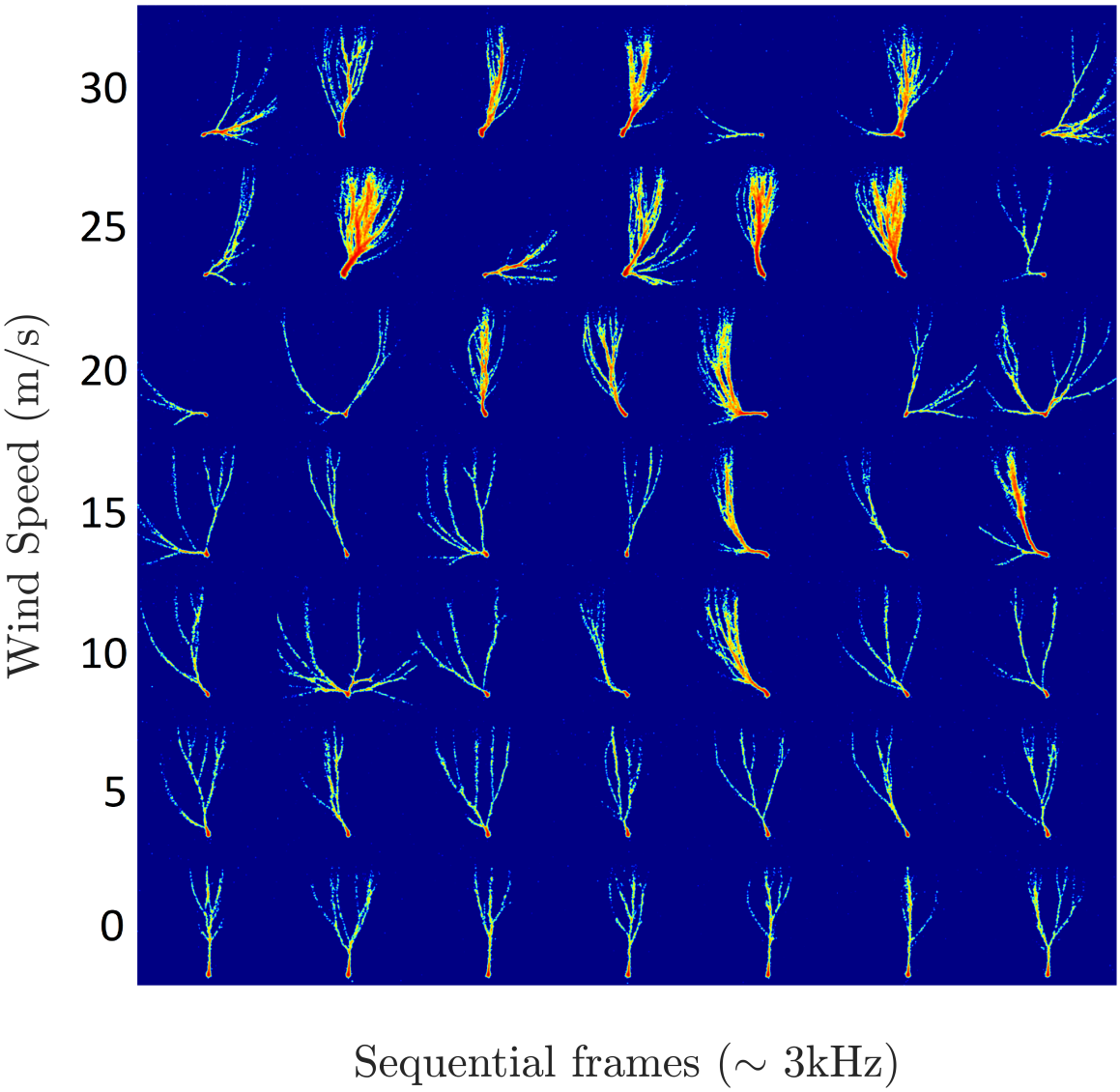

Figure A-6: 7 individual streamer bursts at 16 kV as they change with wind speed.

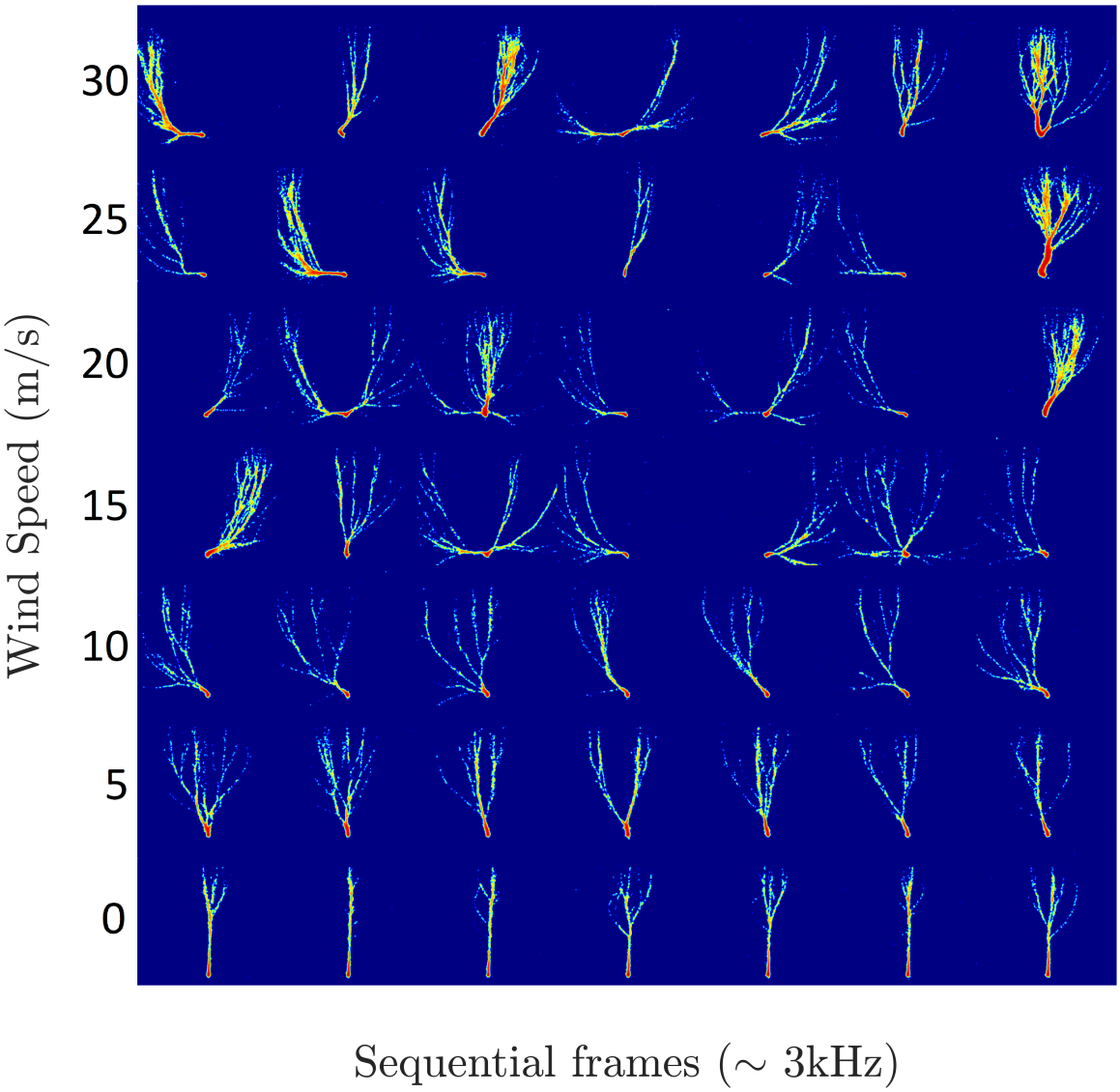

Figure A-7: 7 individual streamer bursts at 18 kV as they change with wind speed.

Appendix B

Additional Streamer Frequency Plots

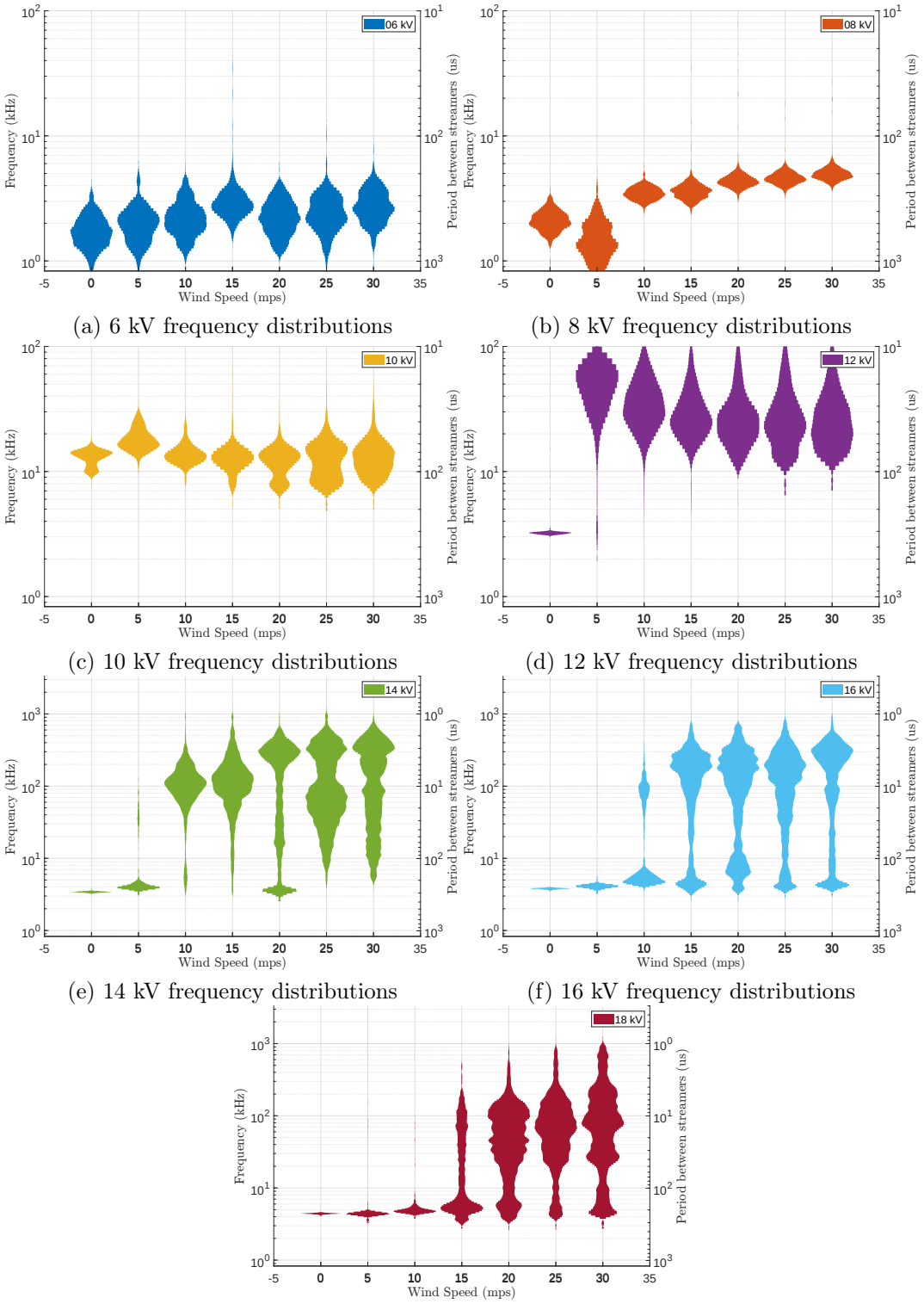

(a) 6 kV frequency distributions

(b) 8 kV frequency distributions

(c) 10 kV frequency distributions

(d) 12 kV frequency distributions

(e) 14 kV frequency distributions

(f) 16 kV frequency distributions

(g) 18 kV frequency distributions

Figure B-1: Distributions of the frequency between pulses as they change with wind speed and voltage.

Bibliography

[1] https://www.labelec.es/en/, last accessed 03/2021.

[2] Understanding Lightning: Thunderstorm Electrification, National Weather Service, NOAA, 2016. https://www.weather.gov/safety/lightning-science-electrification, last accessed: 05/2021.

[3] Electrical Bonding and protection Against Lightning and Static Electricity. Technical report, Federal Aviation Administration, 1998.

[4] MIL-DTL-9129E: Detail Specification, Electrostatic Dischargers. Technical report, Department of Defense, 2001.

[5] Aerospace Recommended Practice 5672: Aircraft Precipitation Static Certification. Technical report, SAE International, 2016.

[6] The National Severe Storms Library Research: Lightning. https://www.nssl.noaa.gov/research/lightning/, last accessed: 05/2021, 2020.

[7] F D Alessandro. Experimental study of the effect of wind on positive and negative corona from a sharp point in a thunderstorm. *Journal of Electrostatics*, 67:482–487, 2009.

[8] Marcelo Arcanjo, Joan Montanyà, Michele Urbani, Victor Lorenzo, and Nicolau Pineda. Observations of corona point discharges from grounded rods under thunderstorms. *Atmospheric Research*, 247, 1 2021.

[9] R Bartnikas and EJ McMahon, editors. *Engineering Dielectrics Volume I Corona Measurement and Interpretation*. ASTM International, 100 Barr Harbor Drive, PO Box C700, West Conshohocken, PA 19428-2959, 1 1979.

[10] Andrew J. Benkoczy and Don S. Grant. Static Discharger. US Patent 3,034,020, 6 1960.

[11] Xavier Borg. Blaze Labs EHD Thrusters Research. http://blazelabs.com/, last accessed: 05/2021, 8 2004.

[12] T M P Briels, J Kos, G J J Winands, E M Van Veldhuizen, and U Ebert. Positive and negative streamers in ambient air: Measuring diameter, velocity and dissipated energy. *Journal of Physics D: Applied Physics*, 41(23), 2008.

[13] Laurence G. Britton. *Avoiding Static Ignition Hazards in Chemical Operations: A CCPS Concept Book*. American Institute of Chemical Engineers, New York, 1999.

[14] J.-S. Chang, P.A. Lawless, and T. Yamamoto. Corona discharge processes. *IEEE Transactions on Plasma Science*, 19(6), 1991.

[15] S Chapman. Corona point current in wind. *Journal of Geophysical research*, 75(12):2165–2169, 1970.

[16] S Chapman. The magnitude of corona point discharge current. *Journal of the Atmospheric Sciences*, 34:1801–1809, 1977.

[17] S.C Coroniti. The effect of aerosols on the electrical conductivity in the atmosphere. *Geofisica Pura e Applicata*, 48:124–128, 1961.

[18] J. Cross and J. Beattie. Positive Glow Corona In Quasi-Uniorm Fields. *Canadian electrical engineering journal*, 5(3):22–32, 1980.

[19] U Ebert, C Montijn, T M P Briels, W Hundsdorfer, B Meulenbroek, A Rocco, and E M van Veldhuizen. The multiscale nature of streamers. *Plasma Sources Science and Technology*, 15(2):S118–S129, 2006.

[20] Michael Faraday. *Experimental Researches in Electricity*, volume 1. 1838.

[21] F A Fisher, J A Plumer, and R A Perala. Lightning protection of aircraft. Report, Lightning Technologies Inc., 10 Downing Parkway, Pittsfield, Massachusetts 01201, second printing, 1999.

[22] Gen. Edward Lawrence Logan International Airport Station. Weather Underground: Daily Observations, 11 2020.

[23] M. Goldman, A. Goldman, and R. S. Sigmond. The corona discharge, its properties and specific uses. *Pure and Applied Chemistry*, 57(9), 1 1985.

[24] C. Guerra-Garcia, N. C. Nguyen, T. Mouratidis, and M. Martinez-Sanchez. Corona Discharge in Wind for Electrically Isolated Electrodes. *Journal of Geophysical Research: Atmospheres*, 125(16), 2020.

[25] Carmen Guerra-Garcia, Pol Fontanes, Michele Urbani, Joan Montanya, Theodore Mouratidis, Manuel Martinez-Sanchez, and N.C. Nguyen. Controlled Electric Charging of an Aircraft in Flight using Corona Discharge. In *AIAA Scitech 2020 Forum*, pages 1–10, Orlando, FL, 2020.

[26] Carmen Guerra-Garcia, Ngoc Cuong N.C. Nguyen, Jaime Peraire, and Manuel Martinez-Sanchez. Charge control strategy for aircraft-triggered lightning strike risk reduction. *AIAA Journal*, 56(5):1988–2002, 2018.

[27] Leslie C Hale. Middle atmosphere electrical structure, dynamics and coupling. *Adv. Space Res.*, 4(4):175–186, 1984.

[28] R. G. Harrison and K. L. Aplin. Water vapour changes and atmospheric cluster ions. *Atmospheric Research*, 85(2):199–208, 8 2007.

[29] R. Giles Harrison. Long-term measurements of the global atmospheric electric circuit at Eskdalemuir, Scotland, 1911-1981. *Atmospheric Research*, 70(1):1–19, 4 2004.

[30] Michael J Johnson and David B Go. Recent advances in electrohydrodynamic pumps operated by ionic winds: a review. *Plasma Sources Science and Technology*, 26(10), 10 2017.

[31] J J Jones. Electric charge acquired by airplanes penetrating thunderstorms. *Journal of Geophysical Research. Part D, Atmospheres*, 95(10):16.589–16.600, 1990.

[32] A. K. Kamra, C. G. Deshpande, and V. Gopalakrishnan. Effect of relative humidity on the electrical conductivity of marine air. *Q. J. R. Meteorol. Soc.*, 123:1295–1305, 1997.

[33] H W Kasemir. Qualitative Uebersicht ueber Potential-Feldund Ladungsverhaltnisse bei einer Blitzentladung in der Gewitterwolke. In Das Gewitter, ed. Hans Israel, Akad. Verlags. Ges. Geest and Portig K.-G, Leipsig, Germany, 1950.

[34] G.D. Kinzer and J.W. McGee. Army-Navy Precipitation-Static Project: Part IV-Investigations of Methods for Reducing Precipitation-Static Radio Interference. *Proceedings of the IRE*, 34(5):234–240, 5 1946.

[35] P Lalande, A Bondiou-Clergerie, and P Laroche. Analysis of Available In-Flight Measurements of Lightning Strikes to Aircraft. In *International Conference on Lightning and Static Electricity*, Toulouse, France, 1999. SAE International.

[36] M.I. Large and E.T. Pierce. The dependence of point-discharge currents on wind as examined by a new experimental approach. *Journal of Atmospheric and Terrestrial Physics*, 10(5-6), 1 1957.

[37] A Larsson. The interaction between a lightning flash and an aircraft in flight. *C. R. Physique*, 3:1423–1444, 2002.

[38] Lipeng Liu and Marley Becerra. An Efficient Semi-Lagrangian Algorithm for Simulation of Corona Discharges: The Position-State Separation Method. *IEEE Transactions on Plasma Science*, 44(11):2822–2831, 2016.

[39] Min Liu, Ju Tang, Qiang Yao, and Yulong Miao. Development processes of positive and negative DC corona under needle-plate electrode in air. In *2016 IEEE International Conference on High Voltage Engineering and Application (ICHVE)*. IEEE, 9 2016.

[40] Leonard B Loeb and John M Meek. The mechanism of spark discharge in air at atmospheric pressure. I. *Journal of Applied Physics*, 11(6):438–447, 1940.

[41] Manuel Martinez-Sanchez, Carmen Guerra-Garcia, Ngoc Cuong Nguyen, Jaime Peraire, and Theodore Mouratidis. US Patent No. 10450086 B2 - Charge Control System to Reduce Risk of An Aircraft-Initiated Lightning Strike, 2019.

[42] Vladislav Mazur. A physical model of lightning initiation on aircraft in thunderstorms. *Journal of Geophysical Research*, 94(D3), 1989.

[43] C B Moore, J J Jones, S J Hunyady, W Rison, and W P Winn. Electrical hazards to airborne operations. ONR N00014-87-K-0783. Technical report, ONR, 1991.

[44] J P Moreau, J C Alliot, and V Mazur. Aircraft lightning initiation and interception from in situ electric measurements and fast video observations. *Journal of Geophysical Research*, 95(15):903–912, 1992.

[45] R Morrow. The theory of positive glow corona. *J. Phys. D: Appl. Phys*, 30:3099–3114, 1997.

[46] Mojtaba Niknezhad, Olivier Chanrion, Christoph Koehn, Joachim Holbøll, and Torsten Neubert. A three-dimensional model of streamer discharges in unsteady airflow. *Plasma Sources Science and Technology*, 4 2021.

[47] R Ny. Corrosion of stainless-steel points subjected to the positive glow corona in room air. In *7th International Conference on Gas Discharges*, 5 1982.

[48] C. Pavan, P. Fontanes, M. Urbani, N.C. C. Nguyen, M. Martinez-Sanchez, J. Peraire, J. Montanya, and C. Guerra-Garcia. Aircraft Charging and its Influence on Triggered Lightning. *Journal of Geophysical Research: Atmospheres*, 125(1):1–15, 2020.

[49] Frank W. Peek. *Dielectric phenomena in high-voltage engineering*. McGraw-Hill Book Company, New York, 3d ed. edition, 1929.

[50] J. A. Plumer. Lightning and aircraft: an incomplete history of research and standardization. In *International Conference on Lightning and Static Electricity (ICOLSE)*, Nagoya, Japan., 2017.

[51] Branko M. Radičević and Milan S. Savić. Experimental Research on the Influence of Wind Turbine Blade Rotation on the Characteristics of Atmospheric Discharges. *IEEE Transactions on Energy Conversion*, 26(4), 12 2011.

[52] H. Raether. Die Entwicklung der Elektronenlawine in den Funkenkanal. *Zeitschrift fur Physik*, 112(7-8), 7 1939.

[53] V A Rakov and M A Uman. *Lightning: Physics and Effects*. Cambridge University Press, 2006.

[54] M Saba, C Schumann, T A Warner, M A S Ferro, A R Paiva, J Heldson Jr, and R E Orville. Upward lightning flashes characteristics from high-speed videos. *Journal of Geophysical Research: Atmospheres*, 121:849–8505, 2016.

[55] Raj Kamal Singh, Sujan Fernando, Sadjad Fakouri Baygi, Nicholas Multari, Selma Mededovic Thagard, and Thomas M. Holsen. Breakdown Products from Perfluorinated Alkyl Substances (PFAS) Degradation in a Plasma-Based Water Treatment Process. *Environmental Science and Technology*, 53(5):2731–2738, 2019.

[56] D. Singleton, S. J. Pendleton, and M. A. Gundersen. The role of non-thermal transient plasma for enhanced flame ignition in C2H4-air. *Journal of Physics D: Applied Physics*, 44(2), 2011.

[57] Ronald G Stimmel, Emery H Rogers, Franklin E Waterfall, and Ross Gunn. Army-Navy Precipitation-Static Project: Part III-Electrification of Aircraft Flying in Precipitation Areas. *Proceedings of the IRE*, 34(4):167–177, 1946.

[58] Greg Sweers, Bruce Birch, and John Gokcen. Lightning Strikes: Protection, Inspection, and Repair. *AERO Magazine*, pages 19–28, 2012.

[59] N.G. Trinh. Partial discharge XIX: discharge in air part I: physical mechanisms. *IEEE Electrical Insulation Magazine*, 11(2), 1995.

[60] Irene Tzinis. NASA Technology Readiness Level. https://www.nasa.gov/directorates/heo/scan/engineering/technology/ technology_readiness_level, last accessed: 05/2021, 4 2021.

[61] Oscar A. van der Velde, Joan Montanyà, Jesús A. López, and Steven A. Cummer. Gigantic jet discharges evolve stepwise through the middle atmosphere. *Nature Communications*, 10(1):4350, 2019.

[62] Stephan Vogel and Joachim Holboll. Experimental evaluation of discharge characteristics in inhomogeneous fields under air flow. *IEEE Transactions on Dielectrics and Electrical Insulation*, 25(2):721–728, 4 2018.

[63] B Vonnegut and A D Little. Electrical behavior of an airplane in a thunderstorm. *Technical Report for Federal Aviation Agency*, pages FAA–ADS–36, 1965.

[64] B Vonnegut, B C Moore, and F J Mallahan. Adjustable potential-gradient-measuring apparatus for airplane use. *Journal of Geophysical Research*, 66:2393–2397, 1961.

[65] Ramond C Waddel, Richard C Drutowski, and William N Blatt. Army-navy precipitation-static project: Part II-aircraft instrumentation for precipitation-static research. *Proceedings of the IRE*, 34(4):161–166, 1946.

[66] Shuqun Wu, Wenxin Cheng, Guowang Huang, Fei Wu, Chang Liu, Xueyuan Liu, Chaohai Zhang, and Xinpei Lu. Positive streamer corona, single filament, transient glow, dc glow, spark, and their transitions in atmospheric air. *Physics of Plasmas*, 25(12), 2018.